Fluid-Rock Interactions
from the Lithosphere to Earth's Surface

Thesis by

Carl Raymond Swindle

In Partial Fulfillment of the Requirements for
the degree of
Doctor of Philosophy

CALIFORNIA INSTITUTE OF TECHNOLOGY
Pasadena, California

2024
Defended September 26, 2023

Carl Raymond Swindle
ORCID: 0000-0002-8706-9398

ACKNOWLEDGEMENTS

First, I would like to thank my advisor, Kenneth Farley, who has guided me in my research endeavors and provided me with quality feedback on my projects. Through the opportunities I have pursued in his lab, I have learned a great deal about mass spectrometry, noble gas geochemistry, and how to conduct cutting-edge analytical research. While working with Ken, I have learned to think rigorously about the use of analytical techniques applied to geological samples and the extrapolations that can be made to place constraints on geological processes.

I greatly appreciate the guidance, feedback, and discussions regarding computational geochemistry offered by Paul Asimow, who also led an amazing field trip to Hawaii earlier this year. Paul has provided extraordinary mentorship. Through working with him I have had the opportunity to expand deeper into computational research than I initially anticipated.

I further acknowledge Theodore Present and Paulo Vasconcelos who have both been excellent mentors, providing me with invaluable samples, advice, discussions, and feedback associated with method development and wet chemistry. I have always enjoyed the engaging discussions we had together; many of which included Surjyendu Bhattacharjee and Emily Cardarelli, who have also been superb colleagues.

I have benefited from the mentorship and discussions I have had with Jonathan Treffkorn and Nathan Dalleska, who have both provided me with high level guidance using, operating, and debugging problems associated with mass spectrometers. Having a background of conducting mostly modeling and field-based projects before Caltech, I am grateful for the time Jonathan and Nathan have invested and the communication they have provided.

I appreciate Brian Wernicke for the opportunity to analyze detrital zircons at the Geochron Lab at the University of Arizona during my first year at Caltech. Although we did not successfully date the Ediacaran ash deposits, I learned a great deal about geochronology and how one could in principle couple tectonic models with geochronological data to place reasonable constraints on the timing of deposition of every bed throughout hundreds of meters of otherwise undatable strata.

I have benefited from the feedback I received from people on academic committees, such as those on my thesis committee including John Eiler, Ed Stolper, and Francois Tissot, and those on my qualifying exam committee such as Heather Knutson and Jess Adkins.

I acknowledge everyone in the Farley Lab group including Jonathan Treffkorn, Jessica Muller, Florian Hoffman, Benjamin Thyer, Alessandra Flaherty, Peter Martin, Ruolin Deng, Frank Pavia, Jeff Osterhout, Abigail Keebler, Hayden Miller, Iva Tomchovska, and others who have visited for brief periods of time. I have learned a lot from everyone in the lab through group discussions and one-on-one conversations.

I want to thank the collaborators who provided me with samples, including Basil Tikoff, Sarah Francis, Doug Clark, and Francis Macdonald. I acknowledge Roberta Oberti and Massimo Boiocchi for providing me with critical data utilized for model calibration in Chapter 3. I am grateful for insights provided by Paula Antoshechkin regarding model formulation. I want to thank both Doug Clark and Paulo Vasconcelos once more for organizing field expeditions that were crucial to my research.

I am grateful for opportunities provided by the Division of Geological and Planetary Sciences at Caltech including support for emergency responder training and safety training for exposure to x-rays and radioactive materials.

I have benefited from the National Science Foundation Graduate Research Fellowship Grant (DGE-1745301), the Simons Foundation, the Santa Barbara Scholarship Foundation, and Caltech, which have all contributed to funding my research. I appreciate the Resnick Sustainability Institute for funding Water and Environment Lab at Caltech.

I am grateful for the work of Julie Lee, Julia Zuckerman, Jennifer Shechet, Kacey Gibson, Mark Garcia, and everyone in the Division of Geological and Planetary Sciences and Caltech at large who make this institution operational.

I have also benefited from use of other analytical facilities managed by Claire Bucholz, George Rossman, and Chi Ma.

My teaching skills have developed considerably while serving as a teaching assistant for courses taught by Joseph Kirschvink, Joann Stock, Donald Burnett, Paul Asimow, Jennifer Jackson, and Nathan Dalleska. These opportunities have provided me with experience managing large groups of students, effectively communicating complex topics, and organizing multiple-day field trips.

I have enjoyed working alongside those in the geology option in my cohort at Caltech including Juliet Ryan-Davis and Xenia Boyes, along with others in my cohort. You were all extremely supportive building up to qualifying exams. I am especially grateful for my friendships with Krittanon Sirorattanakul and Ruolin Deng, who made the social isolation during the COVID-19 pandemic more manageable.

I am happy to have spent time exploring the natural world with Paolo Sanchez, Will Palfey, Cullen Quinn, Oliver Wilner, and others who I have gone on rockhounding trips with over the past few years. I appreciate the many discussions I have had about topics I am less familiar with that I have had with my office mates, including Abdalla Bakri, who is in my office working alongside me as I write this section. By the way, it's Sunday afternoon on Labor Day weekend. I have enjoyed playing basketball with Julie Inglis, Amanda Bednarik, Ren Marquez, and others affiliated with Caltech and the Pasadena area.

Obviously, my journey did here did not start at Caltech. I am grateful to those who ignited my interests in the geosciences including Jan Shultz, Jeff Myers, Eiko Katio, Parker Shankin-Clarke, and many other faculty members and students at Santa Barbara City College. I am thankful for the excellent mentorship and motivation to pursue graduate school at Caltech after obtaining by bachelor's degree provided by Bradley Hacker, Robert Holder, John Melack, and others at the University of California, Santa Barbara.

I would not be here right now if it weren't for my family and close friends who have been exceptionally encouraging and have supported me throughout my life. I am greatly appreciative of my partner Adriana Piña Paez, who has been extremely supportive of me and my wellbeing during this time. I am grateful for everyone who ever challenged me to do better or provided me with the support I needed. I look forward to my next steps in the journey of life, wherever they may be.

ABSTRACT

Fluids can cycle and migrate through planetary bodies, transporting soluble ions and influencing physical properties of the surrounding rock or magma, such as fracture toughness, seismic wave velocity, melting point, viscosity, and more. Precipitated minerals, fluids trapped in inclusions, and free pore fluids can be used to constrain fluid provenance, mixing relationships, and paleoenvironmental information such as temperature, pressure, redox conditions, salinity, and pH. In my thesis, I discuss my research on topics pertaining to the geochemistry associated with fluid-rock interactions that occur from the depths of the lithospheric mantle to Earth's surface. Broadly, these chapters address open questions pertaining to 1) the retention timescales and metasomatic overprinting of fluids sourced from the mantle in obducted peridotites, 2) the capacity for pedogenic Mg-carbonates to preserve palaeohydrological information with implications for Martian carbonates, and 3) the influences hydrous fluids have on lithospheric magmas and minerals.

Helium isotopes are arguably the best tracer for fluid sources in Earth materials at the planetary scale. $^{3}He/^{4}He$ ratios of the Earth's 1) continental crust, 2) atmosphere, 3) upper mantle, and 4) core or deep isolated mantle (mantle plume source) vary by over two orders of magnitude, offering considerable dynamic range compared to measurement precision. While helium isotope signatures in Earth's mantle have been determined almost exclusively by the analysis of helium retained in mantle xenoliths, phenocrysts, erupted glasses, and vent gases, this selection introduces a sampling bias towards fluids that have been transported to Earth's surface by eruptive processes. In contrast, residual mantle peridotites take much longer to arrive at Earth's surface and are therefore more susceptible to metasomatic processes that can overprint primary helium isotopic signatures. In Chapter 1, I use concentrations and isotopes of helium and argon along with concentrations of U and Th to place constraints on the sources and siting of helium retained in exhumed mantle peridotites collected from Twin Sisters Mountain of the Northern Cascades in Washington State, USA. Helium isotope ratios of peridotites from the Twin Sisters Mountain span from 0.8 to 6 times the atmospheric ratio ($1R_A=1.4*10^{-6}$ $^3He/^4He$). Fluid inclusions in these peridotites capture a two-component mixture that included a mantle-like endmember (~6 R_A) and a serpentinizing endmember (1.0±0.5 R_A) that is consistent with a mixture of surface-derived groundwater, leached crustal radiogenic helium and reworked mantle helium. While these components are not effectively isolated by extraction using vacuum crushing and powder fusion, step-heating analysis reveals that the serpentinizing endmember is released at lower temperatures (<1000°C) and the mantle-like endmember is released at higher temperatures. Results demonstrate that helium signatures can be retained in lithospheric peridotites against both diffusive loss and radiogenic ingrowth over at least 10^8-year timescales but can be greatly modified by cryptic metasomatic processes during emplacement.

Mg-carbonates have become increasingly relevant in the scientific community due to their orbital and in situ detection on the Martian surface. Like Ca-carbonate on Earth, Martian Mg-carbonates may preserve paleoenvironmental information associated with their formation on Mars billions of years ago, shedding light on habitability. Yet, unlike Ca-carbonates, the capacity for Mg-carbonates to preserve paleoenvironmental information through trace element signatures associated with their source fluids has not been well established for surficial magnesite samples on Earth. In Chapter 2, I 1) develop a digestion protocol to selectively digest Mg-carbonates (magnesite ± dolomite) while obviating

influences of contaminant phases and ions adsorbed to mineral surfaces, 2) validate a method to analyze trace elements with Mg-matrix by solution ICP-MS, and 3) apply these procedures to determine trace element concentrations of pedogenic Mg-carbonates sampled along a depth profile in the Kunwarara open pit magnesite mine in Queensland, Australia. Results from this study confirm that the method we implemented selectively digests magnesite ± dolomite. A relationship between negative Ce anomaly in the carbonates and Fe/Mn-oxides/hydroxides in corresponding host sediment collected along the depth profile demonstrates that pedogenic magnesites can capture redox gradients in the soil column. This finding implies that Ce anomaly in carbonates can potentially be used to place constraints on the paleo-redox conditions associated with Mg-carbonate formation on ancient Mars.

Numerous questions in Earth science depend on quantitative understanding of how elements fractionate during melting and crystallization. To name a few: assessment of how lithospheric fluids influence geodynamical processes, constraining mechanisms that led to the formation of the Earth’s continental crust, evaluation of elemental fluxes from the mantle to Earth's surface, calibration of a reliable crustal barometer, and gauging how magmatism and plate tectonics differed with the higher geothermal gradients of a younger Earth. MELTS thermodynamic software is a widely available free tool utilized by geoscientists to both test hypotheses and model the geochemistry of magmatic processes. However, minerals of the amphibole supergroup, although common in magmatic systems, rarely crystallize in MELTS simulations, even when well controlled experiments demonstrate that they should. The decrease in the Gibbs energy needed to stabilize amphibole in MELTS is often on the order of the configurational entropy contribution to the Gibbs energy associated with minor elements that are not present in any of the current amphibole solution models used in MELTS but are frequently incorporated in the amphibole crystal lattice. In Chapter 3, I outline a framework for a volume model for monoclinic amphiboles that can be used in an expanded amphibole solution model to be incorporated in MELTS software. A volume model is prerequisite to calibrating the other model terms because it accounts for differences in pressure among experimental constraints. The framework I develop extends the model to include minor components that are not present in existing versions of the MELTS amphibole models. I calibrate a preliminary model using a dataset composed of x-ray refinements that supply amphibole volume and site occupancy data. Results reveal regions in parameter space where data is limited and the sensitivity that model coefficients have to uncertainties in the data, suggesting that filtering the dataset to remove outliers may be necessary.

PUBLISHED CONTENT AND CONTRIBUTIONS

Swindle C, Clark D, Farley KA (2023). Helium isotope evidence for mixing of mantle-derived fluids and deeply penetrating surface waters in an obducted perdotite massif. *Geochimica et Cosmochimica Acta* **353**: 45-60. DOI: 10.1016/j.gca.2023.05.015.

CS participated in the design of the project, conducted the field work, collected samples, performed the analytical work, synthesized the results, and wrote the paper.

TABLE OF CONTENTS

LIST OF ILLUSTRATIONS

LIST OF TABLES

Chapter 1

HELIUM ISOTOPE EVIDENCE FOR MIXING OF MANTLE-DERIVED FLUIDS AND DEEPLY PENETRATING SURFACE WATERS IN AN OBDUCTED PERDOTITE MASSIF

The contents of this chapter have been published with the following citation:

Swindle C, Clark D, Farley KA (2023). Helium isotope evidence for mixing of mantle-derived fluids and deeply penetrating surface waters in an obducted perdotite massif. *Geochimica et Cosmochimica Acta* **353**: 45-60. DOI: 10.1016/j.gca.2023.05.015.

1.1 Abstract

We measured He and Ar in fresh peridotites from the Twin Sisters massif, Washington USA. ^{3}He/^{4}He ratios measured on more than 35 samples are highly variable (~0.8 to ~6 times the atmospheric ratio, R_A). Step-heating of a subset of these samples in every case reveals a low ^{3}He/^{4}He component (~1 R_A) released at <1000°C and a high ^{3}He/^{4}He component (>3 R_A) above that temperature, but these components are not effectively isolated by crushing and powder fusion analysis. He-Ar systematics indicate an intimate association of two fluid-inclusion hosted components in the peridotites. The first is a ~6 R_A mantle component that is released at higher temperatures during step heating and is more abundant in dunite bands than surrounding harzburgites. The second component, released at low temperatures, has a ^{3}He/^{4}He ratio of 1.0±0.5 R_A, atmospheric ^{40}Ar/^{36}Ar, and ^{4}He/^{40}Ar far above atmospheric. It appears to be a mixture of mantle and radiogenic He sources introduced during obduction-related serpentinization, sometimes invisible, by surface-derived waters enriched with deeply-sourced helium.

These data indicate that mantle noble gas signatures can be retained in lithospheric peridotites against both diffusive loss and radiogenic ingrowth over at least 10^8 year timescales, likely due to concentration and immobilization of He in fluid inclusions. However, the mantle signature can be greatly modified by pervasive and potentially cryptic fluid alteration during emplacement.

1.2 Introduction

A wealth of He isotope data obtained from submarine volcanic glasses and mafic minerals and xenoliths in lavas has contributed substantially to an understanding of the geochemical evolution of Earth's mantle (e.g., Dunai and Porcelli, 2002; Farley and Neroda, 1998; Graham, 2002; Hilton *et al.*, 2002). Helium trapped in these erupted materials has integrated a series of processes enroute to the Earth's surface, including melt-solid interaction, magma mixing, degassing, and decompression and associated fluid inclusion decrepitation and likely exchange of He between inclusions in crystals and surrounding magma. In contrast, obducted peridotite massifs, such as ophiolites, provide direct access to depleted residual mantle. Such bodies can preserve phase assemblages and magmatic and deformation features that form in the mantle at length scales larger than evident from xenoliths; in some cases, detailed three-dimensional views of these structures are exposed over square kilometer areas (e.g., Braun and Kelemen, 2002; Kelemen *et al.*, 1995; Kruckenberg *et al.*, 2013; Pirard *et al.*, 2013; Tikoff *et al.*, 2010; Toy *et al.*, 2010). In addition, some ophiolites are up to hundreds of millions of years old (Dann, 1991; Furnes *et al.*, 2007; Kusky *et al.*, 2001), and may record upper mantle He isotope characteristics in the distant past. Thus, massif peridotites may carry unique information on the composition, spatial and temporal distribution, and behavior of He in the mantle that is complementary to the erupted record.

Relatively little is known about the siting and distribution of He in the mantle and more could be learned from studying obducted mantle rocks. Helium is strongly partitioned from minerals into melts, with the bulk mineral-melt distribution coefficient likely ~10^{-3}-10^{-4} (Heber *et al.*, 2007; Jackson *et al.*, 2013; Marty and Lussiez, 1993; Parman *et al.*, 2005). Distribution coefficients combined with the estimated He concentration of the upper mantle (~$1\text{x}10^{-5}$ cc/g: Porcelli and Ballentine, 2002) suggest the He concentration in the mantle following melt extraction should be on the order of ~10^{-8}-10^{-9} cc/g or less. However, these partition coefficients may not be completely relevant to actual mantle conditions. For example, at mantle temperatures He may migrate over geologic timescales from energetically unfavorable sites in olivine or pyroxene matrix into grain boundaries, fractures, deformation features, and especially melt or fluid inclusions (Baxter *et al.*, 2007; Blard *et al.*, 2008; Cherniak and Watson, 2012; Kurz *et al.*, 2009; Recanati *et al.*, 2012; Shuster *et al.*, 2004; Trull *et al.*, 1991; Trull and Kurz, 1993). Such inclusions are evident in mantle xenoliths and exhumed peridotites (Andersen and Neumann, 2001; Brett *et al.*, 2015; Burnard *et al.*, 1994, 1998; Grozeva *et al.*, 2020; Hansteen *et al.*, 1998; Klein *et al.*, 2019; Pagé *et al.*, 2008; Zhang *et al.*, 2021). The abundance of inclusions and other He-accessible sites, their spatial relationship relative to mantle structures, and their influence on mantle He distribution and partitioning during melting can potentially be ascertained from study of obducted mantle rocks.

Mantle helium in massif peridotites is subject to confounding processes distinct from those in erupted rocks because exhumation may be complex, occurs over timescales many orders of magnitude longer than eruption, and is not necessarily monotonic or linear in pressure-temperature-time space. Peridotite massifs sustain temperatures transitional between mantle and Earth's surface for much longer durations than erupted rocks, and have had greater opportunity to deform, undergo phase transitions, and react with metasomatic fluids during ascent. These processes lead to a potentially complex interplay of temperature, time, composition, and location dependent phenomena that can modify the He systematics of the peridotite. For example, at temperatures ranging from ~50-600°C, serpentinization reactions between peridotite and aqueous fluids occur (Evans, 2010; Wunder *et al.*, 2001), extracting He by consumption of peridotite and promoting fracture and deformation. At temperatures above ~400°C, secondary inclusions form via annealing of fractures (Allen and Seyfried, 2003; Klein *et al.*, 2019; Wanamaker *et al.*, 1990), potentially trapping He from ambient fluids. These fluids may carry He released from earlier generations of inclusions either by diffusion or by rupture during deformation and fracturing.

He ingrowth from U and Th decay during and after emplacement may also be important. Diffusion data (Cherniak and Watson, 2012) indicates that radiogenic ^{4}He will accumulate in grain interiors once exhumation cools peridotite below about 300°C. The impact of this ingrowth on the He budget depends on the U, Th, and initial He concentrations, and the time since He closure (i.e., obduction). The U and Th concentration of peridotite is expected to be much lower than in erupted rocks, so ingrowth of ^{4}He will similarly be much smaller. Once at the Earth's surface, massif peridotites may accumulate ^{3}He from cosmic ray irradiation of the uppermost meter of the body.

The few previous studies (Francis, 2019; Grozeva *et al.*, 2020; Matsumoto *et al.*, 2001; Recanati *et al.*, 2012; Ye *et al.*, 2007) of peridotite massifs reveal some of the promise and complexity described above. For example, there is evidence that mantle He concentrations well in excess of those predicted from partition coefficients can be retained for more than 100 Myr after obduction (Recanati *et al.*, 2012; Ye *et al.*, 2007), and in some cases it is strongly associated with deformation fabrics and/or fluid inclusions (Grozeva *et al.*, 2020; Recanati *et al.*, 2012). However, serpentinization and both radiogenic and cosmogenic ingrowth are also sometimes evident from He isotope systematics (Francis, 2019; Grozeva *et al*., 2020). In this work we build on a cosmogenic ^{3}He dating study (Francis, 2019) of the Twin Sisters massif that revealed highly variable mantle-like He concentrations in fresh dunites and harzburgites very well-exposed over a few km^2 area by recent glacial retreat. Our goal is to better understand the spatial distribution, siting, and origin of He in a peridotite section in which these characteristics can be compared with peridotite structures visible in outcrop, hand sample, and thin section.

1.3 Geologic Setting

The Twin Sisters ultramafic complex (TSC) is exposed as a 16 km long, 6 km wide glaciated mountain ridge in the North Cascades of Washington State (Figure 1.1). The TSC probably formed in a suprasubduction or ocean basin setting (Kruckenberg *et al.*, 2013; Vance et al., 1980). An alternative interpretation that the TSC is an exhumed section of subcontinental lithospheric mantle (Christensen, 2002) is based on contested geologic observations (Frasse, 1981). The initial emplacement age of the complex is uncertain but likely Cretaceous based on structural relationships with surrounding rock units (Kruckenberg *et al*., 2013; Onyeagocha, 1978; Whetten *et al.*, 1980). The TSC is in fault contact with the Eocene Chuckanut Formation (Ragan, 1963), and the presence of TSC-sourced chromite grains in Chuckanut coals indicates the TSC was exposed by the Eocene (Brownfield *et al*., 1995). Frasse (1981) offered geomorphic evidence suggesting Holocene uplift in the range.

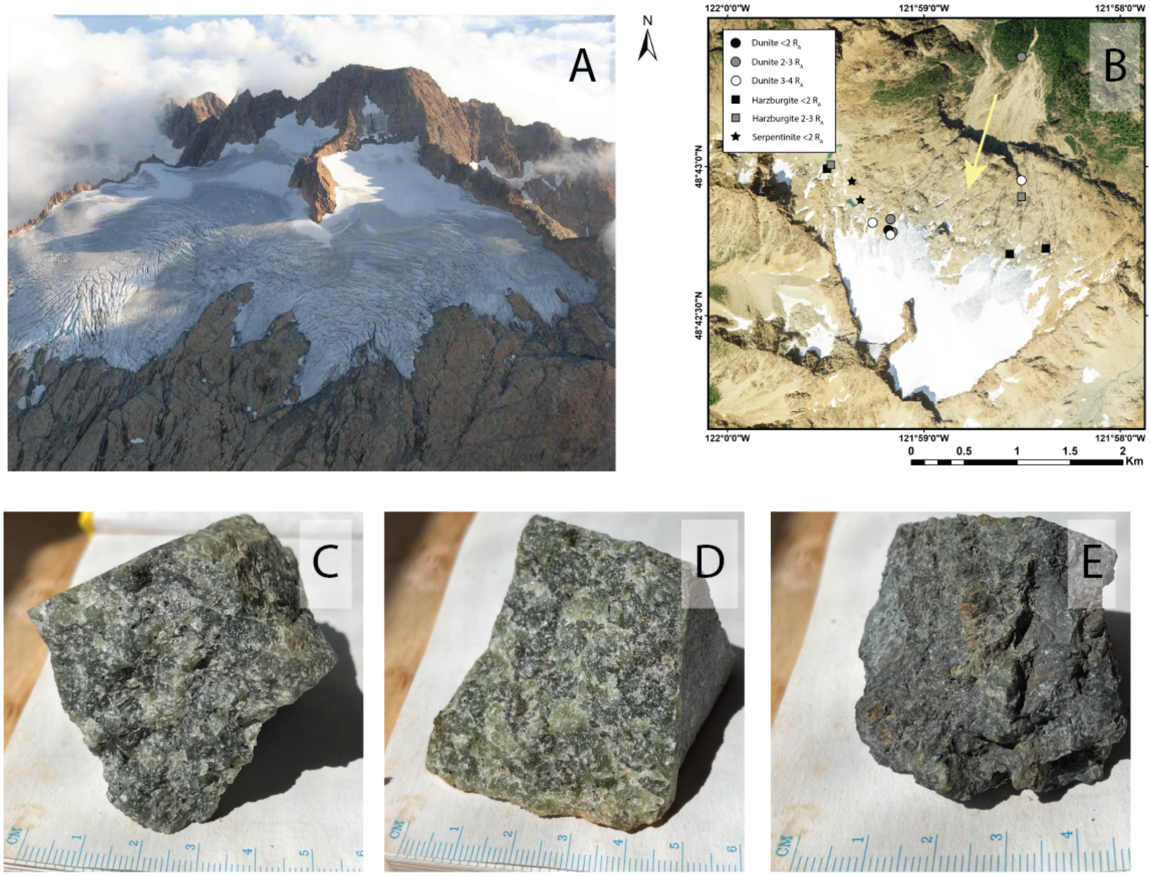

Dunite (20-TS-10)
Harzburgite (TS-TRAN-02)
Serpentinite (20-TS-01)

Figure 1.1 A) Oblique aerial image of northeast side of South Twin peak (Aug. 2005, courtesy J. Scurlock). View to southwest. Samples were acquired directly downslope of the retreating Sisters Glacier to minimize cosmic ray exposure. B) Sampling locations of the in-place samples and associated total ^{3}He/^{4}He ratios (image from USDA Farm Service Agency). Outcrop in images A and B is entirely peridotite. Representative hand sample images of C) dunite, D) harzburgite, and E) serpentinite.

Peridotites of the TSC consist of dunites, harzburgites, pyroxenite dikes, and chromite layers and pods (Onyeagocha, 1978; Ragan, 1963). Kruckenberg *et al.* (2013) and Toy *et al.* (2010) reported mantle structures and fabrics including plastically-sheared peridotite, mylonites, and tabular dunite bodies likely produced by melt infiltration and reaction (Braun and Kelemen, 2002, 2002; Kelemen *et al.*, 1995, 1997). Peridotite equilibration and deformation occurred at high temperatures (600-1300°C) consistent with the lithospheric mantle (Onyeagocha, 1978; Toy *et al.*, 2010). Shear zones in the TSC formed at lower temperatures (~600-700°C) than the host peridotite (~800-1300°C), which is consistent with shearing of the cooling and exhuming massif (Onyeagocha, 1978; Toy *et al.*, 2010).

Although the TSC is inferred to be underlain by a serpentinite keel at a depth of 1-2 km below the surface (Thompson and Robinson, 1975), much of the exposed TSC shows little or no evidence of serpentinization. Serpentine is restricted to the margins of the massif, in a few large shear zones in the interior, and in occasional small veins that crosscut the olivine and pyroxene grains (Christensen, 2002). In part, the remarkably fresh appearance of many TSC peridotites may arise from Holocene glacial denudation (Francis, 2019).

1.4 Materials and Methods

1.4.1 Sampling

Glacial erosion has exposed many square km of fresh peridotite on the east-facing slopes of the Twin Sisters ridge (Figure 1.1). Francis (2019) collected samples on several transects across a shallowly-sloping bench on the northeast flank of South Twin peak, at elevations ranging from about 1.3 to 1.7 km. Francis (2019) also collected samples further downslope

(~1 km elevation), beyond the extent of neoglacial erosion, and from the Sven Larsen olivine quarry at the northernmost edge of the peridotite body. All of the Francis (2019) samples may contain cosmic-ray produced ^{3}He except those from the quarry. We reanalyzed some of the Francis (2019) samples for methodological consistency and use them in this study only when the potential for a cosmogenic ^{3}He component is not problematic.

We collected 36 additional samples from immediately downslope of the retreating Sisters Glacier, overlapping the highest elevations in the Francis (2019) suite (Figure 1.1B, Table 1.S1). This area is glacially polished with near-complete exposure (Kruckenberg *et al.*, 2013; Toy *et al.*, 2010), providing an opportunity to relate samples to field-scale lithologic structures. All samples from this new suite were collected in a region that was glacially covered in images from 1927 (Francis, 2019) to minimize potential cosmogenic ^{3}He. Most samples are from bedrock, although a few boulders were sampled to broaden lithologic diversity and to facilitate highly-spatially-resolved sampling transects across interesting features. Samples were obtained from the major Twin Sisters lithologies (Ferré *et al.*, 2005; Kruckenberg *et al.*, 2013; Onyeagocha, 1978; Ragan, 1963; Tikoff *et al.*, 2010; Toy *et al.*, 2010): massive harzburgite, tabular dunite bodies, early-stage orthopyroxene veins, chromite-bearing veins, thin late-stage pyroxenite veins, and highly localized bodies of black and fractured material that appeared serpentinized. Several sampling transects were acquired across distinctive structures in the peridotite (Table 1.S2 in Appendix 1.A) to assess how those structures may relate to He data. For example, the sequence of samples labelled TS-TRAN were taken at few cm intervals over 42 cm spanning a tabular dunite body and including the adjacent harzburgite. Further details of the new samples are provided in Table 1.S2 and Figure 1.S2 in Appendix 1.A.

Twin Sisters dunite hand samples typically contain >90 vol% olivine (~50-micron to ~5-centimeter diameter grains) with minor orthopyroxene and chromite in some samples. Harzburgite hand samples carry ~50-20 vol% orthopyroxene and ~50-80 vol% olivine, and often host minor chromite. Sparse chromite pods and tabular bands observed in the Twin Sisters consist of ~40-80 vol% chromite associated with pyroxene and olivine. Orthopyroxene dikes are comprised of ~100 vol% orthopyroxene and crosscut magmatic band-like features defined by the harzburgite and dunite but are deflected by deformation fabrics in the peridotite. Clinopyroxene-bearing dikes consisting of ~50-100% clinopyroxene with ~0-50% orthopyroxene crosscut band-like magmatic and deformation-related shear-zone features in the harzbugites and the dunites. Some composite veins were observed, with clinopyroxene in the core and orthopyroxene on the rims. Secondary serpentinite minerals filling fractures are present in some peridotite hand samples but are usually << 1vol% of the rock. A few hand samples analyzed here are referred to as serpentinites and are made up of >50% serpentine minerals by volume (mostly lizardite). These rocks often occur along joints, fractures, and fault surfaces, or as a brecciation fabric.

1.4.2 Sample preparation

After thin-section preparation, hand samples were crushed to <2-mm size in a jaw crusher. This crushate was the starting material for further sample preparation described in the subsections below. Most analyzed samples consist of whole rock. However, nearly pure olivine, orthopyroxene, or clinopyroxene separates were obtained for some analyses by handpicking on the basis of color, cleavage, and habit.

1.4.3 Vacuum crushing

Vacuum crushing was used to preferentially extract He from fluid inclusions from a total of 51 whole rock samples and mineral separates while avoiding matrix-associated He (Blard *et al.*, 2008; Kurz *et al.*, 2009). One-to-two-gram samples were sieved to between 0.36 and 2 mm, washed in Milli-Q water, dried at ~100°C, and crushed in vacuum in two sequential steps of two minutes each following the method of Blard *et al.* (2008). Blank measurements were performed by activating the crusher prior to dropping the sample onto the crusher anvil. Blank levels (maximum 0.03 ncc STP of ^{4}He and 0.4 fcc ^{3}He) were small (<5%) compared to He extracted from the samples. Nonetheless, blank corrections were made to sample measurements.

1.4.4 Powder fusion

Fusion analysis of powdered samples ("powder fusion") was employed on a total of 51 whole rock samples and mineral separates in an attempt to isolate matrix helium by removal of large fluid inclusions prior to analysis (Kurz *et al.*, 1990). Material selected for powder fusion consisted of either the powder left over from the vacuum crushing analyses or new aliquots selected from the same batch of sieved grains. The selected material was ground by hand with an agate mortar and pestle rendering powder comprised of <~30-micron grains. Addition of atmospheric helium during grain size reduction (Protin *et al.*, 2016) was prevented by grinding under ethanol (Cox *et al.*, 2022). 50-200 mg aliquots of each sample were washed with ethanol, air-dried in a petri dish, weighed, and wrapped in a tin (Sn) foil capsule. Samples were loaded into a double-walled vacuum furnace and pumped for at least 8 hours, after which the furnace was degassed (Patterson *et al.*, 1997). Some samples were melted using lithium borate flux at ~1000°C for 15-25 minutes in a molybdenum liner (Farley *et al.*, 2020), but most were degassed at ~1400°C for 15-25 minutes without flux in a carbon liner. Helium extraction via the lithium borate flux method was done to extend the life of the furnace and to minimize blank levels. Hot furnace blanks were measured prior to each furnace sample run. Re-extracts (a second heating/analysis of the outgassed sample) were conducted to confirm complete He extraction and in all cases yielded blank level He. Maximum blank levels of 0.5 fcc STP ^{3}He and 0.2 ncc STP ^{4}He were small (<5%) relative to He extracted from the samples. Nonetheless, blank corrections were made to sample measurements.

1.4.5 Step heating

Step heating of seven samples was undertaken to assess whether isotopically different He isotopic components reside in distinct sites within the mineral grains. Between ~0.3 and 2 gram aliquots of powdered sample were wrapped in Sn foil capsules and loaded in the dropper arm of the double-walled furnace as described above. Prior to analyses, the furnace was degassed at 1410°C for one hour. Samples were dropped into the furnace and heated stepwise for 40 minutes, reaching and maintaining peak temperatures ranging from 490-1410°C (see Table 1.S3 for temperature steps), with a cooling time of ~20 minutes between steps. Furnace temperatures were calibrated as a function of furnace output power using a thermocouple and a dual-wavelength pyrometer prior to sample step heating and have an estimated uncertainty of 20°C – 85°C depending on setpoint. He blanks were measured at 490°C and 1410°C. Maximum blank levels were 0.8 fcc STP ^{3}He and 0.02 ncc STP ^{4}He for all steps except for sample 20-TS-02 D in which the ^{4}He blank was 0.33 ncc-STP ^{4}He. These blanks were generally small compared to sample He (<5%), and an average of these two blanks was subtracted from each step and the standard deviation of the blanks was propagated through the uncertainty analysis.

1.4.6 Helium measurement

Helium was purified and analyzed as described previously (Horton *et al.*, 2019). Briefly, for furnace analyses, the gases extracted from the samples were passed through a charcoal U-trap at 77 K to remove most contaminants (e.g., CO_2, H_2O, Ar). Noncondensable gases were then passed over a hot SAES NP10 getter to eliminate reactive species except H_2, which was subsequently removed on a second, cold, SAES NP10 getter. Helium was then cryofocused at 14 K on charcoal and released into the mass spectrometer at 34 K. Samples extracted by crushing were run identically, except no charcoal U-trap was employed.

Helium measurements were made on a Helix SFT mass spectrometer at Caltech with ^{3}He detected on a pulse-counting electron multiplier and ^{4}He on a Faraday cup. A standard containing about 70 ncc of He with ^{3}He/^{4}He of 2.05 Ra was run consistently throughout the study. This standard was synthesized from pure ^{3}He and pure ^{4}He using capacitance manometry and both abundance and ^{3}He/^{4}He ratio accuracy are better than 1%. This standard was split, and multiple shots were analyzed, to characterize mass spectrometer pressure nonlinearity. Sensitivity for each isotope for each sample was obtained by interpolation between standards bracketing the sample ^{4}He peak height.

1.4.7 Argon measurement

Ten samples were analyzed for Ar concentration and isotopic composition by powder fusion extraction in the double-walled furnace. 40-70 mg aliquots of sample were wrapped in Sn foil, loaded in the dropper arm, evacuated, and baked at ~200°C for ~3 days. Simultaneously, lithium borate flux was loaded into a molybdenum furnace liner and degassed at ~1000°C for one hour three times during the baking period. The borate flux method was used to reduce the extraction temperature and thereby minimize the blank (Farley *et al.*, 2020). Following a hot blank measurement of the flux, samples were dropped into the liner and fused in the flux at ~1000°C for ~20 minutes. Re-extracts were conducted until Ar extracted was consistent with the initial blank signal. Extracted gases were purified as described above for He, but no charcoal trap was used, and Ar was not cryofocused. Ar was analyzed on a Helix MC mass spectrometer at Caltech with simultaneous detection of all Ar isotopes on Faraday detectors. A standard of known abundance of atmospheric Ar was analyzed for calibration. Blank corrections were below 4.4 pcc STP ^{36}Ar and below 1.8 ncc ^{40}Ar. While the blank accounted for as much as ~40% of some of the low-Ar samples, the blanks were reproducible to the extent that all Ar analyses were above the lower limit of quantification.

1.4.8 U and Th concentrations

U and Th concentrations were measured on seven samples by isotope dilution ICP-MS analysis after purification on columns based on the method described by Lao *et al.* (1993). Whole rock samples of ~5 grams each of <2 mm diameter grains were ground to powder under atmosphere using an agate mortar and pestle. Aliquots of 400±20 mg were weighed, spiked with ^{230}Th and ^{235}U, digested in 2:1 concentrated hydrofluoric acid : nitric acid and subsequently in concentrated hydrochloric acid, and purified on AG1-X8 resin in 8M nitric acid. In some samples a very small amount of undigested chromite was observed and removed prior to column separation. Two or more aliquots of each sample were processed, and three or more equivalently-spiked procedural blanks were run in conjunction with the samples.

Solutions were analyzed on an Agilent triple quadrupole 8800 ICP-MS at the Caltech Water and Environment Laboratory for Th and U isotopes.

Blank corrections were typically 20-25 pg U and 15-30 pg Th, sometimes constituting a significant fraction of the observed concentration, from 2-30% for U and 2-15% for Th. Analytical uncertainties were propagated through the isotope dilution equation using the uncertainties of the known amount of spike added to the samples, uncertainties in the measurements, and the natural isotopic abundances of ^{235}U, ^{238}U, ^{230}Th, and ^{232}Th. Average blank-corrected concentrations of replicates are reported (Table 1.3). We observed occasional discrepant very high concentrations on replicate analyses that we attribute to sporadic particulate contamination. Within a suite of replicate analyses, outlying (high) concentrations that deviated more than 5 σ from other replicates were rejected from the reported replicate mean concentration but are reported in the text associated with Table 1.S4 of Appendix 1.A.

Standard error (σ_M) was estimated for the average concentrations of U and Th in samples by normalizing individual replicate concentrations to corresponding mean concentrations and taking the standard deviation of all the normalized replicate values (σ_{frac}). To estimate the σ_M for the average U and Th concentrations in each sample, the σ_{frac} values for U (0.105) and Th (0.302) were multiplied by the average concentrations of U and Th in each sample and normalized to the square root of the number of replicate analyses of each sample (Table 1.3).

To verify this method, we also analyzed U and Th concentrations on three replicates of powdered USGS geochemical reference material DTS-2b (lot 1607), coincidentally a dunite from the Sven Larsen olivine quarry in the TSC (Skeen and Crandell, 2003). The U concentration we measured (1.9 ± 0.1 ppb) is consistent with published values of 1.7-2.4 ppb (Debret *et al.*, 2019; Robin-Popieul *et al.*, 2012; Rospabé *et al.*, 2018a, 2018b; Zhang *et al.*, 2019). Our Th concentration of 2.9±0.5 ppb is also within the range of reported values (2.9-4.1 ppb; Debret *et al.*, 2019; Robin-Popieul *et al.*, 2012; Rospabé *et al.*, 2018a, 2018b; Zhang *et al.*, 2019).

1.5 Results

1.5.1 Helium concentrations

He concentrations extracted by crushing (^4He_C) of dunite and harzburgite span about 1 to 100 ncc STP/g, with most samples yielding less than 30 ncc/g (Table 1.1, Figure 1.2A). The highest concentrations are among the harzburgites, although both lithologies yield a wide spread in concentrations (Figures 1.2A, 1.S1). Other mantle lithologies (orthopyroxene veins and clinopyroxene-bearing veins) also plot in this concentration range. Helium concentrations extracted by fusion of powder (^4He_F) are higher than those extracted by crushing for almost every sample, spanning 2 to 450 ncc/g (Figure 1.2A). There is a strong correlation between the two concentrations, with $^{4}\mathrm{He}_{C}$ typically ~30% of $^{4}\mathrm{He}_{F}$ (Figures 1.2A, 1.S1C).

Table 1.1. Helium concentrations and isotope ratios determined by vacuum crushing (C) and powder fusion (F) of Twin Sisters whole rock dunite (Dun), harzburgite (Harz) and serpentinite (Serp) samples and orthopyroxene (OPX), olivine (OL), and clinopyroxene (CPX) mineral separates. The "v" subscript indicates an isolated vein in the hand sample as opposed to the bulk peridotite, which was otherwise analyzed. The asterisk (*) indicates analyses from Francis (2019) — cosmic ray exposure is possible. Underlined powder fusion data highlight analyses in which helium extraction was conducted in a molybdenum liner in lithium borate flux at ~1000°C. Otherwise, powder fusion analyses were undertaken in a carbon liner at ~1400°C (see Section 1.4.4).

Sample	Lithology	$^{4}\mathrm{He}_{C}$	±σ	$^{3}\mathrm{He}/^{4}\mathrm{He}_{C}$	±σ	$^{4}\mathrm{He}_{F}$	±σ	$^{3}\mathrm{He}/^{4}\mathrm{He}_{F}$	±σ
		(ncc STP/g)		(R_A)		(ncc STP/g)		(R_A)	
20-TS-02 CL	Dun	23.5	0.7	1.53	0.06	117	3	1.51	0.05
20-TS-02 D	Dun	29.9	0.9	1.64	0.06	129	4	1.57	0.06
20-TS-02 CD	Dun	13.1	0.4	1.58	0.06	82	2	1.59	0.05
20-TS-03	Dun	6.5	0.2	2.7	0.1	19.0	0.6	2.58	0.09
20-TS-04	Dun	19.0	0.6	1.73	0.06	56	2	1.80	0.07
20-TS-05	Dun	8.7	0.3	2.46	0.09	23.8	0.7	2.71	0.09
20-TS-06	Dun	9.9	0.3	3.5	0.1	15.3	0.4	4.0	0.2
20-TS-07	Dun	5.4	0.2	2.51	0.09	15.1	0.4	3.2	0.1
20-TS-08	Dun	5.1	0.2	3.1	0.1	13.0	0.4	3.8	0.2
20-TS-09	Dun	19.5	0.6	2.31	0.09	51	2	2.8	0.1
20-TS-10	Dun	9.6	0.3	4.6	0.2	20.1	0.6	6.1	0.2
20-TS-14	Dun	2.5	0.1	4.0	0.2	8.7	0.3	4.1	0.2
20-TS-18	Dun	8.0	0.2	5.9	0.2	19.4	0.6	5.1	0.2
TS-TRAN-00	Harz	4.4	0.1	2.8	0.1	5.2	0.5	3.7	0.4
TS-TRAN-02	Harz	3.3	0.1	2.28	0.08	6.4	0.2	3.4	0.3
TS-TRAN-04	Dun	2.2	0.1	2.34	0.09	8.8	0.3	2.7	0.1
TS-TRAN-08	Dun	1.7	0.1	2.8	0.2	7.2	0.2	3.6	0.3
TS-TRAN-12	Dun	4.9	0.1	4.1	0.2	14.2	0.4	3.9	0.1
TS-TRAN-16	Dun	3.6	0.1	3.7	0.2	11.5	0.3	4.0	0.2
TS-TRAN-20	Dun	2.9	0.1	3.6	0.3	10.3	0.3	4.4	0.2
TS-TRAN-24	Dun	3.7	0.1	3.1	0.2	12.1	0.3	3.3	0.2
TS-TRAN-28	Dun	4.8	0.1	3.8	0.1	19.7	0.6	3.9	0.1
TS-TRAN-32	Dun	5.0	0.1	3.6	0.1	15.4	0.4	3.9	0.2
TS-TRAN-34	Dun	5.6	0.2	5.5	0.2	10.2	0.4	4.9	0.3

Sample	Lithology	^4He_C	$\pm\sigma$	$^3He/^4He_C$	$\pm\sigma$	^4He_F	$\pm\sigma$	$^3He/^4He_F$	$\pm\sigma$
		(ncc STP/g)		(R_A)		(ncc STP/g)		(R_A)	
TS-TRAN-36	Dun	2.2	0.1	3.7	0.3	6.2	0.2	5.7	0.5
TS-TRAN-42	Dun	2.9	0.1	2.9	0.2	11.0	0.3	4.0	0.2
20-TS-11	Dun	6.9	0.2	1.95	0.07	43	1	2.09	0.08
20-TS-11	OPX$_v$	3.7	0.1	2.26	0.09	12.1	0.3	3.3	0.1
20-TS-12	Harz	2.71	0.1	2.06	0.07	15.7	0.4	2.3	0.1
20-TS-13	Harz	3.01	0.1	1.85	0.09	15.9	0.4	1.96	0.09
20-TS-13	Harz (OL)	3.9	0.1	1.7	0.1	20.9	0.6	1.20	0.09
20-TS-13	Harz (OPX)	1.7	0.1	2.5	0.2	8.5	0.3	2.3	0.2
20-TS-16	Harz (OL)	9.3	0.3	1.9	0.1	24.3	0.7	2.12	0.08
20-TS-16	CPX$_v$	46	1	0.65	0.02	68	2	0.83	0.03
20-TS-01	Serp	0.22	0.01	1.8	0.3	12.3	0.3	0.93	0.06
20-TS-15	Serp	10.8	0.3	1.08	0.04	70	2	1.19	0.04
T1S6	Dun	14.6	0.6	2.2	0.1	17.4*	0.5	5.4*	0.2
T2S1	Dun	24.1	0.7	2.6	0.1	22.2*	0.6	3.8*	0.1
T1S1	Harz	45	2	1.68	0.07	132	4	1.80	0.07
T1S7	Harz	0.90	0.03	2.3	0.2	2.21*	0.06	18.6*	0.8
T1S8	Harz	1.00	0.03	1.2	0.1	2.22*	0.06	42*	2
T2S3	Harz	87	3	2.03	0.08	207	6	2.07	0.08
T2S8	Harz	101	3	1.44	0.06	446	13	1.55	0.05
_LL2_	_Dun_	_22.6_	_0.7_	_1.63_	_0.06_	_60*_	_2_	_3.1*_	_0.1_
_LL6_	_Dun_	_1.1_	_0.3_	_3.0_	_0.9_	_3.2*_	_0.1_	_19.0*_	_0.7_
Grey TW	**Dun**	**22.1**	**0.6**	**0.89**	**0.03**	**66**	**2**	**0.79**	**0.03**
SLD 02	**Dun**	**14.9**	**0.4**	**2.48**	**0.09**	**39**	**1**	**1.65**	**0.05**
SLQ 10	**Dun**	**31.5**	**0.9**	**0.90**	**0.04**	**71**	**2**	**1.02**	**0.04**
SLD 01	**Harz**	**2.1**	**0.1**	**2.8**	**0.1**	**15.4**	**0.4**	**2.18**	**0.09**
SLQ 7	**Harz**	**26.2**	**0.8**	**1.24**	**0.04**	**20.8**	**0.6**	**2.74**	**0.09**
_TS05-GL_	_Dun_	_23.1_	_0.7_	_3.7_	_0.1_	_66_	_2_	_3.0_	_0.1_

Note: Samples starting with LL, T1, T2 and SLD are from Francis (2019), reanalyzed here. Samples in bold are from Sven Larsen quarry. Samples in italics are from surface outcrop more than 500 meters from the retreating Sisters Glacier.

Both ^4He_F and ^4He_C vary over short outcrop length-scales (Tables 1.1 and 1.S2 and Figure 1.S2), e.g., varying up to ~4-fold in samples collected 10 cm apart, ~3-fold in samples collected 5 cm apart and ~2-fold in samples collected 2 cm apart. The harzburgites (TS-

TRAN-00 and TS-TRAN-02) directly adjacent to the dunite band in Transect 5 have very similar He concentrations to the adjacent dunite sample from the edge of the band (TS-TRAN-04).

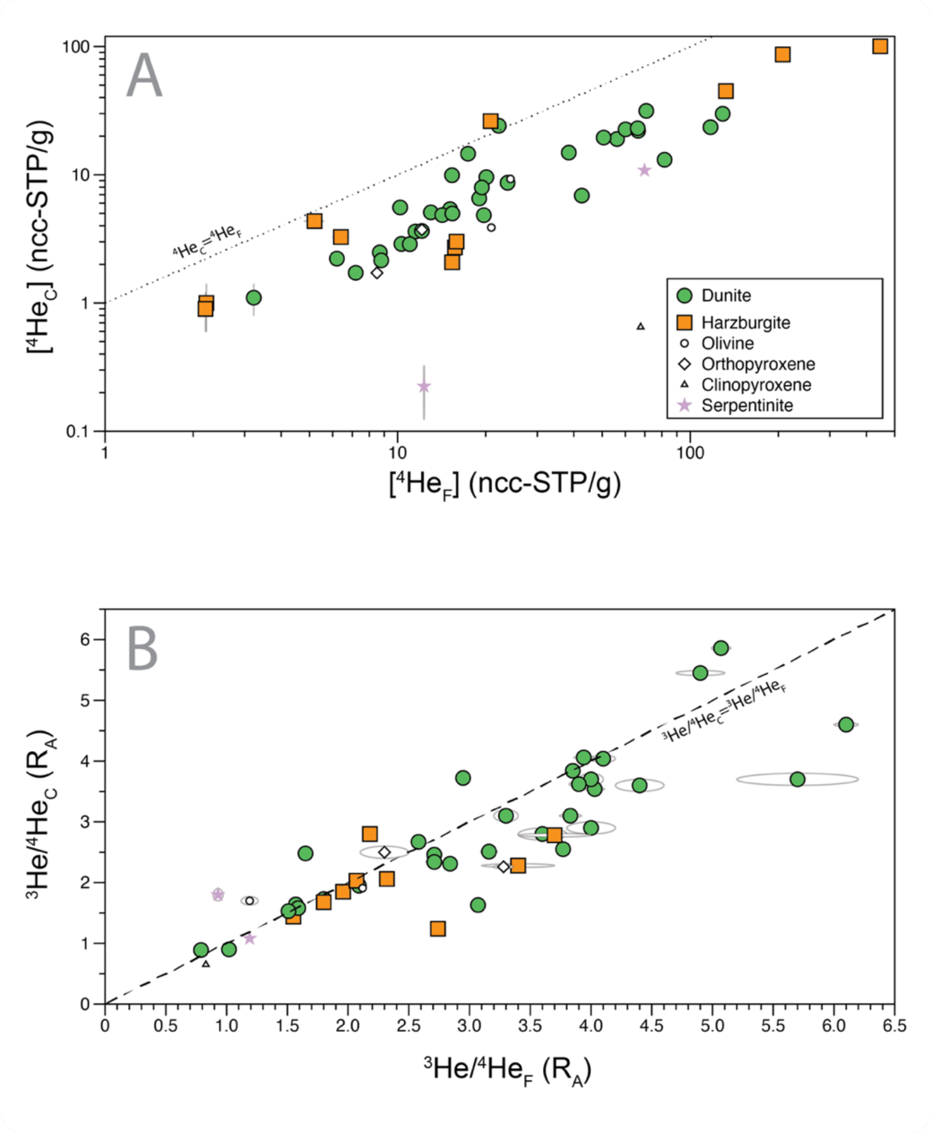

Figure 1.2. Comparison of A) He concentrations and B) ^{3}He/^{4}He ratios obtained by crushing and by powder fusion analysis. Crush and powder fusion analyses are distinguished by "C" and "F" subscripts respectively. Samples from Francis (2019) with ^{3}He/^{4}He$_F$ >18 R$_A$ are presumed to be influenced by cosmogenic ^{3}He and are not shown. Dunite, harzburgite, and serpentinite symbols denote whole rock analyses of each lithology; other symbols indicate mineral separates.

The vein serpentinite sample 20-TS-01, which is ~100% serpentine minerals with trace relict olivine and pyroxene grains, has a notably low ^4He_C of just 0.2 ncc/g, associated with a ^4He_F of 12 ncc/g. In contrast, the brecciated serpentinite sample (20TS-15), with ~50% serpentine minerals and ~50% pyroxene and olivine, has concentrations similar to mantle lithologies.

1.5.2 Helium isotope ratios

Excluding samples that were expected to have cosmogenic ^3He (i.e., most of those from Francis, 2019), $^3He/^4He$ ratios in harzburgites and dunites extracted by both crushing and fusion vary from ~1 to ~6 R_A (Table 1.1, Figure 1.2B); only three samples yielded $^3He/^4He$ ratio lower than the atmospheric ratio, ranging from 0.7 to 0.9 R_A. The highest $^3He/^4He$ ratios occur in the dunites; for example, of the 14 samples with fusion $^3He/^4He$ ratios higher than 3.7 R_A, all are dunites. $^3He/^4He$ ratios measured by crush extraction are broadly correlated with those obtained by fusion (Figure 1.2B), with a clear tendency for ratios to be higher in the fusion than in the crush. Because the isotopic ratios obtained by crushing and fusion are similar, in much of what follows we frequently discuss the characteristics of the total He (He_T) extracted from the samples (He_T=He_C + He_F) with regard to both He concentrations and isotope ratios.

$^3He/^4He$ ratios lower than atmospheric occur in a clinopyroxene separate from a clinopyroxenite vein, and in dunites SLQ 10 and Grey-TW, which are both from the Sven Larsen quarry. The two serpentinite samples yielded $^3He/^4He$ ratios between ~0.9 and 2 R_A.

Like He concentrations, He isotope ratios vary significantly over cm length-scales, e.g., from 2.7 to 4 R_A across 10 cm in the fusion analyses of 20-TS-05 and 20-TS-06, and from

3.7 to 5.5 R_A over just 2 cm in the crush analyses of TS-TRAN-34 and TS-TRAN-36 (Tables 1.1 and 1.S2 and Figure 1.S3). Similar variation occurs even between minerals in a single sample: in harzburgite 20-TS-13, orthopyroxene yielded 2.3 R_A by fusion and 2.5 R_A by crushing while olivine yielded 1.2 R_A by fusion and 1.7 R_A by crushing.

1.5.3 He concentration - isotope ratio relationships

Samples with the highest He concentrations generally have the lowest $^3He/^4He$ ratios, and vice versa. This is well-illustrated in a mixing diagram plotting $(^3He/^4He)_T$ as a function of $1/[^4He_T]$, in which mixing between endmembers with constant He isotope ratios and concentrations plot along a straight line (Figure 1.3). All mantle lithologies lie in or near a triangular region with one apex at $1/[^4He_T]=0$ and a $^3He/^4He$ ratio of 1 ± 0.5 R_A. The upper bound of the triangle is defined by $^3He/^4He$ ratios of about 5.5-6 R_A. At any given $1/[^4He_T]$, the harzburgites tend to plot at lower $^3He/^4He$ than the dunites. A nearly identical pattern is observed when crush and fusion results are plotted separately (not shown). Although the serpentinite sample that contains ~50% unreacted olivine and orthopyroxene (20-TS-15) plots near the high concentration apex and within the range of the mantle lithologies, the completely serpentinized sample (20-TS-01) has a much lower He concentration for its $^3He/^4He$ ratio (i.e., plots well below the triangle bounding the other data points).

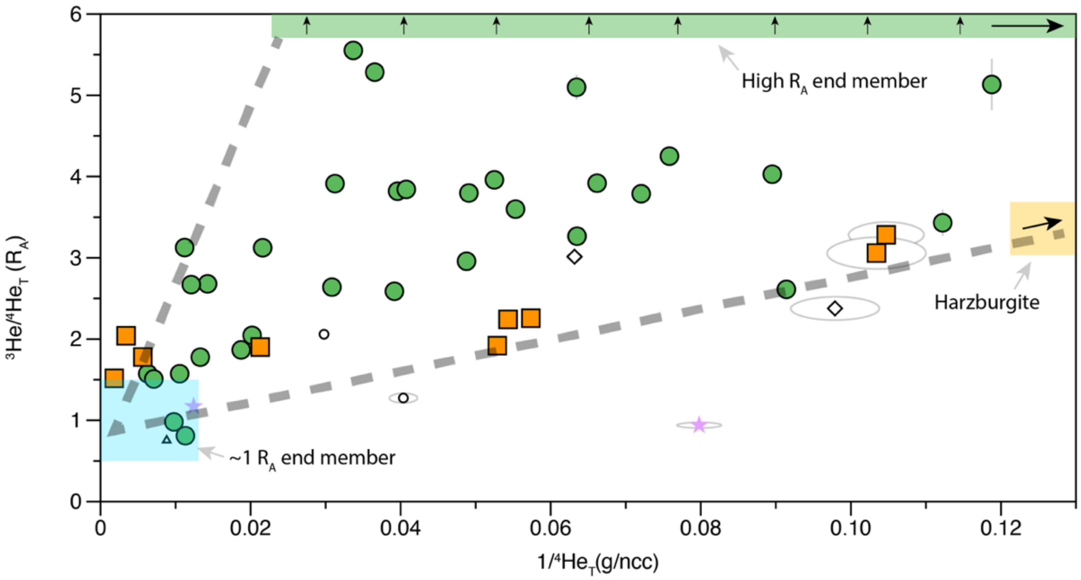

Figure 1.3. Helium concentration – $^3He/^4He$ ratio mixing diagram in which the data define a triangular field (grey dashed lines) bounded by endmembers with a $^3He/^4He$ ratio of ~1 R_A (blue field) and a high R_A mantle-like endmember with $^3He/^4He$ ratio around 6 R_A (green field). The harzburgites project from the ~1 R_A endmember along harzburgite array to at least ~3.0-3.5 R_A (orange field). The "T" subscript indicates total He where He_T is the sum of the He concentrations determined by crushing and powder fusion. Samples from Francis (2019) with $^3He/^4He_F$ ratios >18 R_A are presumed to be influenced by cosmogenic ^3He and are not shown. Black arrows indicate that mantle endmembers may extend to lower He concentrations and possibly higher $^3He/^4He$ ratios.

1.5.4 Step heating

Seven samples were selected for step heating: one serpentinite (20-TS-15), three dunites (20-TS-02-D, Grey TW and TS05-GL), two harzburgites with very high He concentration (T2S8 and T1S1) and one harzburgite with a low He concentration (T1S8). Although samples TS05-GL, T2S8, T1S1, and T1S8 all may have experienced some cosmic ray exposure, only T1S8 has obvious cosmogenic ^3He in the powder fusion analysis, indicated by a $^3He/^4He$ ratio of 42 R_A (Francis, 2019). This sample was analyzed specifically to provide insight to the temperature range over which cosmogenic ^3He is released.

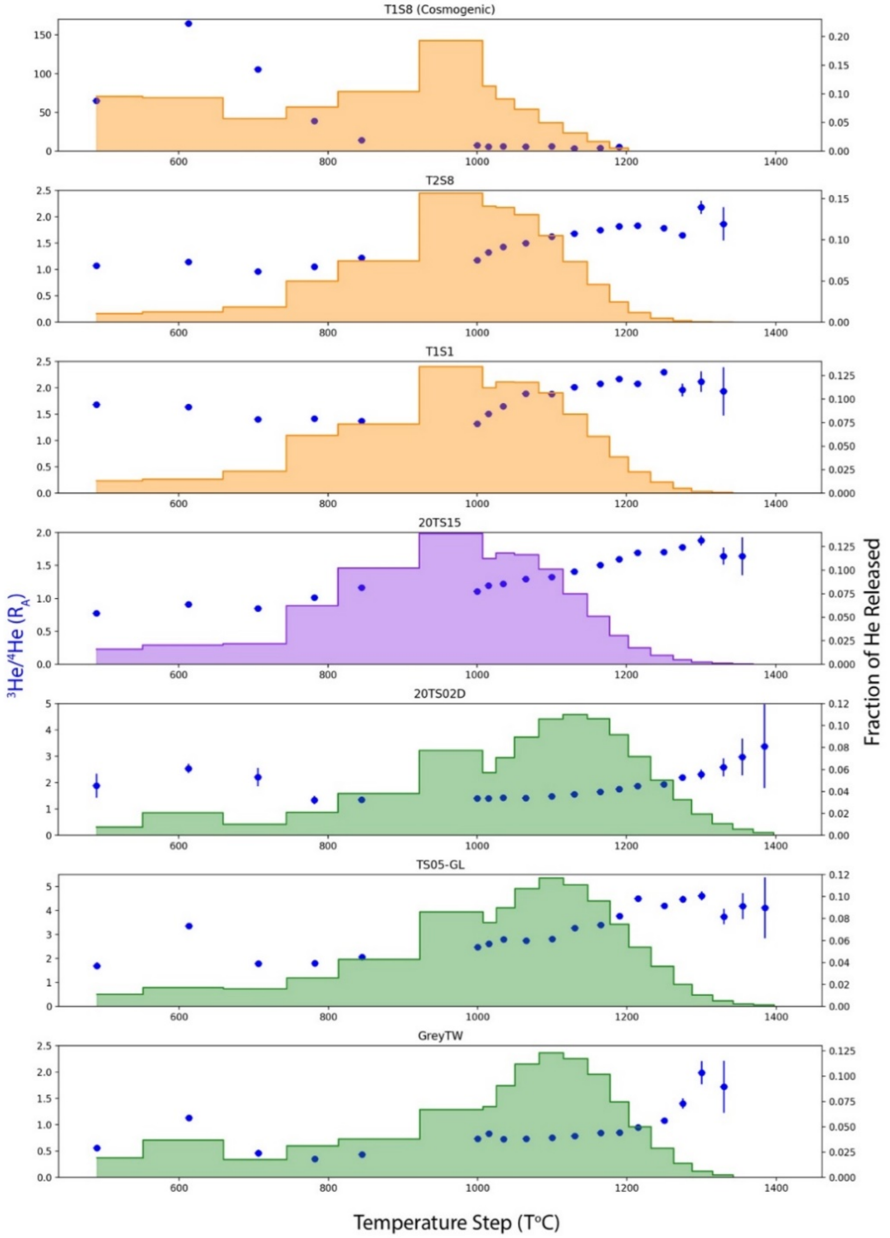

Figure 1.4. Step heating results. Histograms (orange-harzburgite, green-dunite, purple-serpentinite) represent fractional yield of He in each step; blue points indicate the step ^{3}He/^{4}He ratio. All samples except cosmic ray exposed T1S8 tend to yield higher ^{3}He/^{4}He ratios in the higher temperature steps. Sample T1S8 has a ^{3}He/^{4}He ratio peak at lower temperature, indicating extraction of matrix hosted cosmogenic He peaking at ~600°C.

With the exception of T1S8, the samples exhibit consistent step-heating behavior (Figure 1.4 and Table 1.S3). Fairly uniform and low ^{3}He/^{4}He ratios were extracted over the first five temperature steps up to 1000°C, after which the ratios climb steadily, typically achieving their maximum in the steps >1250° C. The low ^{3}He/^{4}He component extracted at low temperatures (≤ 1000°C) is not isotopically the same in every sample. For example, in sample T2S8 the low temperature steps are near 1 R_A, but cluster around 1.5 R_A in T1S1. In Grey-TW, the low temperature steps are as low as 0.4 R_A. The highest ^{3}He/^{4}He ratio measured in a single temperature step in each of these samples is also variable, ranging from 1.8 to 4 R_A. In every case except T1S8, the crushing and powder fusion ^{3}He/^{4}He ratio results are bounded by the extremes of the step heat data points, indicating that the isotopic components isolated by step heating are mixed in the crushing and fusion extractions.

At low temperatures, the step-heating profile of the cosmic-ray exposed sample T1S8 exhibits elevated ^{3}He/^{4}He ratios (up to 165 R_A) compared to other samples. Unambiguously cosmogenic ^{3}He/^{4}He ratios (i.e., >8 R_A) cease at temperatures greater than 845°C. Above this temperature helium isotope ratios generally decline, from 7.6 R_A to 3 R_A. From these observations we conclude that the majority of cosmogenic ^{3}He is released below ~1000°C. The He isotope ratio determined by crushing of this sample, 1.2 R_A, is lower than the ^{3}He/^{4}He ratios determined in any individual temperature step, presumably because the cosmogenic component is not present in the fluid inclusions opened by crushing.

Dunite samples exhibit peak release temperatures higher than those of harzburgites. The highest fractional extraction of He from dunite samples occurred between 1130 and 1165°C, whereas in the harzburgite samples the highest fractional release occurred during the 1000°C step (Figure 1.4).

The serpentinized sample 20-TS-15 yielded a step-heating pattern almost identical to the harzburgites, with $^{3}He/^{4}He$ ratios of 0.75-1.2 R_A up to ~1000°C, and then rising steadily to a ratio of almost 2 R_A in the highest temperature steps. The He yield profile also looks remarkably similar to the harzburgites, with the maximum He extraction at ~1000°C. This suggests the He in this sample is hosted in the surviving mafic minerals rather than in serpentine minerals.

1.5.5 Argon

Argon isotopes were measured on seven dunite and three harzburgite samples that span nearly the entire range of $^{4}He_F$ (19 to 450 ncc/g) and $^{3}He/^{4}He_F$ (0.79 to 6.1 R_A). Argon concentrations range from 75 - 1980 ncc/g and all $^{40}Ar/^{36}Ar$ ratios are within 1σ uncertainty of the atmospheric ratio with the exception of the sample with the highest $^{3}He/^{4}He$ ratio (20-TS-10; $^{40}Ar/^{36}Ar$ =357±23 vs ~297±2 in atmosphere: Lee *et al.*, 2006; Mark *et al.*, 2011; Valkiers *et al.*, 2010; see Table 1.2 and Figure 1.5A). Concentrations of all He and Ar isotopes are linearly correlated with each other over almost a factor of 10 in concentration, and the correlation lines pass close to the origin (Figure 1.S3). Only one sample deviates substantially from this trend, harzburgite T2S8, which has about twice as much ^{4}He as expected from the ^{40}Ar-^{4}He correlation observed among the other samples (Figure 1.S3). $^{40}Ar/^{4}He$ ratios range from 3 to 12 compared to the atmospheric ratio of almost 1800 (Porcelli and Ballentine, 2002). These ratios do not appear to correlate with $^{3}He/^{4}He$, nor is there a clear distinction between harzburgites and dunites (Figure 1.5B).

Table 1.2. Ar concentrations and $^{40}Ar/^{36}Ar$ ratios determined by powder fusion of Twin Sisters peridotite whole rock samples.

Sample	Lithology	^{40}Ar ncc/g	±σ	$^{40}Ar/^{36}Ar$	±σ
20-TS-02 D	Dun	1037	55	305	20
20-TS-03	Dun	207	11	295	19
20-TS-04	Dun	676	36	305	20
20-TS-10	Dun	127	7	357	23
20-TS-18	Dun	97	5	290	19
Grey TW	Dun	205	11	306	20
TS-TRAN-28	Dun	75	4	300	19
T1S1	Harz	1424	76	314	20
T2S3	Harz	1913	102	314	20
T2S8	Harz	1975	106	312	20

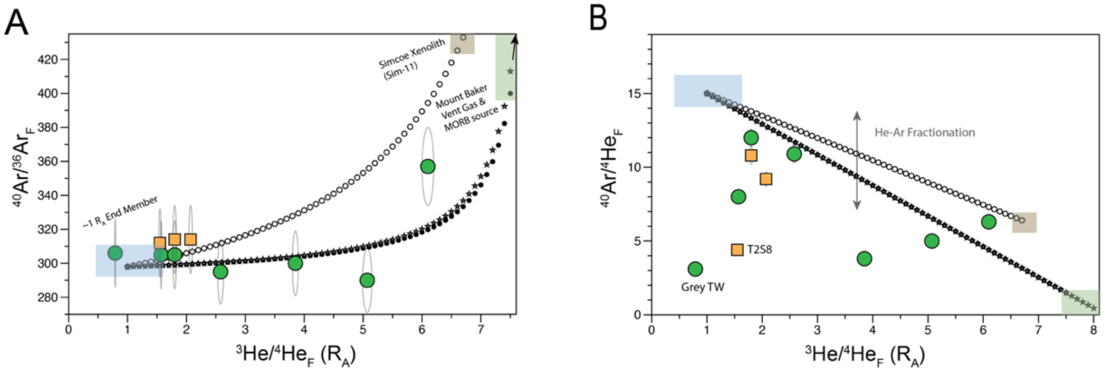

Figure 1.5. He and Ar in Twin Sisters peridotite samples obtained by powder fusion. A) $^{40}Ar/^{36}Ar_F$ against $^{3}He/^{4}He_F$ with a mixing curve; B) $^{40}Ar/^{4}He_F$ against $^{3}He/^{4}He_F$ with a mixing curve. Mixing curves are calculated with three potential high-R_A compositions: one similar to Mount Baker geothermal gases ($^{3}He/^{4}He$=7.5 R_A, $^{40}Ar/^{36}Ar$=400 and $^{40}Ar/^{4}He$=1.5; Symonds et al., 2003); a second with values measured in a peridotite xenolith (Sim-11) from Simcoe, Washington associated with the Cascades Arc ($^{3}He/^{4}He$=6.7 R_A, $^{40}Ar/^{36}Ar$=433 and $^{40}Ar/^{4}He$=6.4; Dodson and Brandon, 1998); and a third similar to MORB mantle ($^{3}He/^{4}He$=8 R_A, $^{40}Ar/^{36}Ar$=40,000 and $^{40}Ar/^{4}He$=0.45; Burnard *et al.*, 1997). The 1±0.5 R_A mixing endmember is a mixture of air-saturated groundwater with radiogenic ^{4}He and a component of mantle noble gases ($^{3}He/^{4}He$=1 R_A, $^{40}Ar/^{36}Ar$=298 and $^{40}Ar/^{4}He$=15). The absence of linearity in Panel B suggests He/Ar fractionation.

1.5.6 Uranium and Thorium concentrations

U concentrations range from 0.15 to 0.71 ppb and Th concentrations from 0.6 to 1.6 ppb (Table 1.3). There is no obvious distinction among concentrations in the dunites, harzburgites, and the clinopyroxene vein.

Table 1.3. U and Th concentrations of whole rock samples, a clinopyroxene vein mineral separate (CPX_v) and USGS standard DTS-2b. Reported U and Th concentrations of DTS-2b are 1.7-2.4 ppb U and 2.87-4.12 ppb Th (Debret *et al.*, 2019; Robin-Popieul *et al.*, 2012; Rospabé *et al.*, 2018a, 2018b; Zhang *et al.*, 2019).

Sample	Replicates	U ppb	$\pm\sigma_M$	Th ppb	$\pm\sigma_M$
20-TS-14	2	0.18	0.01	0.9	0.2
20-TS-16 (CPX_v)	2	0.71	0.05	1.3	0.3
20-TS-18	2	0.15	0.01	0.8	0.2
T1S7	2	0.64	0.05	1.6	0.3
T1S8	2	0.23	0.02	0.8	0.2
TS-TRAN-00	3	0.32	0.01	0.6	0.1
DTS-2b	3	1.9	0.1	2.9	0.5

1.6 Discussion

Dunites and harzburgites from the TSC have total He concentrations spanning a factor of almost 200, and $^3He/^4He$ ratios ranging from slightly below atmospheric to ~6 R_A. Variability is observed among samples over cm length scales (Figure 1.S2), and even individual samples contain isotopically distinct He components that can be resolved through step heating (Figure 1.5). These observations are inconsistent with expectations of a residual mantle in which melt extraction has almost entirely removed He, and in which high temperatures promote diffusional homogenization of He across much longer length scales (Albarède, 2008; Cherniak and Watson, 2012; Hart, 1984). The main questions to be addressed here are the origin of these He components, how, when, and where they were introduced, and how they are sited and preserved in peridotites of the TSC.

1.6.1 He components

He isotope variability in our samples requires the presence of at least two isotopically distinct components which we refer to as "high R_A" and "~1 R_A" (Figure 1.3). The fact that step heating at least partially resolves them implies they were added in two separate processes rather than mixed first and then added. The presence of cosmogenic ^{3}He in some samples is indicated by the very high ^{3}He/^{4}He ratios occasionally observed by Francis (2019) in fused samples, and in our step-heat analysis of sample T1S8 from that study (Figure 1.4). However, the new samples described here were collected immediately downslope from a retreating glacier, where cosmic ray exposure should be minimal. Supporting this conclusion, a substantial cosmogenic ^{3}He component in the new samples can be ruled out because the highest ^{3}He/^{4}He ratios (above 5 R_A) are observed in both crush and fusion analyses (e.g., 20-TS-18, TS-TRAN-34) and cosmogenic He is not liberated by crushing of olivine or pyroxene (Blard et al., 2008; as well as our sample T1S8). Furthermore, the highest He isotope ratios measured by step heating in the newly collected samples are liberated at high temperatures (>1100 °C, Figure 1.4), but in sample T1S8 the cosmogenic component is clearly extracted below 1000 °C.

The highest ^{3}He/^{4}He ratios of around 6 R_A suggest the high R_A component originates in the mantle. This maximum ratio is slightly lower than the MORB mantle (8 ± 1 R_A: Allègre *et al.*, 1995) and nearby Cascade arc volcanoes (e.g., vent gases from Mount Baker 7.5 ± 0.1

R_A: Symonds *et al.*, 2003; springs near Three Sisters volcanoes ≥ $7R_A$: Evans *et al.*, 2004), but is similar to values measured in xenoliths from the sub-continental lithospheric mantle (e.g., 6.1 ± 0.9 R_A: Gautheron and Moreira, 2002) and is within the range of mantle xenoliths erupted from the Simcoe shield volcano of the Cascades arc (4.2-8.2 R_A; Dodson and Brandon, 1999).

The lowest $^3He/^4He$ ratios in the Twin Sisters suite cluster around 1 ± 0.5 R_A (Figures 1.2B, 3). For example, the lowest $^3He/^4He_T$ obtained on peridotite is 0.94 R_A and ratios as low as 0.35 R_A were obtained in some steps of the step heat experiments (Figure 1.4). $^3He/^4He$ ratios near 1 R_A are clearly distinct from purely radiogenic He (estimated to have a $^3He/^4He$ ratio of <0.01 R_A in an ultramafic lithology: Andrews, 1985), and therefore implicate either a He component sourced from the atmosphere (currently 1 R_A by definition), or a mixture of radiogenic He with mantle He that fortuitously yields an air-like $^3He/^4He$ ratio. As with a cosmogenic component, an in-situ radiogenic component accumulated in the crystal matrix after cooling below the He closure temperature is expected to be released by fusion but not by crushing. This expectation is inconsistent with the strong correlation between $^3He/^4He$ ratios released by crushing and by fusion of our samples (Figure 1.2B). This observation argues strongly against in-situ radiogenic He being an important source of the ~ 1 R_A component. The seeming absence of in-situ radiogenic He and its possible implications are discussed in Section 1.6.6.

He isotope-concentration systematics (Figure 1.3) can be interpreted to indicate that the peridotite initially carried only the high R_A component in fairly low concentrations (< ~20 ncc/g), but during exhumation variable and in some cases very large amounts of the ~1 R_A component were added (up to ~10^3 ncc/g as seen in some of the samples analyzed by Francis, 2019). The dunites plot at generally higher $^3He/^4He$ ratios for a given He concentration relative to the harzburgites, such that the two define barely overlapping regions of the mixing diagram (Figure 1.3). The apparent distinction between the harzburgites and dunites could indicate that the harzburgites had lower concentrations of the high R_A component than the dunites, or alternatively that the high R_A component in the dunites (~5.5-6 R_A) is higher than that in the harzburgites (~3.5 R_A). Spatial variations in $^3He/^4He$ indicate that the relative proportion of the high R_A and ~1 R_A components varies over just a few cm (Figure 1.S2 in Appendix 1.A).

1.6.2 He and Ar siting

Previous studies of basalt-hosted olivine and pyroxene crystals have effectively isolated fluid-inclusion-hosted helium from matrix-associated helium by first crushing the samples to release the fluid inclusion component, followed by powder fusion to isolate the matrix component (Blard *et al.*, 2008; Kurz *et al.*, 1990). This technique is effective because crushing to powder prior to fusion opens a substantial fraction of the fluid inclusions — the inclusions are generally large compared to the grain size of the powder. In contrast, in the Twin Sisters samples, on average only about one third of the total helium of each isotope is released by crushing (Figure 1.S1). Recanati *et al.* (2012) similarly observed that a substantial helium fraction was retained after crushing of samples from the Josephine ophiolite. Because crush extraction is only known to liberate helium from fluid inclusions, our results suggest that helium in Twin Sisters samples is present in fluid inclusions. However, unlike in basalt-hosted olivine and pyroxene crystals, the fluid inclusions are sufficiently small that some of them (accounting for about two thirds of the total helium) escape rupture by grain-size reduction to <~30 μm prior to powder fusion analysis. If we model this powder as consisting of cubes with 30 μm edges, then about one third of a population of 4 μm diameter spherical inclusions will be intersected and therefore ruptured during crushing. Fluid inclusions of this size are consistent with our thin section observations (see below). An important implication of the strong correlation between $^3He/^4He_C$ and $^3He/^4He_F$ (Figure 1.2B) is that both helium components are present in fluid inclusions of similar size — if not, there would be a more substantial isotopic distinction between crush and fusion $^3He/^4He$ ratios. The modest preference for higher $^3He/^4He$ ratios in the fusion may indicate that the high R_A component is hosted in, on average, smaller inclusions than the ~ 1 R_A component.

Compared to crushing and powder fusion, step heating was much more effective in separating the two isotopic components, with the ~ 1 R_A component released preferentially below ~1000°C and the high R_A component at higher temperatures. He release during step heating may be controlled by thermal decrepitation of inclusions as the internal pressure of the inclusions exceeds the confining strength of the host mineral (Lamadrid *et al.*, 2021; Wanamaker *et al.*, 1990). For example, Bodnar *et al.* (1989) showed that large-volume synthetic fluid inclusions in quartz decrepitated at lower temperatures than small-volume inclusions at constant inclusion pressure and composition. Higher temperature decrepitation might similarly be expected for lower pressure inclusions at fixed inclusion volume and composition. The possibility of preferential siting of the high R_A component in smaller inclusions is consistent with the higher average $^3He/^4He$ ratio obtained by fusion compared to crushing (Figure 1.2B).

Alternatively, helium release during step heating might be controlled by thermally activated He mobility associated with dissolution of He from inclusions into matrix, followed by diffusive migration out of the grain. However, since the matrix in which He must dissolve and diffuse is the same for both the high R_A and the ~1 R_A components, it is unclear why this process would produce the observed step heating profiles.

Further insights to siting and origin of the components comes from petrography that reveals the presence of fluid inclusions, fractures, and serpentine minerals. All studied Twin Sisters peridotites host planar inclusion trails with individual inclusions ranging from ~15-30 microns to as small as ~100 nm (Figure 1.6E). Inclusions are often elongated, with long-axes aligned within a given trail. Trails occur in multiple orientations, frequently cross-cutting each other. Among the four samples observed under SEM (T2S3, TS05-GL, SLQ07 and SLD01), all contain linearly oriented arrays of sub-micron voids. These features are consistent with fluid inclusions decorating annealed fractures and are similar to those reported in the Zambales ophiolite (Grozeva *et al.*, 2020) and in many other peridotites (Klein *et al.*, 2019).

Among our samples in close spatial proximity, we sometimes observed higher He concentrations and lower $^3He/^4He$ ratios in the samples with more inclusion trails (Figure 1.6A-B). However, we did not find a convincing general correlation between the abundance of inclusion trails and He concentration or isotope ratio throughout the sample suite.

In addition to fluid inclusion trails, some of the peridotites are extensively fractured and serpentinized. Serpentine minerals (lizardite and minor antigorite identified by Raman spectroscopy) fill some of the fractures and grain boundaries. In the most extreme cases, serpentine minerals pervasively replace olivine grains (Figure 1.S4E), whereas in other cases they are restricted to thin veins. Other samples appear to be entirely free of serpentinization (Figure 1.S4A-C).

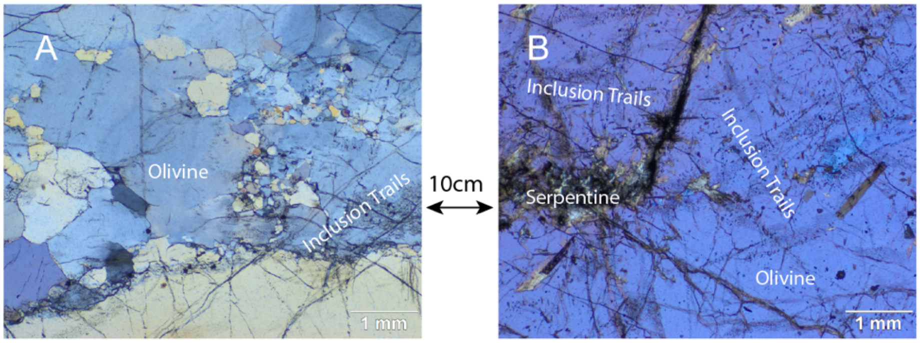

20-TS-08 (3.6 R_A, 18 ncc He/g)

20-TS-09 (2.7 R_A, 70 ncc He/g)

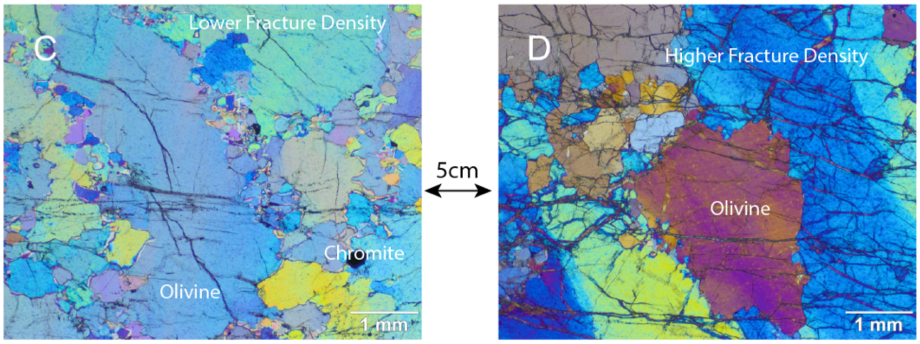

20-TS-03 (2.6 R_A, 26 ncc He/g)

20-TS-04 (1.8 R_A, 75 ncc He/g)

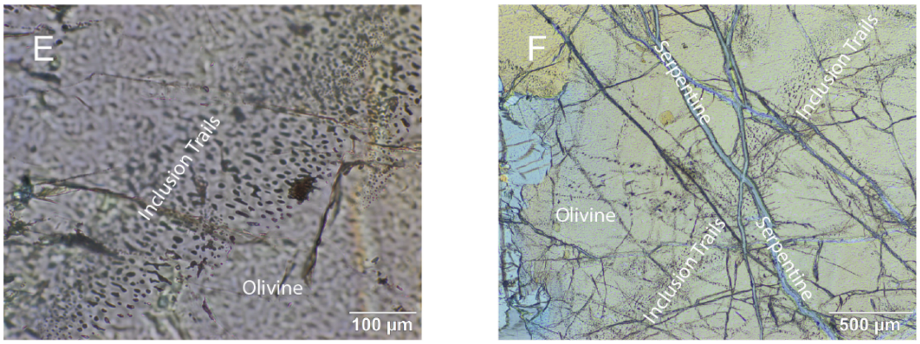

20-TS-08

T1S1

Figure 1.6. Photomicrographs (cross polarized light) of representative thin sections. In A-B and C-D the arrow indicates the physical separation between the samples when collected in the field. Total ^{3}He/^{4}He ratios and He concentrations (labelled) suggest that higher fracture density and/or serpentinization is associated with higher He concentrations and lower ^{3}He/^{4}He ratios. E) An example of ~30-micron sized fluid inclusions very common in our samples and F) of serpentine veins, which are much less common.

Peridotites with low fracture density and rare or no serpentine veins (Figure 1.S4A-C) have lower He concentrations and higher $^3He/^4He$ ratios than those with higher fracture density and serpentine vein abundance (Figure 1.S4D-F). Samples with the highest He concentrations and lowest $^3He/^4He$ ratios, e.g., sample T2S8 with 547 ncc/g of ^4He_T and a $^3He/^4He_T$ ratio of 1.5 R_A, have a distinctly darker tone in hand sample. Thin section petrography indicates the dark color is associated with abundant fracturing and serpentinization (Figure 1.S4E). These observations link the ~1 R_A component to serpentinization.

Notable variations in He systematics along the sampling transects may similarly be related to serpentinization. Dunite sample 20-TS-09 consists of ~1 cm diameter olivine grains that contain a high density of inclusion trails and serpentine minerals filling fractures while sample 20-TS-08, located 10 cm away, contains smaller grains and exhibits a lower density of inclusion trails and almost no serpentine minerals (Figures 1.6A-B, 1.S2 and Table 1.S2). The He concentration of 20-TS-09 is four times higher and the $^3He/^4He$ ratio 25% lower than in 20-TS-08, which is consistent with the ~1R_A component being associated with serpentinization (Table 1.S2 and Figure 1.S2). Likewise, while samples 20-TS-03 and 20-TS-04 were collected ~5 cm apart, the He concentration in sample 20-TS-04 is ~3 times higher and the $^3He/^4He$ ratio 30% lower than those of 20-TS-03 (Table 1.S2 and Figure 1.S2). Thin sections reveal that sample 20-TS-04 has a higher density of thin fractures filled with serpentine minerals compared to 20-TS-03 (Figure 1.6C-D).

The linkage between the ~ 1 R_A component and serpentine minerals is supported by the analysis of two samples dominated by such minerals. 20-TS-01, a vein that is 100% serpentine minerals, yielded a $^3He/^4He$ ratio of 0.94 R_A; 20-TS-15, a breccia consisting of roughly equal proportions of serpentine minerals and olivine+pyroxene, yielded a ^{3}He/^{4}He ratio of 1.2 R_A. However, despite their low ^{3}He/^{4}He ratios, these samples hosted low (20-TS-01) to average (20-TS-15) He concentrations. Thus, while peridotites with higher He concentrations and lower ^{3}He/^{4}He ratios often have more serpentine minerals, the serpentine minerals themselves may not host the ~ 1 R_A component. Most obviously, if the He concentrations we measured in the serpentinites are typical, they are not sufficiently He-rich to account for the high concentrations of ~1 R_A He observed in some of the peridotites. A low abundance of He in serpentines is consistent with He closure temperatures of <100ºC estimated for these minerals by first principles calculations (Wang *et al.*, 2020). Serpentinization occurs along fractures that act as conduits for fluid transport; annealing of these fractures and trapping of serpentinizing fluids in inclusions in olivine or pyroxene is the most plausible explanation for the association of the ~1 R_A component with serpentine.

A final linkage of the ~1 R_A component to serpentinization comes from Raman spectroscopy of inclusions in olivine grains from a few selected samples (Figure 1.S5). Spectra of olivine hosted inclusions in sample 20-TS-02D, with a ^{3}He/^{4}He$_F$ ratio of 1.6 R_A, tend to show both a sharp peak in at ~2914 cm^{-1} Raman shift and peaks in the $3650 - 3700\ \mathrm{cm}^{-1}$ wavenumber range, consistent with the presence of methane vapor, lizardite and brucite inclusions. These peaks are largely absent or much less distinct in two high-R_A samples (20-TS-10 and 20-TS-18) indicating a preference for methane and hydrous mineral inclusions in the low-R_A samples, probably from entrapment of aqueous fluids and subsequent serpentinization within the inclusions (Klein *et al.*, 2019).

1.6.3 Origin of the ~ 1 R_A component

In this section and the next we focus on possible origins of the two endmember compositions we infer have interacted to create the He-Ar systematics in Twin Sisters peridotites. In the section that follows we describe how these components may have mixed, and how mixing accounts for the observed composition in the Twin Sisters rocks (e.g., in He-Ar space, Figure 1.5).

Serpentinization is implicated in the introduction of the ~1 R_A component to the Twin Sisters peridotites, but the origin of its $^3He/^4He$ ratio (1±0.5 R_A) is unclear. As noted above, the similarity of this ratio to the composition of air He suggests an atmospheric source. Addition of atmospheric gases to the samples such as by trapping of air-saturated groundwater during serpentinization can be ruled out for two reasons. First, air-saturated groundwater carries just ~50 ncc He/g (Kipfer *et al.*, 2002), far too little to account for observed peridotite helium concentrations of 100 to 1000 ncc/g (Table 1.1; Francis, 2019). Second, although the $^{40}Ar/^{36}Ar$ ratio of the ~ 1 R_A component is air-like (Figure 1.5A), the $^{40}Ar/^4He$ ratio is definitely not: Twin Sisters peridotites range in $^{40}Ar/^4He$ from about 3-12 (Figure 1.5B), but $^{40}Ar/^4He$ ratios of air (1800: Porcelli and Ballentine, 2002) and air-saturated water (~8000: Kipfer *et al.*, 2002) are orders of magnitude higher. Barring implausibly extreme He/Ar fractionation, only a tiny fraction of the He in Twin Sisters peridotites can be air-derived. The same is not true for Ar. For example, the Ar concentrations we measured (10^2-10^3 ncc STP/g) could be explained by reasonably small additions of air-saturated groundwater with Ar concentration of ~$4x10^5$ ncc STP/g (Kipfer *et al.,* 2002).

Despite its suggestive isotopic similarity to atmospheric He, we conclude that the ~1 R_A component in our samples is more likely a mixture of mantle, crustal, and atmospheric sources that fortuitously yield a near air-like $^{3}He/^{4}He$ ratio. Near the surface, groundwaters equilibrate noble gases with the atmosphere, but in the subsurface they accumulate radiogenic ^{4}He and ^{40}Ar. The average crustal $^{40}Ar/^{4}He$ production ratio from K, U, and Th decay is ~0.2 (Torgersen *et al*., 1989), and one might therefore expect a fluid with crustal radiogenic helium to be characterized by high $^{40}Ar/^{36}Ar$ ratios (which are not seen in TSC samples). However, diffusion, alpha particle ejection, and radiation damage can strongly enhance release of ^{4}He over ^{40}Ar from host minerals into subsurface fluids. For example, natural gases and groundwaters often contain abundant radiogenic He but Ar concentrations and $^{40}Ar/^{36}Ar$ ratios indistinguishable from air saturated water (Andrews *et al*., 1989; Torgersen *et al.,* 1989). The result of this ^{4}He-^{40}Ar fractionation can be a crustal fluid with very low $^{3}He/^{4}He$ ratios (~0.02 R_A), air-like $^{40}Ar/^{36}Ar$, and $^{40}Ar/^{4}He$ ratios orders of magnitude lower than air saturated water (e.g, ≤ 20).

Once in solubility equilibrium with the atmosphere, a groundwater to which crustal radiogenic He has been added cannot account for our ~1 R_A component - the $^{3}He/^{4}He$ ratio would be far too low. Instead, we hypothesize that addition of mantle noble gases raised the $^{3}He/^{4}He$ ratio of the deeply circulating water without strongly modifying Ar systematics. As a plausibility argument, consider a mixture of air saturated groundwater enriched with radiogenic He as described above (with $^{40}Ar/^{4}He$ arbitrarily chosen to be 15) and geothermal gases on the nearby Mt Baker arc stratovolcano: $^{40}Ar/^{36}Ar \sim 400$, $^{40}Ar/^{4}He \sim 1.5$, and $^{3}He/^{4}He \sim 7.5$ R_A (Symonds *et al*., 2003). When these endmembers are mixed in proportions to yield a fluid with a $^{3}He/^{4}He$ ratio of 1±0.5 R_A, the $^{40}Ar/^{36}Ar$ ratios would be between 297 and 299 and $^{40}Ar/^{4}He$ between 6.5 and 7.5. These modeled ratios are in good agreement with those measured in our most He-rich, low $^{3}He/^{4}He$ samples (Figure 1.5) supporting the conclusion that this fluid is an appropriate endmember.

1.6.4 Origin of the high R_A component

The high R_A component in the Twin Sisters samples is clearly of mantle derivation. Although most samples are heavily overprinted by the ~ 1 R_A component, the high R_A component is nevertheless present in all samples we investigated. The ubiquitous presence of a mantle component in the Twin Sisters samples is consistent with previous studies of peridotite massifs (Grozeva *et al.*, 2020; Recanati *et al.*, 2012).

A mantle component could have been trapped any time between last melt extraction (which is expected to have stripped He away) and last communication with mantle during exhumation. Formation of secondary inclusions may have trapped mantle-sourced fluids at relatively shallow depths during exhumation, in much the same way the serpentinization-associated ~ 1 R_A component was trapped. For example, the Twin Sisters rocks may have experienced injection and trapping of magmatic gases released in association with Cascade Arc volcanism (e.g., Mt Baker). However, unlike the ~ 1 R_A component, the high R_A component would have to have escaped addition of substantial externally sourced radiogenic helium.

As a more likely alternative, fluid inclusions trapping the high R_A component may have formed by processes occurring in the lithospheric mantle, i.e., at higher temperatures than the process described above. Supporting this interpretation is the He isotope distinction between the dunites and the harzburgites. The dunites occur as tabular bodies that crosscut the harzburgite and have been interpreted as the product of channelized melt-rock interaction under mantle conditions (Kelemen *et al.*, 1995, 1997, 2000; Kruckenberg *et al.*, 2013). Compared to the harzburgites, these dunites have higher $^3He/^4He$ ratios for a given He concentration (Figure 1.3) suggesting the dunites may have trapped a mantle component with a higher $^3He/^4He$ ratio than the harzburgites. The distinction between harzburgites and dunites seems unlikely if the mantle component was simply injected by fractures pervasively penetrating through the peridotite body during exhumation. Instead, this observation suggests that the melt percolating through the peridotite to form the dunite bands was associated with a higher $^3He/^4He$ ratio than the harzburgites. This interpretation would indicate a relatively ancient He source, i.e., one associated with the process of dunite band formation in the mantle prior to exhumation of the massif. An important implication of this explanation is that melt-rock interaction does not completely strip He from olivine despite its extreme incompatibility (Heber *et al.,* 2007; Jackson *et al*., 2013; Parman *et al.*, 2005); instead, He can remain trapped in fluid inclusions, possibly retarding diffusive migration from crystal to melt.

The unambiguous presence of the high R_A component within the peridotite offers another possibility for the source of mantle He in the ~ 1R_A serpentinizing fluid: reworking of He from earlier generations of fluid inclusions opened during serpentinization. A similar possibility was noted by Klein *et al.,* (2019), who concluded that release of gases from fluid inclusions during serpentinization is the source of mantle He in serpentinization-related fluid seeps. In the case of the Twin Sisters, groundwater with initially radiogenic helium and atmospheric argon as described above could penetrate the peridotite as it exhumes and serpentinizes, reworking mantle He from the peridotite and raising the fluid's $^3He/^4He$ ratio from ~0.02 R_A to ~1 R_A. Associated fracture annealing could trap this isotopically modified composition in later-formed inclusions. In support of such a model we note that the two samples with the lowest $^3He/^4He$ ratios (Grey TW, SLQ10, both with $^3He/^4He$ ratios ≤ 1 R_A) are from the Sven Larsen quarry, at the contact between the peridotite and the surrounding country rock where one might expect a greater integrated degree of interaction of groundwater with the peridotite. A model in which the ~ 1 R_A component evolves isotopically by reworking of He from inclusions in the peridotite is also consistent with the observation that the ~1 R_A component released by step-heating spans an isotopic range, from ~0.4 to ~1.5 R_A.

1.6.5 A Proposed Model

Figure 1.7 provides a diagrammatic model in which the processes affecting the peridotite noble gas budget are laid out in temporal sequence. The model begins with a harzburgitic sub-continental lithospheric mantle with a low concentration of He with a $^3He/^4He$ ratio of about 3.5 R_A trapped in fluid inclusions, presumably derived from some earlier metasomatic or melting event for which we have no other evidence (Stage 1). Similar $^3He/^4He$ ratios were observed in peridotite xenoliths from Simcoe volcano further south in the Cacscade arc in support of this possibility (Dodson and Brandon, 1999).

In Stage 2, dunite bands formed as arc magmas antecedent to the ~35-45 Ma initiation of the Cascades Arc (Humphreys and Grunder, 2022; Kant *et al.*, 2018; Miller *et al.*, 2022) percolated through the harzburgite host rock at ~15-25 km depths, resulting in capture of ~6 R_A fluids typical of arc volcanism (Hilton *et al.*, 2002). This model suggests that melts associated with dunite channel formation carry a free fluid phase which becomes trapped in neoformed olivine. Furthermore, this process occurs without significant He exchange with the surrounding harzburgites.

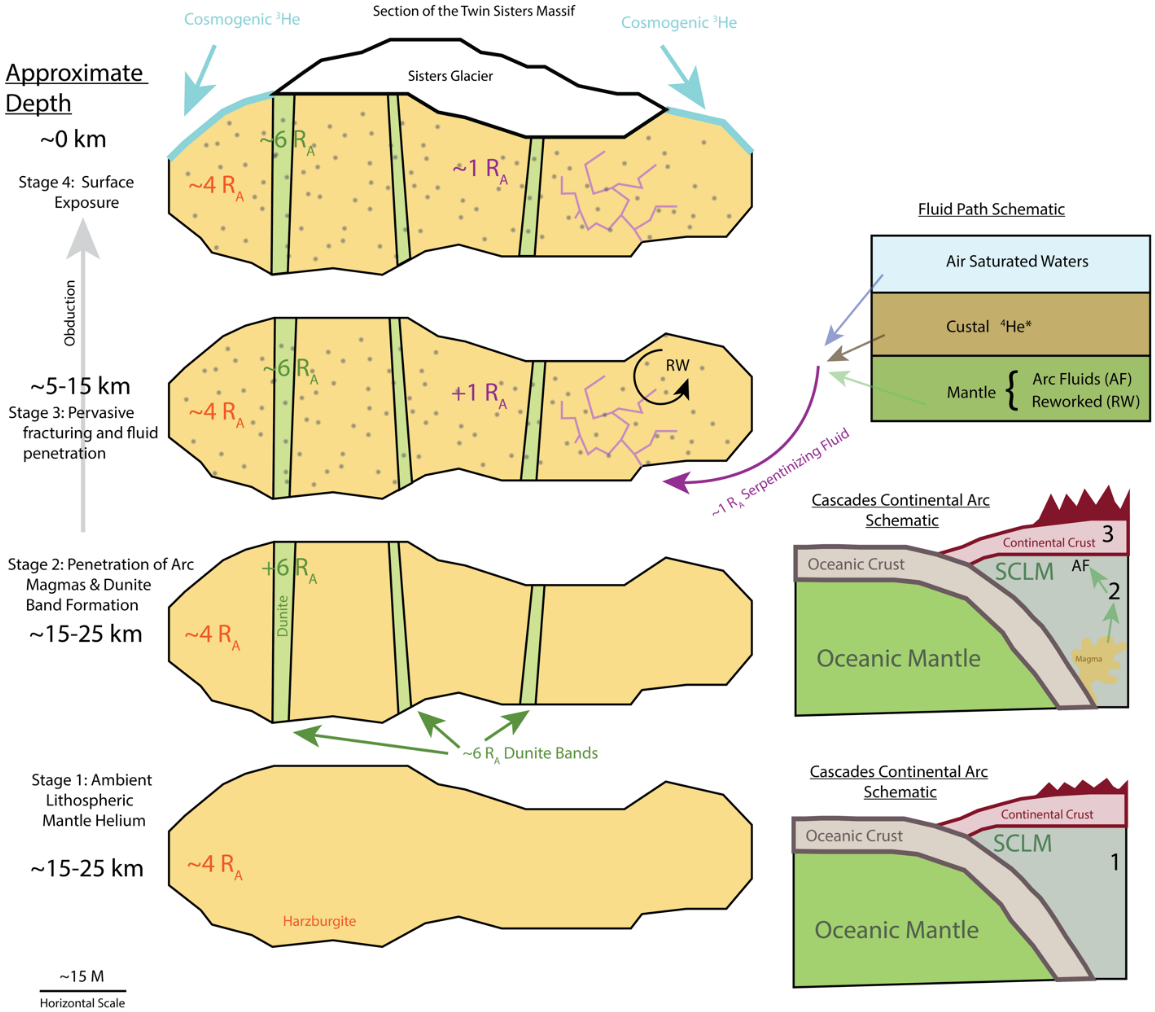

Figure 1.7. Schematic of hypothesized He-Ar systematics of the Twin Sisters peridotite massif from ~15-25 km depth to the surface of the Earth. Stage 1 consists of the initial entrapment of ambient mantle He in mantle harzburgite. Stage 2 involves the subsequent formation of dunite bands as arc-related magmas penetrate the harzburgite beneath the Cascades Arc or its predecessor. Stage 3 follows the initiation of obduction in which a ~1 R_A serpentinizing fluid derived from air saturated groundwater, crustal radiogenic ^{4}He and reworked and/or arc-derived mantle helium is entrapped by the annealing of fractures (purple lines indicate fracture, stipel indicates fluid penetration). Stage 4 involves the exhumation and modern conditions of the Twin Sisters Massif, which preserves He-Ar signatures associated with Stages 1-3.

Obduction of the peridotite occurs in Stage 3, likely in the late Cretaceous. Groundwaters, saturated with atmospheric He and Ar, acquired high concentrations of radiogenic He with low $^{40}Ar/^{4}He$ ratios owing to the preferential extraction of ^{4}He from crustal rocks. There are then two possibilities for raising the $^{3}He/^{4}He$ ratio of this fluid to ~ 1 R_A. The first possibility is addition of magmatic fluids to the deeply circulating groundwater, the second is by reworking of the mantle helium trapped in Stages 1 and 2 after aqueous alteration begins. Either way, this fluid then serpentinizes the peridotite. The processes of exhumation, serpentinization, fracturing, and annealing led to the pervasive capture of this second fluid in inclusions throughout the peridotite at depths of ~5-15 km (Figure 1.7 – Stage 3). Ongoing obduction of the Twin Sisters massif led to the modern surface exposure of the massif and the termination of fluid-capture via serpentinization and fracture annealing (Stage 4).

Quantitative He-Ar mixing curves for these scenarios are indicated on Figure 1.5. In $^{3}He/^{4}He$ - $^{40}Ar/^{36}Ar$ space, a mixing array between the ~ 1R_A serpentinizing fluid endmember in section 5.3 and reasonable high R_A mantle endmembers (Mount Baker geothermal gases, MORB mantle, and Simcoe xenoliths) adequately bound the data. However, in $^{40}Ar/^{4}He$ vs $^{3}He/^{4}He$ space mixing arrays would be linear in the absence of He-Ar fractionation. While broadly consistent with the $^{40}Ar/^{4}He$ ratios predicted by the mixing model, the data do not define a mixing line. This observation suggests significant fractionation of He from Ar in the processes that formed and/or injected the endmembers into the peridotite.

1.6.6 Implications of the absence of in-situ radiogenic He

Our work failed to reveal evidence for in-situ produced radiogenic He ($^{4}He^{*}$), with implications for how recently the Twin Sisters massif exhumed through the He-in-olivine closure temperature. As a firm upper limit on the (U-Th)/He cooling age (Farley, 2002), we assume that only in-situ radiogenic He is released by our powder fusion analyses. This is an upper limit to ^{4}He* because all analyses yield He isotope ratios higher than can be attributed to radioactive decay, likely due to the presence of mantle helium. The lowest powder fusion He concentrations in the current data set were obtained on dunite LL6 and harzburgites T1S7 and T1S8, all between 2.2 and 3.2 ncc/g. We determined U and Th concentrations on samples T1S7 and T1S8 (Table 1.3). Using these data, the lowest upper limit (U-Th)/He cooling age we calculate is 18 ± 5 Ma on sample T1S7. The other samples for which we obtained U and Th concentrations yield a broad range of upper limit cooling ages up to almost a billion years. The ~18 Ma cooling age on T1S7 requires that rocks near the summit of the Twin Sisters massif passed through the He closure isotherm around the early Miocene. This age is far younger than the suspected age of Twin Sisters emplacement (uncertain but probably Cretaceous: Kruckenberg *et al.*, 2013; Onyeagocha, 1978; Whetten *et al.*, 1980) and the first known appearance of Twin Sisters detritus in nearby sedimentary rocks (Brownfield *et al.,* 1995), likely indicating substantial pre-Miocene erosion of the massif.

As noted above, the He closure temperature for olivine of the grain size in our samples is about ~300°C. Regional heat flow data suggest a geothermal gradient at the Twin Sisters of 40°C/km (Blackwell *et al.*, 1990), placing the closure isotherm at ~7.5 km subsurface. Combined with the 18 Ma upper limit on the (U-Th)/He age of T1S7, this depth indicates a mean exhumation rate of greater than 400 m/Myr since 18 Ma. Even with an extreme geothermal gradient (e.g., 70°C/km, perhaps associated with the nearby Mt Baker stratovolcano or its predecessors) the closure isotherm would still be at 4.5 km and the exhumation rate >250 m/Myr. While quite rapid, these exhumation rates are similar to rates observed in broadly granitic rocks of the nearby Cascades (Reiners *et al.,* 2003) and Coast Mountains (Ehlers *et al.,* 2006). Additional analyses undertaken to better isolate ^{4}He* from other sources of ^{4}He could improve upon this limiting exhumation rate.

An additional implication of the relatively high mantle He concentrations coupled with very low U and Th concentrations in peridotites such as we studied in the TSC is that mantle He isotopic signatures may in some cases be preserved for very long periods of time in the lithosphere. For example, sample 20-TS-18 yielded 19 ncc/g of He with a ^{3}He/^{4}He ratio of 5 R_A. Based on our measured U and Th concentrations for this sample, 100 million years of in situ radioactive decay would reduce this ratio by less than 1 R_A. It is very likely that even more ingrowth-resistant (high He/(U+Th)) TSC peridotites exist given how few samples we measured for U and Th. Recanati *et al*., (2012) similarly observed a near absence of ^{4}He* in Josephine ophiolite peridotites. While mantle He in the Twin Sisters peridotites has been compromised by serpentinization, it is possible that other ophiolites may have peridotites that record the He isotopic composition of the ancient oceanic or sub-arc mantle. More speculatively, these observations may indicate that He-rich and radioelement-poor peridotites in the continental lithosphere could preserve near-primary He isotope ratios isolated from the convecting mantle sometime in the distant past.

1.7 Conclusions

Crushing, powder fusion, and step heating analysis of Twin Sisters peridotites reveal the presence of two isotopically distinct He components. One component has a He isotopic ratio of around 6 R_A, similar to mantle values. The highest concentrations of this component are found in dunite bands attributed to reactive melt percolation through the mantle, suggesting this is a deeply sourced and relatively ancient constituent of the peridotite. These bands may have been created during a phase of arc magmatism prior to obduction. Surrounding harzburgites also carry mantle He, but at lower concentration or of a lower ^{3}He/^{4}He ratio. In both lithologies the He concentrations are higher than would be predicted from mineral-melt partition coefficients applied to mantle residual to melt extraction by ~1-3 orders or magnitude, likely because He is hosted in small fluid inclusions. The same is not true of the parent isotopes of ^{4}He (U and Th), both of which are found at extremely low concentrations of around 1 ppb.

The mantle He component escaped diffusive loss during what is likely to have been millions of years as the peridotite transitioned from hot mantle conditions to below the He closure temperature of about 300°C. This observation suggests an additional important role of fluid inclusions: as an agent that impedes He mobility. In mantle with fluid inclusions and other features into which He partitions, such as zones of intense deformation (Recanati *et al*., 2012), simple volume diffusion calculations (eg., Albarède, 2008) may substantially overestimate He mobility. If so, and if the relative abundances of He and its parent isotopes are commonly as high as measured in this study, near primary mantle ^{3}He/^{4}He ratios may be preserved against both diffusive loss and radiogenic ingrowth over hundreds of millions of years in peridotites carried in the lithosphere.

The second He component in the Twin Sisters peridotites is characterized by a ^{3}He/^{4}He ratio of 1±0.5 R_A and atmospheric Ar, and is associated with serpentinization. The similarity between the He isotope ratio of this component and that of the modern atmosphere is fortuitous as indicated by He-Ar systematics. Instead, this He component is itself likely to be a mixture of mantle and radiogenic He added to a groundwater-sourced serpentinizing fluid.

The two He components found in TSC peridotites are both sited in fluid inclusions, but during step heating the serpentine-associated He is released at lower temperatures than the mantle component.

The near absence of post-emplacement in situ radiogenic helium in Twin Sisters peridotites arises in part from very low U and Th concentrations. It also arises from rapid and likely ongoing exhumation of the Twin Sisters range, at a rate comparable to nearby granitic rocks in the Cascades and Coast Mountains.

Although the Twin Sisters peridotites carry mantle He and are largely unaffected by in situ ^{4}He* ingrowth, assessing the composition and distribution of He in the mantle from these rocks is compromised by the pervasive and largely invisible effects of serpentinization.

Appendix 1.A. Supplementary Material

The supplementary material for this article includes four tables (Table 1.S1-1.S4) and five figures (Figure 1.S1-1.S5). Table 1.S1 contains the GPS coordinates and elevation at which each sample was collected along with the rock type and geologic context. Table 1.S2 contains data that describes sampling transects including the distances between samples and the structure or lithology of a given sample. Table 1.S3 contains step heating He extraction data including the temperature of extraction, the ^{3}He/^{4}He ratio and the ^{4}He extracted during each temperature step. Table 1.S4 contains U and Th concentrations for replicate analyses of peridotite samples. Figure 1.S1 includes histograms of ^4He_C, ^4He_F and $^4He_C/^4He_F$. Figure 1.S2 contains photographs of the sampling transects and plots of ^4He_T and total ^{3}He/^{4}He ratios against distance along the transects. Figure 1.S3 contains plots of concentrations of individual Ar isotopes plotted against concentrations of individual He isotopes. Figure 1.S4 displays photomicrographs of peridotite thin sections and the associated ^4He_T and total $^3He/^4He$. Figure 1.S5 displays the Raman spectra of olivine hosted fluid inclusions.

Table 1.S1 GPS coordinates (WGS-84), elevation, and context of samples. Rock types include dunite (Dun), harzburgite (Harz), serpentinite (Serp), orthopyroxene veins (OPX_v), and clinopyroxene veins (CPX_v).

Sample	Rock	Context	Elevation	Latitude	Longitude
			Meters	Degrees	Degrees
20-TS-02 CL	Dun	In Place	1695	48.7131139	-121.98626
20-TS-02 D	Dun	In Place	1695	48.7131139	-121.98626
20-TS-02 CD	Dun	In Place	1695	48.7131139	-121.98626
20-TS-03	Dun	In Place	1703	48.7130556	-121.98611
20-TS-04	Dun	In Place	1703	48.7130556	-121.98611
20-TS-05	Dun	In Place	1703	48.7130556	-121.98611
20-TS-06	Dun	In Place	1703	48.7130556	-121.98611
20-TS-07	Dun	In Place	1703	48.7130556	-121.98611
20-TS-08	Dun	In Place	1703	48.7130556	-121.98611
20-TS-09	Dun	In Place	1703	48.7130556	-121.98611
20-TS-10	Dun	Float	1665	48.713875	-121.98587
20-TS-14	Dun	Float	1626	48.7175	-121.99
20-TS-18	Dun	Float	1625	48.71784	-121.99254
TS-TRAN-00	Harz	Float	1613	48.7178722	-121.99151
TS-TRAN-02	Harz	Float	1613	48.7178722	-121.99151
TS-TRAN-04	Dun	Float	1613	48.7178722	-121.99151
TS-TRAN-08	Dun	Float	1613	48.7178722	-121.99151
TS-TRAN-12	Dun	Float	1613	48.7178722	-121.99151
TS-TRAN-16	Dun	Float	1613	48.7178722	-121.99151
TS-TRAN-20	Dun	Float	1613	48.7178722	-121.99151
TS-TRAN-24	Dun	Float	1613	48.7178722	-121.99151
TS-TRAN-28	Dun	Float	1613	48.7178722	-121.99151
TS-TRAN-32	Dun	Float	1613	48.7178722	-121.99151
TS-TRAN-34	Dun	Float	1613	48.7178722	-121.99151
TS-TRAN-36	Dun	Float	1613	48.7178722	-121.99151
TS-TRAN-42	Dun	Float	1613	48.7178722	-121.99151
20-TS-11	Dun & OPX_v	In Place	1672	48.7137278	-121.98616
20-TS-12	Harz	In Place	1643	48.7166667	-121.99139

Sample	Rock	Context	Elevation	Latitude	Longitude
			Meters	Degrees	Degrees
20-TS-13	Harz	In Place	1643	48.7166667	-121.99139
20-TS-16	Harz & CPX_v	Float	1668	48.715607	-121.9903
20-TS-01	Serp	In Place	1662	48.7158333	-121.98944
20-TS-15	Serp	In Place	1666	48.7148139	-121.98869
T1S6	Dun	In Place	1421	48.7149	-121.972
T2S1	Dun	In Place	1339	48.7159	-121.975
T1S1	Harz	In Place	1546	48.7121	-121.973
T1S7	Harz	In Place	1401	48.7153	-121.972
T1S8	Harz	In Place	1381	48.7158	-121.972
T2S3	Harz	In Place	1376	48.715	-121.975
T2S8	Harz	In Place	1570	48.7118	-121.976
LL2	*Dun*	*In Place*	*1067*	*48.7228*	*-121.975*
LL6	*Dun*	*In Place*	*1055*	*48.7229*	*-121.977*
Gray TW	**Dun**	**Float**	**1628**	**48.7433085**	**-122.00533**
SLD 02	**Dun**	**In Place**	**1628**	**48.7433085**	**-122.00533**
SLQ 10	**Dun**	**In Place**	**1628**	**48.7433085**	**-122.00533**
SLD 01	**Harz**	**In Place**	**1628**	**48.7433085**	**-122.00533**
SLQ 7	**Harz**	**In Place**	**1628**	**48.7433085**	**-122.00533**
TS05-GL	*Dun*	*In Place*	*1691*	*48.7135333*	*-121.98768*

Note: Samples starting with LL, T1, T2, and SLD are from Francis (2019). Samples in bold are from Sven Larsen quarry. Samples in italics are from surface outcrop but more than 500 m from the retreating Sisters glacier.

Table 1.S2. Spatial transects of Twin Sisters peridotite samples. Photos and data are in Figure 1.S3.

Sample	Transect Increment	Lithology/Structure
Transect 1		
20-TS-02 CL	Starting Point	Dunite Band
20-TS-02 D	1 cm	Dunite Band
20-TS-02 CD	1 cm	Dunite Band
Transect 2		
20-TS-03	Starting Point	Dunite Band
20-TS-04	5 cm	Dunite Band
Transect 3		
20-TS-05	Starting Point	Dunite Band
20-TS-06	10 cm	Dunite Band
20-TS-07	10 cm	Dunite Band
20-TS-08	10 cm	Dunite Band
20-TS-09	10 cm	Dunite Band
Transect 4		
20-TS-12	Starting Point	Harzburgite
20-TS-13	15 cm	Harzburgite
Transect 5		
TS-TRAN-00	Starting Point	Harzburgite
TS-TRAN-02	2 cm	Harzburgite
TS-TRAN-04	2 cm	Dunite Band
TS-TRAN-08	4 cm	Dunite Band
TS-TRAN-12	4 cm	Dunite Band
TS-TRAN-16	4 cm	Dunite Band
TS-TRAN-20	4 cm	Dunite Band
TS-TRAN-24	4 cm	Dunite Band
TS-TRAN-28	4 cm	Dunite Band
TS-TRAN-32	4 cm	Dunite Band
TS-TRAN-34	2 cm	Dunite Band
TS-TRAN-36	2 cm	Dunite Band
TS-TRAN-42	6 cm	Dunite Band

Table 1.S3. Step heating helium extraction data of whole rock powder.

Sample	Temperature	^{4}He	±σ	^{3}He/^{4}He	±σ
	(°C)	(ncc-STP/g)		(RA)	
20-TS-15	490	2.51	0.05	0.77	0.03
	613	3.20	0.07	0.91	0.03
	706	3.42	0.07	0.85	0.03
	782	9.8	0.2	1.01	0.03
	845	16.2	0.3	1.16	0.03
	1000	22.0	0.4	1.11	0.03
	1015	17.8	0.4	1.19	0.03
	1035	18.7	0.4	1.22	0.03
	1065	18.4	0.4	1.29	0.03
	1100	16.0	0.3	1.32	0.03
	1130	11.8	0.2	1.41	0.04
	1165	8.0	0.2	1.50	0.04
	1190	4.8	0.1	1.59	0.05
	1215	2.75	0.06	1.69	0.06
	1250	1.48	0.03	1.71	0.07
	1275	0.74	0.02	1.78	0.08
	1300	0.356	0.008	1.9	0.1
	1330	0.160	0.005	1.6	0.2
	1355	0.065	0.003	1.6	0.3
	1385	0.023	0.002	1.9	0.8
Gray TW	490	1.21	0.04	0.56	0.07
	613	2.31	0.06	1.13	0.06
	706	1.10	0.04	0.46	0.08
	782	1.94	0.05	0.35	0.05
	845	2.36	0.06	0.44	0.04
	1000	4.2	0.1	0.73	0.04
	1015	4.4	0.1	0.83	0.04
	1035	5.7	0.1	0.73	0.03
	1065	7.0	0.2	0.73	0.03
	1100	7.7	0.2	0.75	0.03
	1130	7.3	0.2	0.78	0.03
	1165	6.4	0.1	0.85	0.04
	1190	4.7	0.1	0.85	0.04
	1215	3.12	0.08	0.95	0.05
	1250	1.80	0.05	1.08	0.07
	1275	0.87	0.03	1.4	0.1

Sample	Temperature	^{4}He	±σ	^{3}He/^{4}He	±σ
	1300	0.38	0.02	2.0	0.3
	1330	0.16	0.02	1.7	0.5
TS05-GL	490	0.70	0.02	1.7	0.2
	613	1.08	0.03	3.4	0.2
	706	1.00	0.02	1.8	0.1
	782	1.64	0.04	1.8	0.1
	845	2.71	0.06	2.1	0.1
	1000	5.5	0.1	2.46	0.09
	1015	4.8	0.1	2.6	0.1
	1035	5.7	0.1	2.8	0.1
	1065	6.8	0.1	2.74	0.09
	1100	7.4	0.2	2.81	0.09
	1130	7.0	0.1	3.3	0.1
	1165	6.1	0.1	3.4	0.1
	1190	4.7	0.1	3.8	0.1
	1215	3.41	0.07	4.5	0.2
	1250	2.32	0.05	4.2	0.2
	1275	1.27	0.03	4.5	0.2
	1300	0.66	0.02	4.6	0.3
	1330	0.31	0.01	3.7	0.4
	1355	0.14	0.01	4.2	0.6
	1385	0.071	0.005	4	1
T1S8	490	0.269	0.006	65	2
	613	0.263	0.006	165	4
	706	0.160	0.004	105	3
	782	0.217	0.005	39	1
	845	0.292	0.007	14.0	0.5
	1000	0.54	0.01	7.6	0.3
	1015	0.320	0.007	5.9	0.3
	1035	0.255	0.006	6.1	0.3
	1065	0.204	0.005	5.6	0.3
	1100	0.139	0.004	6.0	0.4
	1130	0.089	0.003	3.4	0.5
	1165	0.047	0.002	3.8	0.9
	1190	0.015	0.001	5	2
T2S8	490	4.20	0.09	1.07	0.04
	613	5.1	0.1	1.15	0.04
	706	7.4	0.2	0.96	0.03

Sample	Temperature	^{4}He	±σ	^{3}He/^{4}He	±σ
	782	20.3	0.4	1.05	0.03
	845	30.5	0.6	1.22	0.03
	1000	64	1	1.18	0.03
	1015	58	1	1.32	0.03
	1035	57	1	1.43	0.03
	1065	53	1	1.50	0.04
	1100	42.9	0.9	1.62	0.04
	1130	30.0	0.6	1.68	0.04
	1165	18.7	0.4	1.75	0.05
	1190	10.0	0.2	1.82	0.05
	1215	4.7	0.1	1.83	0.06
	1250	1.94	0.04	1.79	0.07
	1275	0.72	0.02	1.65	0.08
	1300	0.24	0.01	2.2	0.2
	1330	0.07	0.01	1.9	0.4
	1355	0.02	0.01	5	2
T1S1	490	1.31	0.03	1.68	0.09
	613	1.48	0.04	1.64	0.08
	706	2.32	0.05	1.40	0.06
	782	6.1	0.1	1.42	0.05
	845	7.3	0.2	1.37	0.05
	1000	13.4	0.3	1.32	0.04
	1015	11.2	0.2	1.51	0.05
	1035	11.8	0.2	1.65	0.05
	1065	11.8	0.2	1.89	0.06
	1100	10.6	0.2	1.88	0.06
	1130	8.4	0.2	2.01	0.06
	1165	6.0	0.1	2.08	0.07
	1190	3.84	0.08	2.17	0.08
	1215	2.26	0.05	2.08	0.08
	1250	1.16	0.03	2.3	0.1
	1275	0.51	0.02	2.0	0.2
	1300	0.20	0.01	2.1	0.2
	1330	0.06	0.01	1.9	0.5
20-TS-02 D	490	0.8	0.1	1.9	0.5
	613	2.1	0.1	2.5	0.2
	706	1.0	0.1	2.2	0.4
	782	2.2	0.1	1.3	0.2
	845	3.9	0.2	1.3	0.1

Sample	Temperature	^{4}He	±σ	^{3}He/^{4}He	±σ
	1000	7.9	0.2	1.40	0.07
	1015	5.9	0.2	1.40	0.09
	1035	7.3	0.2	1.42	0.08
	1065	9.2	0.3	1.42	0.07
	1100	10.9	0.3	1.48	0.06
	1130	11.3	0.3	1.56	0.06
	1165	10.9	0.3	1.65	0.07
	1190	9.4	0.3	1.75	0.07
	1215	7.4	0.2	1.88	0.09
	1250	5.2	0.2	1.9	0.1
	1275	3.3	0.1	2.2	0.2
	1300	2.0	0.1	2.3	0.2
	1330	1.09	0.10	2.6	0.4
	1355	0.56	0.09	3.0	0.8
	1385	0.26	0.08	3	2

Table 1.S4. U and Th replicate analyses of separate dissolutions (subscripts a, b & c). The (CPX$_v$) indicates that a clinopyroxene vein was analyzed. Reported ±σ of replicates are analytical. Averages and ±σ$_M$ are reported in Table 1.3. A replicate of 20-TS-16 (CPX$_v$), which yielded 2.5±0.2 ppb U and 1.6±0.2 Th (U concentration is >5σ above other replicates), was rejected from this table. A replicate of 20-TS-14, which yielded 0.29±0.03 ppb U and 23±3 ppb Th (Th concentration is >5σ above other replicates), was also rejected from this table. We attribute these fliers to the incorporation contaminant material such as dust derived from the continental crust.

Sample	U ppb	±σ	Th ppb	±σ
20-TS-14$_a$	0.16	0.03	0.5	0.1
20-TS-14$_b$	0.19	0.02	1.2	0.2
20-TS-16 (CPX$_v$)$_a$	0.71	0.05	1.2	0.2
20-TS-16 (CPX$_v$)$_b$	0.71	0.07	1.3	0.3
20-TS-18$_a$	0.16	0.03	0.9	0.2
20-TS-18$_b$	0.13	0.03	0.30	0.07
T1S7$_a$	0.66	0.07	1.3	0.1
T1S7$_b$	0.61	0.05	1.9	0.6
T1S8$_a$	0.17	0.03	0.6	0.1
T1S8$_b$	0.28	0.04	1.0	0.1
TS-TRAN-00$_a$	0.34	0.03	0.5	0.1
TS-TRAN-00$_b$	0.31	0.04	0.45	0.09
TS-TRAN-00$_c$	0.31	0.03	0.8	0.2
DTS-2b$_a$	1.9	0.1	2.3	0.3
DTS-2b$_b$	2.0	0.1	3.7	0.6
DTS-2b$_c$	1.9	0.1	2.7	0.3

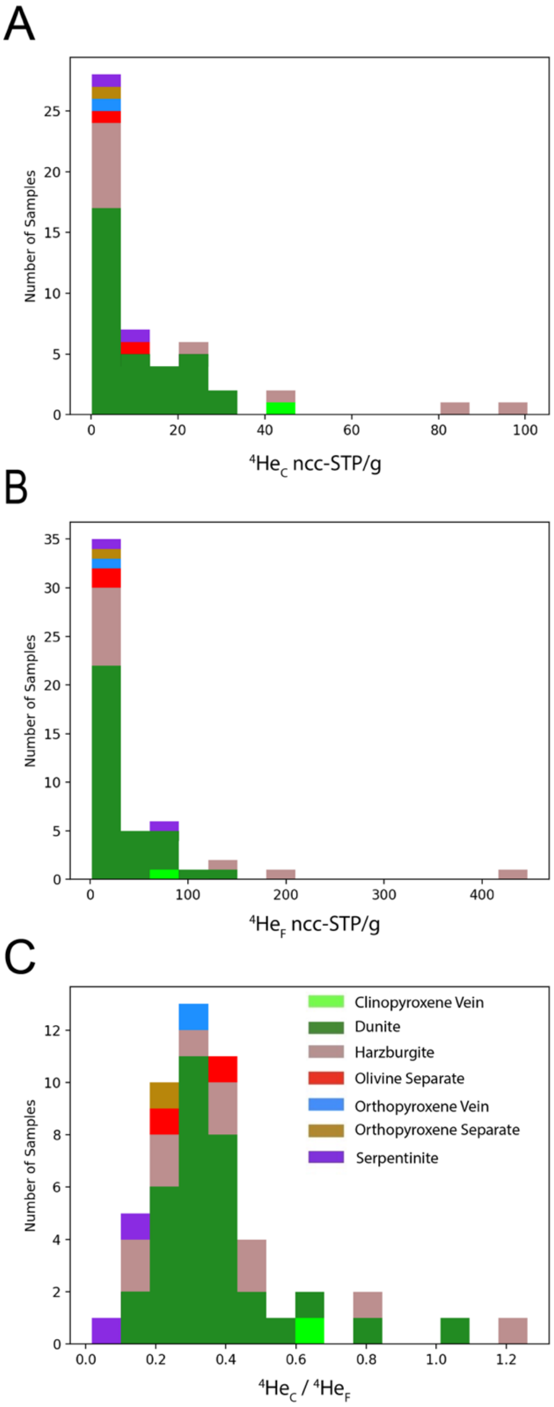

Figure 1.S1. He concentration systematics in Twin Sisters peridotites extracted by A) crushing (^4He_C), B) powder fusion (^4He_F), and C) the ratio of concentrations extracted by each method (^4He_C/^4He_F).

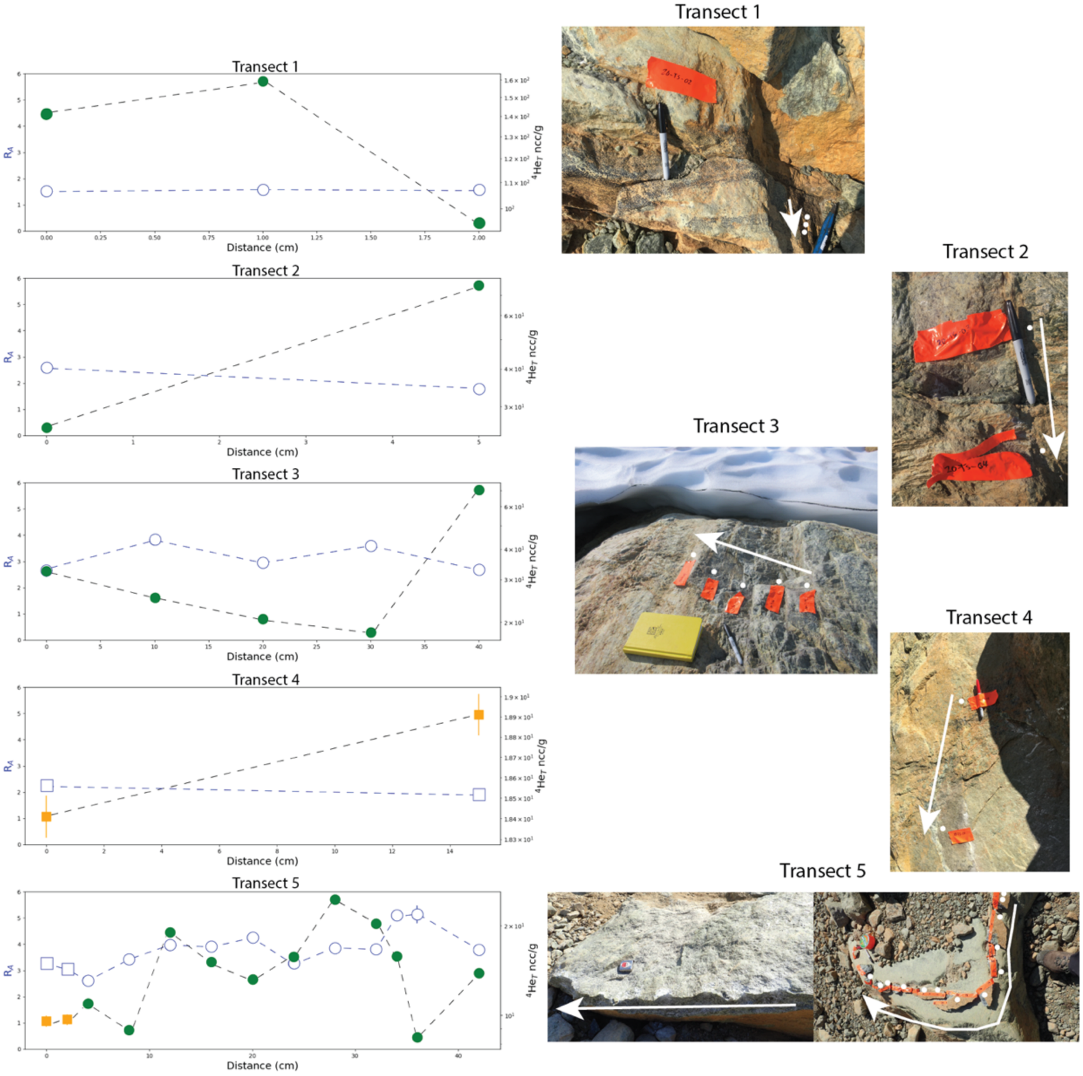

Figure 1.S2. Field photographs and total He concentration and $^3He/^4He$ ratio plotted along spatial transects described in Table 1.S2. In the scatter plots, circles represent harzburgites and squares represent dunites. Open blue symbols represent the isotope ratios and filled symbols (green for dunites and orange for harzburgites) represent He concentrations. In the photographs, white arrows indicate the transect orientation and the white dots indicate the locations in which samples were collected from the rock. Transect 1 crosses a chromite rich band, Transects 2 and 3 are completely within a dunite band, Transect 4 is completely within harzburgite, and Transect 5 spans the entire width of a dunite band and includes harzburgite country rock on one side.

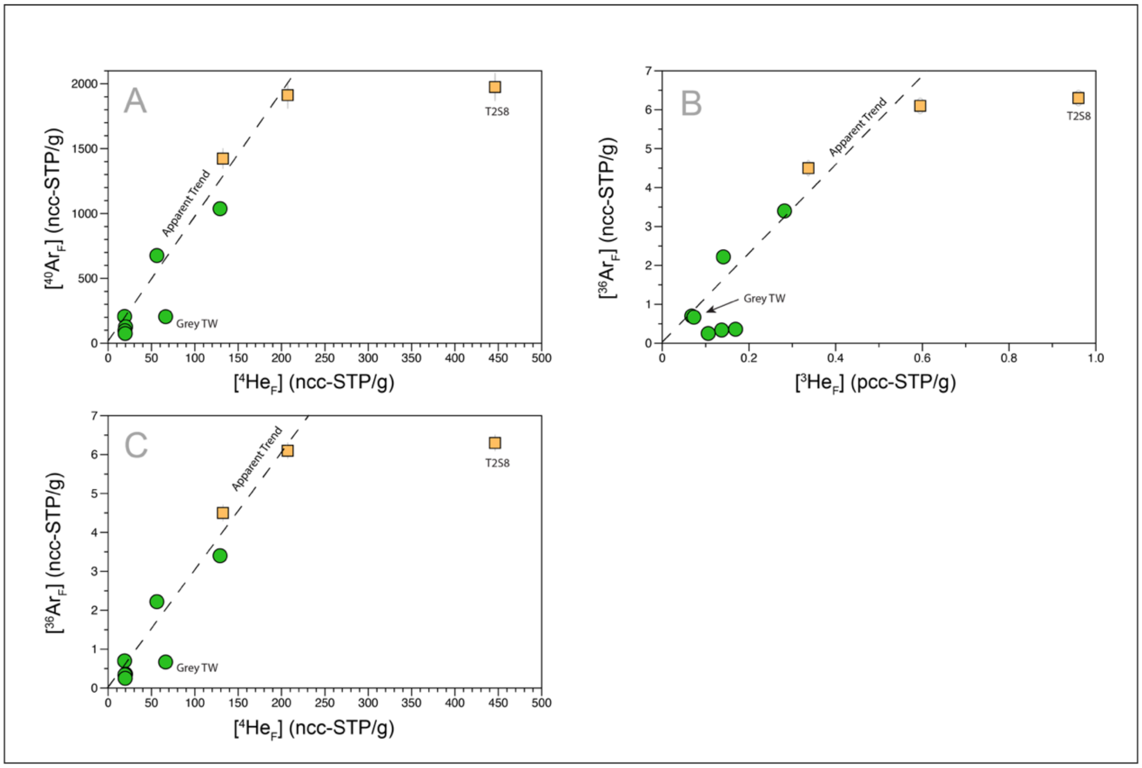

Figure 1.S3. He and Ar in Twin Sisters peridotite samples obtained by powder fusion. Panels A), B) & C) reveal strong correlations between all He and Ar isotopes. Green circles and orange squares represent dunite and harzburgite samples respectively. Apparent trends indicated with black dashed lines through the origin suggest co-siting of He and Ar in the samples. T2S8 has anomalously high ^{3}He and ^{4}He for its Ar content and Gray TW has anomalously high ^{4}He for its Ar content.

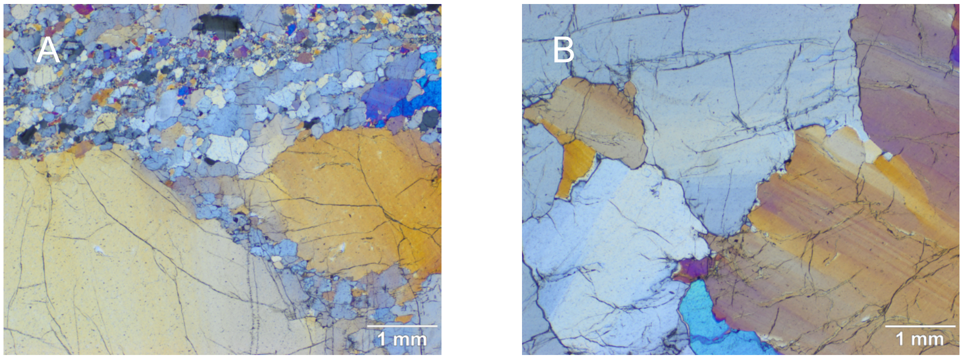

20TS18 (5.3 RA, 27 ncc He/g) TS-TRAN-34 (5.1 RA, 16 ncc He/g)

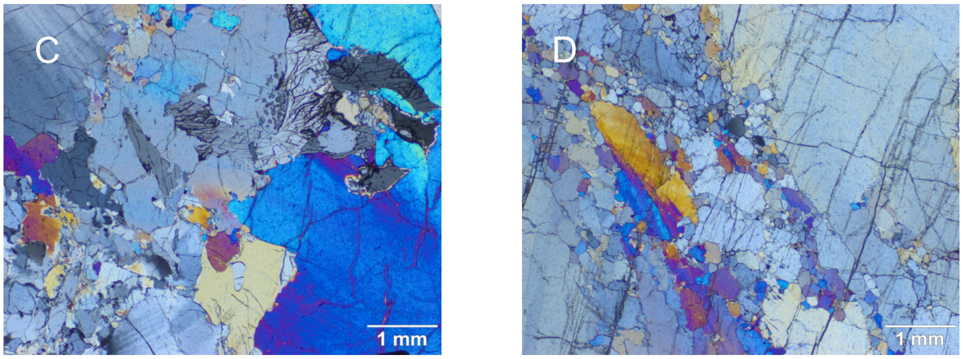

TS-TRAN-02 (3 RA, 10 ncc He/g) 20TS02-D (1.6 RA, 159 ncc He/g)

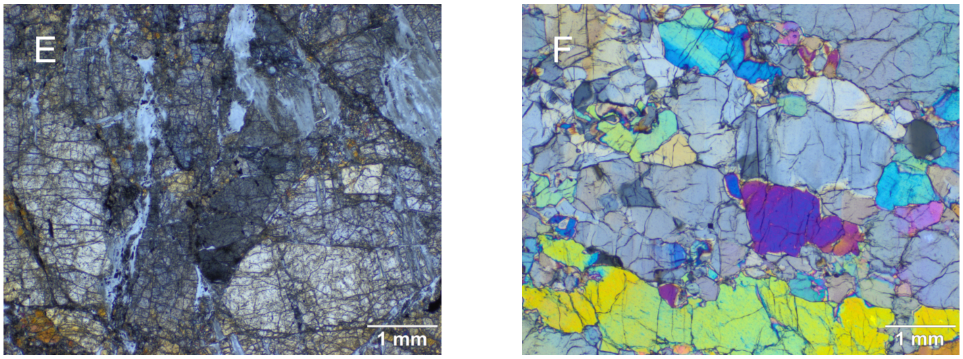

T2S8 (1.5 RA, 547 ncc He/g) Grey TW (0.8 RA, 88 ncc He/g)

Figure 1.S4. Photomicrographs (cross polarized light) of representative thin sections. Panels A-F are arranged in order of consecutively decreasing $^{3}He/^{4}He_{T}$ ratio. Note that He_{T} concentrations range from 10-27 ncc-He/g in panels A-C and from 88-574 ncc-He/g in panels D-F, and that fracture density increases between panels A-C and panels D-F. These observations support a role of fracturing and serpentinization in introducing the 1±0.5 R_{A} component.

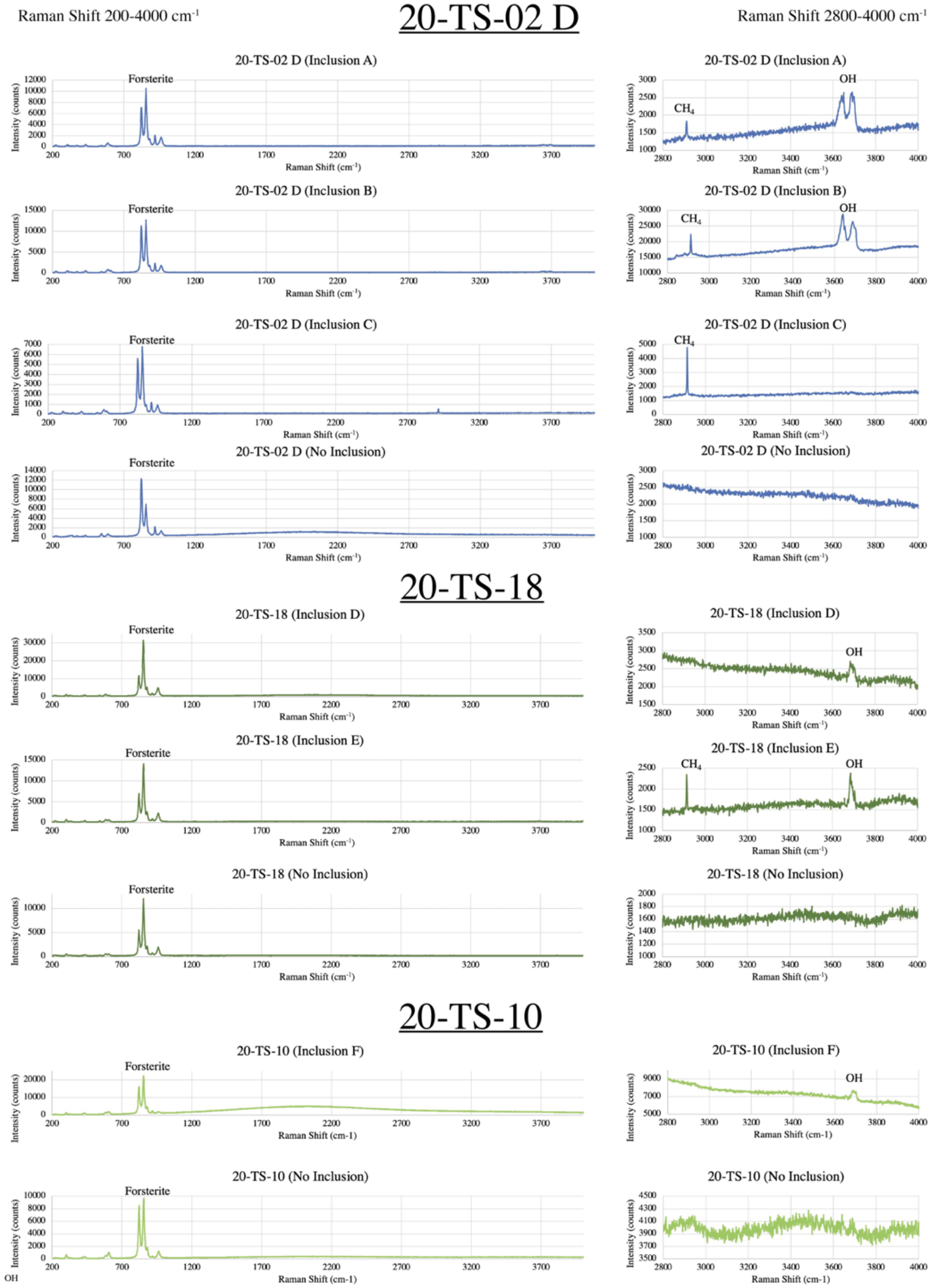

Figure 1.S5. A subset of the Raman spectra gathered from olivine grains in from one ~1 R_A sample (20-TS-02 D) and two high-R_A samples (20-TS-10 and 20-TS-18). Methane (CH_4) and OH-bearing inclusion minerals (lizardite and brucite) are detected in both the high-R_A samples and the ~1 R_A the sample but show a strong preference towards the ~1 R_A sample. Methane was only detected once in the high-R_A samples (Inclusions E) but was found numerous times in the ~1 R_A sample.

Chapter One References

Albarède, F., 2008. Rogue Mantle Helium and Neon. *Science*, *319*, 943–945.

Allègre, C. J., Moreira, M., Staudacher, T. 1995. ^{4}He/^{3}He dispersion and mantle convection. *Geophy. Res. Lett.*, *22*, 2325–2328.

Allen, D. E., Seyfried, W. E., 2003. Compositional controls on vent fluids from ultramafic-hosted hydrothermal systems at mid-ocean ridges: An experimental study at 400°C, 500 bars. *Geochim. Cosmochim. Acta*, *67*, 1531–1542.

Andersen, T., Neumann, E.-R., 2001. Fluid inclusions in mantle xenoliths. *Lithos*, *55*, 301–320.

Andrews, J. N., 1985. The isotopic composition of radiogenic helium and its use to study groundwater movement in confined aquifers. *Chem. Geol.*, *49*, 339–351.

Andrews, J. N., Hussain, N., Youngman, M. J., 1989. Atmospheric and radiogenic gases in groundwaters from the Stripa granite. *Geochim. Cosmochim. Acta*, *53*, 1831–1841.

Baxter, E. F., Asimow, P. D., Farley, K. A., 2007. Grain boundary partitioning of Ar and He. *Geochim. Cosmochim. Acta*, *71*, 434–451.

Blackwell, D. D., Steele, J. L., Kelley, S., Korosec, M. A., 1990. Heat flow in the state of Washington and thermal conditions in the Cascade Range. *J. Geophys. Res.*, *95*, 19495-19516.

Blard, P.-H., Puchol, N., Farley, K. A., 2008. Constraints on the loss of matrix-sited helium during vacuum crushing of mafic phenocrysts. *Geochim. Cosmochim. Acta*, *72*, 3788–3803.

Bodnar, R. J., Binns, P. R., Hall, D. L., 1989. Synthetic fluid inclusions—VI. Quantitative evaluation of the decrepitation behaviour of fluid inclusions in quartz at one atmosphere confining pressure. *J. Metamorph. Geol. 7*, 229–242.

Braun, M. G., Kelemen, P. B., 2002. Dunite distribution in the Oman Ophiolite: Implications for melt flux through porous dunite conduits. *Geochem. Geophys. Geosystems*, *3*, 1–21.

Brett, R. C., Russell, J. K., Andrews, G. D. M., Jones, T. J., 2015. The ascent of kimberlite: Insights from olivine. *Earth Planet. Sci. Lett.*, *424*, 119–131.

Brownfield, M. E., Affolter, R. H., Stricker, G. D., Hildebrand, R. T., 1995. High chromium contents in Tertiary coal deposits of northwestern Washington—A key to their depositional history. *Int. J. Coal Geol.*, *27*, 153–169.

Burnard, P. G., Farley, K. A., Turner, G., 1998. Multiple fluid pulses in a Samoan harzburgite. *Chem. Geol.*, *147*, 99–114.

Burnard, P. G., Stuart, F., Turner, G., 1994. C He Ar variations within a dunite nodule as a function of fluid inclusion morphology. *Earth Planet. Sci. Lett.*, *128*, 243–258.

Burnard, P., Graham, D., Turner, G., 1997. Vesicle-Specific Noble Gas Analyses of "Popping Rock": Implications for Primordial Noble Gases in Earth. *Science*, *276*, 568–571.

Cherniak, D. J., Watson, E. B., 2012. Diffusion of helium in olivine at 1 atm and 2.7 GPa. *Geochim. Cosmochim. Acta*, *84*, 269–279.

Christensen, N. I., 2002. Continental mantle seismic anisotropy: A new look at the Twin Sisters massif. *Tectonophysics*, *355*, 163–170.

Cox, S. E., Miller, H. B. D., Hofmann, F., Farley, K. A., 2022. Short communication: Mechanism and prevention of irreversible trapping of atmospheric He during mineral crushing. *Geochronology*, *4*, 551–560.

Czuppon, G., Matsumoto, T., Handler, M. R., Matsuda, J., 2009. Noble gases in spinel peridotite xenoliths from Mt Quincan, North Queensland, Australia: Undisturbed MORB-type noble gases in the subcontinental lithospheric mantle. *Chem. Geol.*, *266*, 19–28.

Dann, J. C., 1991. Early Proterozoic ophiolite, central Arizona. *Geology*, *19*, 590-593.

Debret, B., Albers, E., Walter, B., Price, R., Barnes, J. D., Beunon, H., Facq, S., Gillikin, D. P., Mattielli, N., Williams, H., 2019. Shallow forearc mantle dynamics and geochemistry: New insights from IODP Expedition 366. *Lithos*, *326–327*, 230–245.

Dodson, A., Brandon, A. D., 1999. Radiogenic helium in xenoliths from Simcoe, Washington, USA: Implications for metasomatic processes in the mantle wedge above subduction zones. *Chem. Geol.*, *160*, 371–385.

Dunai, T. J., Porcelli, D., 2002. Storage and Transport of Noble Gases in the Subcontinental Lithosphere. *Rev. Mineral. Geochem.*, *47*, 371–409.

Ehlers, T. A., Farley, K. A., Rusmore, M. E., Woodsworth, G. J., 2006. Apatite (U-Th)/He signal of large-magnitude accelerated glacial erosion, southwest British Columbia. *Geology*, *34*, 765-768.

Evans, B. W., 2010. Lizardite versus antigorite serpentinite: Magnetite, hydrogen, and life(?). *Geology*, *38*, 879–882.

Evans, W. C., van Soest, M. C., Mariner, R. H., Hurwitz, S., Ingebritsen, S. E., Wicks, C. W., Schmidt, M. E., 2004. Magmatic intrusion west of Three Sisters, central Oregon, USA: The perspective from spring geochemistry. *Geology*, *32*, 69-72.

Farley, K. A., 2002. (U-Th)/He Dating: Techniques, Calibrations, and Applications. *Rev. Mineral. and Geochem.*, *47*, 819–844.

Farley, K. A., Neroda, E., 1998. Noble Gases in the Earth's Mantle. *Annu. Rev. Earth Planet. Sci.*, *26*, 189–218.

Farley, K. A., Treffkorn, J., Hamilton, D., 2020. Isobar-free neon isotope measurements of flux-fused potential reference minerals on a Helix-MC-Plus mass spectrometer. *Chem. Geol.*, *537*, 1-10.

Ferré, E. C., Tikoff, B., Jackson, M., 2005. The magnetic anisotropy of mantle peridotites: Example from the Twin Sisters dunite, Washington. *Tectonophysics*, *398*, 141–166.

Francis, S., 2019. *Quantifying the magnitude and spatial variability of bedrock erosion beneath the Sisters Glacier, Washington, using cosmogenic ^{3}He concentrations* (857) [Masters Thesis, Western Washington University]. WWU Graduate School Collection.

Frasse, F., 1981. *Geology and Structure of the Western and Southern Margins of Twin Sisters Mountain, North Cascades, Washington* (639) [Masters Thesis, Western Washington University]. WWU Graduate School Collection.

Furnes, H., de Wit, M., Staudigel, H., Rosing, M., Muehlenbachs, K., 2007. A Vestige of Earth's Oldest Ophiolite. *Science*, *315*, 1704–1707.

Gautheron, C., Moreira, M., 2002. Helium signature of the subcontinental lithospheric mantle. *Earth Planet. Sci. Lett.*, *199*, 39–47.

Graham, D. W., 2002. Noble Gas Isotope Geochemistry of Mid-Ocean Ridge and Ocean Island Basalts: Characterization of Mantle Source Reservoirs. *Rev. Mineral. Geochem.*, *47*, 247–317.

Grozeva, N. G., Klein, F., Seewald, J. S., Sylva, S. P., 2020. Chemical and isotopic analyses of hydrocarbon-bearing fluid inclusions in olivine-rich rocks. *Phil. Trans. Royal. Soc. A*, *378*, 1-28.

Hansteen, T. H., Klügel, A., Schmincke, H.-U., 1998. Multi-stage magma ascent beneath the Canary Islands: Evidence from fluid inclusions. *Contrib. to Mineral. Petrol.*, *132*, 48–64.

Hart, S. R., 1984. He diffusion in olivine. *Earth Planet. Sci. Lett.*, *70*, 297–302.

Heber, V. S., Brooker, R. A., Kelley, S. P., Wood, B. J. (2007). Crystal–melt partitioning of noble gases (helium, neon, argon, krypton, and xenon) for olivine and clinopyroxene. *Geochim. Cosmochim. Acta*, *71*, 1041–1061.

Hilton, D. R., Fischer, T. P., Marty, B., 2002. Noble Gases and Volatile Recycling at Subduction Zones. *Rev. Mineral. Geochem.*, *47*, 319–370.

Horton, F., Farley, K., Jackson, M., 2019. Helium distributions in ocean island basalt olivines revealed by X-ray computed tomography and single-grain crushing experiments. *Geochim. Cosmochim. Acta*, *244*, 467–477.

Humphreys, E. D., Grunder, A. L. (2022). Tectonic controls on the origin and segmentation of the Cascade Arc, USA. *Bull. Volcanol.*, *84*, 1-13.

Jackson, C. R. M., Parman, S. W., Kelley, S. P., Cooper, R. F., 2013. Constraints on light noble gas partitioning at the conditions of spinel-peridotite melting. *Earth and Planet. Sci. Lett.*, *384*, 178–187.

Kant, L. B., Tepper, J. H., Eddy, M. P., Nelson, B. K. (2018). Eocene Basalt of Summit Creek: Slab breakoff magmatism in the central Washington Cascades, USA. *Lithosphere, 10,* 792-805.

Kelemen, P. B., Braun, M., Hirth, G., 2000. Spatial distribution of melt conduits in the mantle beneath oceanic spreading ridges: Observations from the Ingalls and Oman ophiolites. *Geochem. Geophys. Geosystems*, *1*, 1-21.

Kelemen, P. B., Hirth, G., Shimizu, N., Spiegelman, M., Dick, H. J., 1997. A review of melt migration processes in the adiabatically upwelling mantle beneath oceanic spreading ridges. *Phil. Trans. Royal. Soc. A*, *355*, 283–318.

Kelemen, P. B., Shimizu, N., Salters, V. J. M., 1995. Extraction of mid-ocean-ridge basalt from the upwelling mantle by focused flow of melt in dunite channels. *Nature*, *375*, 747–753.

Kipfer, R., Aeschbach-Hertig, W., Peeters, F., Stute, M., 2002. Noble Gases in Lakes and Ground Waters. *Rev. Mineral. Geochem.*, *47*, 615–700.

Klein, F., Grozeva, N. G., Seewald, J. S., 2019. Abiotic methane synthesis and serpentinization in olivine-hosted fluid inclusions. *Proc. Natl. Acad. Sci. U. S. A.*, *116*, 17666–17672.

Kruckenberg, S. C., Tikoff, B., Toy, V. G., Newman, J., Young, L. I., 2013. Strain localization associated with channelized melt migration in upper mantle lithosphere: Insights from the Twin Sisters ultramafic complex, Washington, USA. *J. Struct. Geol.*, *50*, 133–147.

Kurz, M. D., Colodner, D., Trull, T. W., Moore, R. B., O'Brien, K., 1990. Cosmic ray exposure dating with in situ produced cosmogenic ^{3}He: Results from young Hawaiian lava flows. *Earth Planet. Sci. Lett.*, *97*, 177–189.

Kurz, M. D., Warren, J. M., Curtice, J., 2009. Mantle deformation and noble gases: Helium and neon in oceanic mylonites. *Chem. Geol.*, *266*, 10–18.

Kusky, T. M., Li, J.-H., Tucker, R. D., 2001. The Archean Dongwanzi Ophiolite Complex, North China Craton: 2.505-Billion-Year-Old Oceanic Crust and Mantle. *Science*, *292*, 1142–1145.

Lamadrid, H. M., Zajacz, Z., Klein, F., Bodnar, R. J., 2021. Synthetic fluid inclusions XXIII. Effect of temperature and fluid composition on rates of serpentinization of olivine. *Geochim. Cosmochim. Acta*, *292*, 285–308.

Lao, Y., Anderson, R. F., Broecker, W. S., Hofmann, H. J., Wolfli, W., 1993. Particulate fluxes of ^{230}Th, ^{231}Pa, and ^{10}Be in the northeastern Pacific Ocean. *Geochim. Cosmochim. Acta*, *57*, 205–217.

Lee, J.-Y., Marti, K., Severinghaus, J. P., Kawamura, K., Yoo, H.-S., Lee, J. B., Kim, J. S., 2006. A redetermination of the isotopic abundances of atmospheric Ar. *Geochim. Cosmochim. Acta*, *70*, 4507–4512.

Mark, D. F., Stuart, F. M., de Podesta, M., 2011. New high-precision measurements of the isotopic composition of atmospheric argon. *Geochim. Cosmochim. Acta*, *75*, 7494–7501.

Marty, B., Lussiez, P., 1993. Constraints on rare gas partition coefficients from analysis of olivine-glass from a picritic mid-ocean ridge basalt. *Chem. Geol.*, *106*, 1–7.

Matsumoto, T., Chen, Y., Matsuda, J. 2001. Concomitant occurrence of primordial and recycled noble gases in the Earth's mantle. *Earth Planet. Sci Lett.*, *185*, 35–47.

Miller, R. B., Bryant, K. I., Doran, B., Eddy, M. P., Raviola, F. P., Sylva, N., Umhoefer, P. J. (2022). Eocene dike orientations across the Washington Cascades in response to a major strike-slip faulting episode and ridge-trench interaction. *Geosphere*, *18*, 697–725.

Onyeagocha, A. C., 1978. Twin Sisters dunite: Petrology and mineral chemistry. *Geol. Soc. Am. Bull.*, *89*, 1459-1474.

Pagé, P., Bédard, J. H., Schroetter, J.-M., Tremblay, A., 2008. Mantle petrology and mineralogy of the Thetford Mines Ophiolite Complex. *Lithos*, *100*, 255–292.

Parman, S. W., Kurz, M. D., Hart, S. R., Grove, T. L., 2005. Helium solubility in olivine and implications for high 3He/4He in ocean island basalts. *Nature*, *437*, 1140–1143.

Patterson, D. B., Farley, K. A., McInnes, B. I. A., 1997. Helium isotopic composition of the Tabar-Lihir-Tanga-Feni island arc, Papua New Guinea. *Geochim. Cosmochim. Acta*, *61*, 2485–2496.

Pirard, C., Hermann, J., O'Neill, H. ST. C., 2013. Petrology and Geochemistry of the Crust–Mantle Boundary in a Nascent Arc, Massif du Sud Ophiolite, New Caledonia, SW Pacific. *J. Petrol.*, *54*, 1759–1792.

Porcelli, D., Ballentine, C. J., 2002. Models for Distribution of Terrestrial Noble Gases and Evolution of the Atmosphere. *Rev. Mineral. Geochem.*, *47*, 411–480.

Protin, M., Blard, P.-H., Marrocchi, Y., Mathon, F., 2016. Irreversible adsorption of atmospheric helium on olivine: A lobster pot analogy. *Geochim. Cosmochim. Acta*, *179*, 76–88.

Ragan, D. M., 1963. Emplacement of the Twin Sisters dunite, Washington. *Am. J. Sci.*, *261*, 549–565.

Recanati, A., Kurz, M. D., Warren, J. M., Curtice, J., 2012. Helium distribution in a mantle shear zone from the Josephine Peridotite. *Earth Planet. Sci. Lett.*, *359–360*, 162–172.

Reiners, P. W., Ehlers, T. A., Mitchell, S. G., Montgomery, D. R., 2003. Coupled spatial variations in precipitation and long-term erosion rates across the Washington Cascades. *Nature*, *426*, 645–647.

Robin-Popieul, C. C. M., Arndt, N. T., Chauvel, C., Byerly, G. R., Sobolev, A. V., Wilson, A., 2012. A New Model for Barberton Komatiites: Deep Critical Melting with High Melt Retention. *J. Petrol., 53*, 2191–2229.

Rospabé, M., Benoit, M., Candaudap, F., 2018a. Determination of Trace Element Mass Fractions in Ultramafic Rocks by HR-ICP-MS: A Combined Approach Using a Direct Digestion/Dilution Method and Preconcentration by Coprecipitation. *Geostand. Geoanal. Res.*, *42*, 115–129.

Rospabé, M., Benoit, M., Ceuleneer, G., Hodel, F., Kaczmarek, M.-A., 2018b. Extreme geochemical variability through the dunitic transition zone of the Oman ophiolite: Implications for melt/fluid-rock reactions at Moho level beneath oceanic spreading centers. *Geochim. Cosmochim. Acta*, *234*, 1–23.

Shuster, D. L., Farley, K. A., Sisterson, J. M., Burnett, D. S., 2004. Quantifying the diffusion kinetics and spatial distributions of radiogenic ^{4}He in minerals containing proton-induced 3He. *Earth Planet. Sci. Lett.*, *217*, 19–32.

Skeen, C., Crandell, W., 2003. *Computerized spectrographic data for two new USGS rocks, AMH-1 and DTS-2* (USGS Open-File Report No. 89–183; USGS Open-File Report).

Symonds, R., Poreda, R., Evans, W., Janik, C., Ritchie, B. (2003). *Mantle and crustal sources of carbon, nitrogen, and noble gases in Cascade-Range and Aleutian-Arc volcanic gases* (Open-File Report No. 03–436; USGS Open-File Report).

Thompson, G. A., Robinson, R., 1975. Gravity and Magnetic Investigation of the Twin Sisters Dunite, Northern Washington. *Geol. Soc. Am. Bull.*, *86*, 1413.

Tikoff, B., Larson, C. E., Newman, J., Little, T., 2010. Field-based constraints on finite strain and rheology of the lithospheric mantle, Twin Sisters, Washington. *Lithosphere*, *2*, 418–422.

Torgersen, T., Kennedy, B. M., Hiyagon, H., Chiou, K. Y., Reynolds, J. H., Clarke, W. B., 1989. Argon accumulation and the crustal degassing flux of ^{40}Ar in the Great Artesian Basin, Australia. *Earth Planet. Sci. Lett.*, *92*, 43–56.

Toy, V. G., Newman, J., Lamb, W., Tikoff, B., 2010. The Role of Pyroxenites in Formation of Shear Instabilities in the Mantle: Evidence from an Ultramafic Ultramylonite, Twin Sisters Massif, Washington. *J. Petrol.*, *51*, 55–80.

Trull, T. W., Kurz, M. D., 1993. Experimental measurements of 3He and 4He mobility in olivine and clinopyroxene at magmatic temperatures. *Geochim. Cosmochim. Acta*, *57*, 1313–1324.

Trull, T. W., Kurz, M. D., Jenkins, W. J., 1991. Diffusion of cosmogenic3He in olivine and quartz: Implications for surface exposure dating. *Earth Planet. Sci. Lett.*, *103*, 241–256.

Valkiers, S., Vendelbo, D., Berglund, M., de Podesta, M., 2010. Preparation of argon Primary Measurement Standards for the calibration of ion current ratios measured in argon. *Int. J. Mass Spectrom.*, *291*, 41–47.

Vance, J., Dungan, M., Blanchard, D., Rhodes, J. M., 1980. Tectonic Setting and Trace Element Geochemistry of Mesozoic Ophiolitic Rocks in Western Washington. *Am J. Sci.*, *280-A*, 359–388.

Wanamaker, B. J., Wong, T.-F., Evans, B., 1990. Decrepitation and crack healing of fluid inclusions in San Carlos olivine. *J. Geophys. Res.*, *95*, 15623-15641.

Wang, K., Lu, X., Brodholt, J. P., 2020. Diffusion of noble gases in subduction zone hydrous minerals. *Geochim.Cosmochim. Acta*, *291*, 50–61.

Whetten, J. T., Zartman, R. E., Blakely, R. J., Jones, D. L., 1980. Allochthonous Jurassic ophiolite in northwest Washington. *Geol. Soc. Am. Bull.*, *91*, 359-368.

Wunder, B., Wirth, R., Gottschalk, M., 2001. Antigorite: Pressure and temperature dependence of polysomatism and water content. *Eur. J. Mineral.*, *13*, 485–495.

Yamamoto, J., Kaneoka, I., Nakai, S., Kagi, H., Prikhod'ko, V. S., Arai, S., 2004. Evidence for subduction-related components in the subcontinental mantle from low 3He/4He and 40Ar/36Ar ratio in mantle xenoliths from Far Eastern Russia. *Chem. Geol.*, *207*, 237–259.

Ye, X., Tao, M., Yu, C., Zhang, M., 2007. Helium and neon isotopic compositions in the ophiolites from the Yarlung Zangbo River, Southwestern China: The information from deep mantle. *Sci. Chi. Ser. D*, *50*, 801–812.

Zhang, L., Wang, Q., Ding, X., Li, W.-C., 2021. Diverse serpentinization and associated abiotic methanogenesis within multiple types of olivine-hosted fluid inclusions in orogenic peridotite from northern Tibet. *Geochimi. Cosmochim. Acta*, *296*, 1–17.

Zhang, S. Y., Zhang, H. L., Hou, Z., Ionov, D. A., Huang, F., 2019. Rapid Determination of Trace Element Compositions in Peridotites by LA - ICP - MS Using an Albite Fusion Method. *Geostand. Geoanal. Res.*, *43*, 93–111.

Chapter 2

PRECISE AND ACCURATE DETERMINATION OF CARBONATE-SPECIFIC TRACE ELEMENT COMPOSITIONS IN MAGNESITE-BEARING SOILS

2.1 Abstract

Magnesium carbonates in surficial environments act as temporary sinks for CO_2 and can record aspects of the palaeohydrological cycles on Earth and Mars. In many natural samples, magnesium carbonates are intimately intermixed at the micrometer scale with complex assemblages of other non-carbonate minerals. To better understand magnesium carbonate paragenesis in diverse samples, we developed and validated methods for sample cleaning, digestion, and quadrupole inductively coupled plasma mass spectrometry (ICP-MS) to measure the trace and minor elemental composition of magnesite and dolomite recovered from host sediments while obviating contributions from other authigenic and detrital minerals. Labile, adsorbed elements were removed by pre-washing powdered samples with ammonium acetate, and magnesium carbonates were selectively digested in hot (90°C) acetic acid. Accurate quantification of rare earth elements, redox sensitive elements, and other trace and minor elements (e.g., Sr) in the carbonate was accomplished by matrix-matching major elements for solution ICP-MS analysis. Accuracy was assessed with spike recovery experiments.

The pre-cleaning and selective digestion method was applied to a depth profile of fluvial sediment samples from the Kunwarara magnesite mine, Queensland, Australia. Separation and analysis of magnesite ± dolomite nodules and their host sediments identified previously

unrecognized geochemical trends. In particular, the Ce anomaly (Ce*) in the Mg-carbonate diminishes with depth coincident with decreasing abundances of authigenic Fe/Mn-oxides/hydroxides in the host sediments. These results indicate that the pedogenic magnesium carbonates may replace the host sediments along redox gradients also recorded in the distribution of Fe/Mn-oxides/hydroxides, capturing interactions between oxidizing surface waters and reducing groundwaters. Application of this approach to extraterrestrial or Martian analog magnesium carbonate occurrences and their host rocks could yield constraints on the redox conditions in which the carbonates formed, shedding light on the pH-Eh conditions of waters of ancient Mars.

2.2 Introduction

While Mg-carbonate is relatively uncommon on Earth, these minerals have become increasingly relevant to the scientific community due to their orbital and in situ detection on the Martian surface, particularly at Jezero Crater, the exploration site for the Mars 2020 Perseverance rover (Brown *et al.*, 2020; Clavé *et al.*, 2023; Ehlmann *et al.*, 2008; Farley *et al.,* 2022; Scheller *et al.*, 2021, 2022). Trace element concentrations (and derived quantities such as Ce anomaly) within carbonates are useful because they place constraints on the fluid conditions (such as pH and Eh) in which the carbonates formed, thereby recording past hydrological conditions (e.g., Liu *et al.*, 1988; Smrzka *et al.*, 2019; Zhao *et al.*, 2022). Digestion protocols utilized for determining trace element concentrations in Ca-carbonates (such as calcite and aragonite) by selectively digesting the carbonate while eliminating the influences of contaminant phases and adsorbed trace elements on grain surfaces have been developed and assessed in great detail (e.g., Boyle, 1981; Cao *et al.*, 2020; Tostevin *et al.*, 2016; Yu *et al.*, 2005; Zhao *et al.*, 2022). However, magnesium carbonates such as magnesite (trigonal $MgCO_3$) and dolomite (trigonal $CaMg(CO_3)_2$) are less soluble and their elemental compositions are generally determined by aggressive whole-rock digestions. Magnesite is particularly challenging to process with weak acids due to its extreme insolubility. Digestion protocols for solution ICP-MS analyses of magnesite have involved heated bulk digestions in HNO_3 + HF (e.g., Fernandez-Nieto *et al.*, 2003; Kilias *et al.*, 2006; Lugli *et al.*, 2000) or HNO_3 + HCl (e.g., Dong *et al.*, 2016; Kuşcu *et al.*, 2017). Following implementation of heated HNO_3 + HF digestions, Fernandez-Nieto *et al.* (2003) and Lugli *et al.* (2000) found that REE concentrations and those of other trace elements (e.g., Rb, Cs, Ga, Zr, Th, V, and Sc in Lugli *et al.*, 2000) were positively correlated with Si and Al concentrations in the magnesites. It was concluded that the reported values of many trace elements were largely controlled by the presence of co-existing detrital aluminosilicate phases. While heated digestions in HNO_3 + HCl implemented by Dong *et al.* (2016) and Kuşcu *et al.* (2017) would not be expected to dissolve silicate grains, these strong, oxidizing acids still may attack other phases, such as iron oxides and water-soluble salts, and trace elements adsorbed onto grain surfaces, introducing trace and minor elements not present in the carbonate into the final analytical solution (Cao *et al.*, 2020).

To mitigate these influences, others have attempted direct separation of non-carbonate phases by physical means prior to conducting chemical analyses (e.g., Henjes-Kunst *et al.*, 2014; Mervine *et al.*, 2015). However, while large contaminant grains may be removed by hand picking or density and magnetic separation, separating fine contaminant phases may be impossible (e.g., Mervine *et al.*, 2015). Additionally, such an approach would do little to remove trace elements that are adsorbed onto the surfaces of carbonate grains but not incorporated into the crystal lattice.

Some researchers have determined trace element concentrations of portions of Mg-carbonate visibly free of contaminant grains via laser ablation inductively coupled plasma mass spectrometry (LA-ICP-MS) and secondary ion mass spectrometry (SIMS) (e.g., Eiler *et al.*, 2002; Lu *et al.*, 2022). These methods may be appropriate for measuring concentrations of trace elements in sufficiently large Mg-carbonate grains. However, such analyses may not adequately represent trace element characteristics of bulk carbonate at a larger scale due to local heterogeneities. These procedures can also be complicated by other analytical difficulties such as sample porosity, which is typical of cryptocrystalline carbonates (Pittman, 1971).

Here, we adapt a leaching and digestion protocol developed to determine trace element concentrations in calcite by Cao *et al.* (2020) and apply it to magnesite±dolomite samples to obviate the influence of contaminants or trace elements adsorbed onto mineral surfaces. Our method involves two initial leaching steps to drive down the amount of adsorbed trace elements on grain surfaces by exchange with ammonium, followed by removal of water-soluble contaminants such as halite. After the leaching steps, carbonate in the samples is selectively digested in 0.3 M acetic acid at 90°C for 1-2 hours and filtered to remove residual aluminosilicates and metal-oxide particles. Samples were analyzed in 5% HNO_3 via solution quadrupole ICP-MS, and elemental concentrations in the carbonates were determined by calibration to matrix-matched (magnesium-enriched) multi-element standards. We also performed recovery tests to assess the accuracy of our analyses.

To demonstrate the efficacy of this protocol to selectively digest the Mg-carbonates, we compare elemental concentrations and derived products such as Ce anomaly (Ce*) determined by this procedure with those determined by heated 5% nitric acid digestion for several magnesite±dolomite samples collected from an open pit mine in Kunwarara, Queensland, Australia. Magnesite±dolomite nodules were sampled along a depth profile in the Kunwarara magnesite mine, where pedogenic Mg-carbonate nodules and cements formed by replacement of detrital fluvial sediments and are intimately associated with authigenic phyllosilicates, oxides, and silica phases (Milburn and Wilcock, 1994, 1998; Searston, 1998). Results suggest that the linkage between coprecipitating Fe/Mn-oxides/hydroxides and low Ce* in Mg-carbonates can be applied to constrain redox conditions in near-surface environments on Earth and Mars at the time of carbonate formation.

2.3 Methods

2.3.1 Sample Descriptions and Selection

Pedogenetic Mg-carbonates (magnesite±dolomite) analyzed in this study were collected from the Qmag magnesite mine in Kunwarara, Marlborough, Queensland, Australia from exposures in a fresh mine pit wall. The pit mine excavated into fluvial sediments exposes various types of pedogenic Mg-carbonates (pure magnesite and magnesite+dolomite) (Milburn and Wilcock, 1994, 1998; Searston, 1998).

Two of the carbonate samples were selected for their mineralogical purity (K-10.8) or complexity (K-7.6) to test the efficacy of the leaching method implemented in this study (See Figure 2.1). These carbonate samples were split into several aliquots to compare the leaching method with a 5% nitric acid digestion heated to 90°C. All other carbonates were analyzed only by the leaching method described in Section 2.3.2. Metadata associated with the Mg-carbonate samples is presented in Table 2.1. Paired host sediment samples for magnesites

K-7.6, K-9.8, and K-10.8 were collected at the same depths and <10 cm away from the carbonates. All host sediment samples are denoted with the same sample name as its carbonate pair but with an S at the end (e.g., K-7.6S). An additional sand sample (K-3.4S) was collected from the uppermost horizon which was completely free of carbonate (0-6.8 M depth). At the 8.3-9.3 m depth range, a magnesite+dolomite sample (K-8.8) and its associated host sediment (K-8.8S) were collected, but only the host sediment sample was analyzed due to the heterogeneity of the carbonate sample at the hand sample scale (~1-10 cm). Metadata associated with the paired host sediment samples is also presented in Table 2.1. Annotated profile photographs and representative portions of the Mg-carbonate samples are presented in Figure 2.2. A paired host sediment sample for K-11.8 was collected as well, but the sample was later found to contain ~10-30 vol% of finely disseminated carbonate, which was not readily separable from the host sediment by mechanical means. Thus, sample K-11.8S was not analyzed for whole rock chemistry and is not discussed in further sections of this work.

Sample M22-224E was used as a baseline for a recovery test. It was collected from the Old Man South pit, Kunwarara mine, and represents the outer edge of an ~5 cm diameter magnesite nodule. The solution resulting from processing this sample by the leaching method outlined in this work serves only as a baseline for a recovery test of the trace elements measured in these samples.

Table 2.1. Metadata associated with analyzed samples from the Kunwarara magnesite mine. Mgs stands for magnesite, Dol stands for dolomite, Fe/Mn-O stands for Fe/Mn-oxides/hydroxides, and Si-O-Al stands for aluminosilicates. The depth in meters is measured relative to the surface.

Sample Name	Field Label	Rock Type	Depth (m)	Description	Texture
K-3.4S	19-AUS-20S	Sed	0-6.8	Si-O-Al, Fe/Mn-O, Clay	Brittle
K-7.6	19-AUS-19	Mgs+Dol	6.8-8.3	Mgs+Dol Nodule	Soft
K-7.6S	19-AUS-19S	Sed	6.8-8.3	Si-O-Al, Fe/Mn-O, Clay	Brittle
K-8.8S	19-AUS-24S	Sed	8.3-9.3	Si-O-Al, Fe/Mn-O, Clay	Brittle
K-9.8	19-AUS-23	Mgs	9.3-10.3	Mgs Nodule	Hard
K-9.8S	19-AUS-23S	Sed	9.3-10.3	Si-O-Al, Fe/Mn-O, Clay	Brittle
K-10.8	19-AUS-22	Mgs	10.3-11.3	Mgs Nodule	Hard
K-10.8S	19-AUS-22S	Sed	10.3-11.3	Si-O-Al, Clay	Brittle
K-11.8	19-AUS-21	Mgs	11.3-12.3	Mgs Nodule	Hard
M22-224E	M22-224E	Mgs		Mgs Nodule	Hard

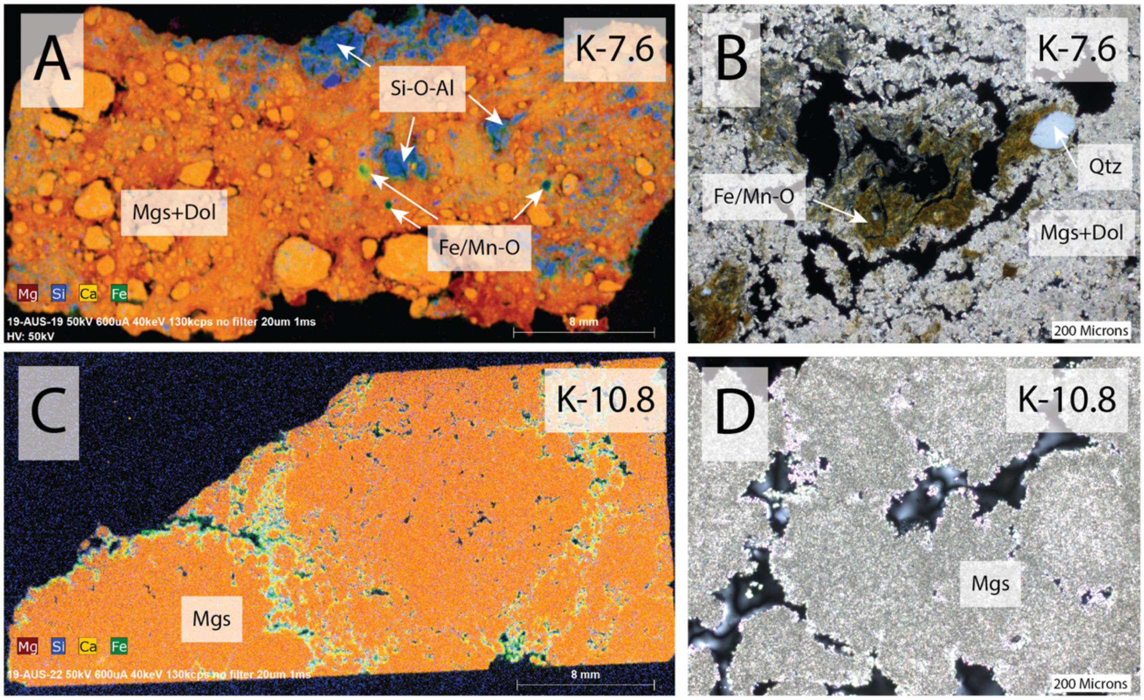

Figure 2.1. Representative micro-XRF (x-ray fluorescence) images (A&C) and optical images of thin sections taken in cross polarized light (B&D) of K-7.6 (A-B) and K-10.8 (C-D). We use the following abbreviations (in parenthesis): Magnesite (Mgs), dolomite (Dol), Fe/Mn-oxides/hydroxides (Fe/Mn-O), and aluminosilicates (Si-O-Al). Magnesite shows up as orange (yellow+red) as opposed to red because Ca is more fluorescent than Mg.

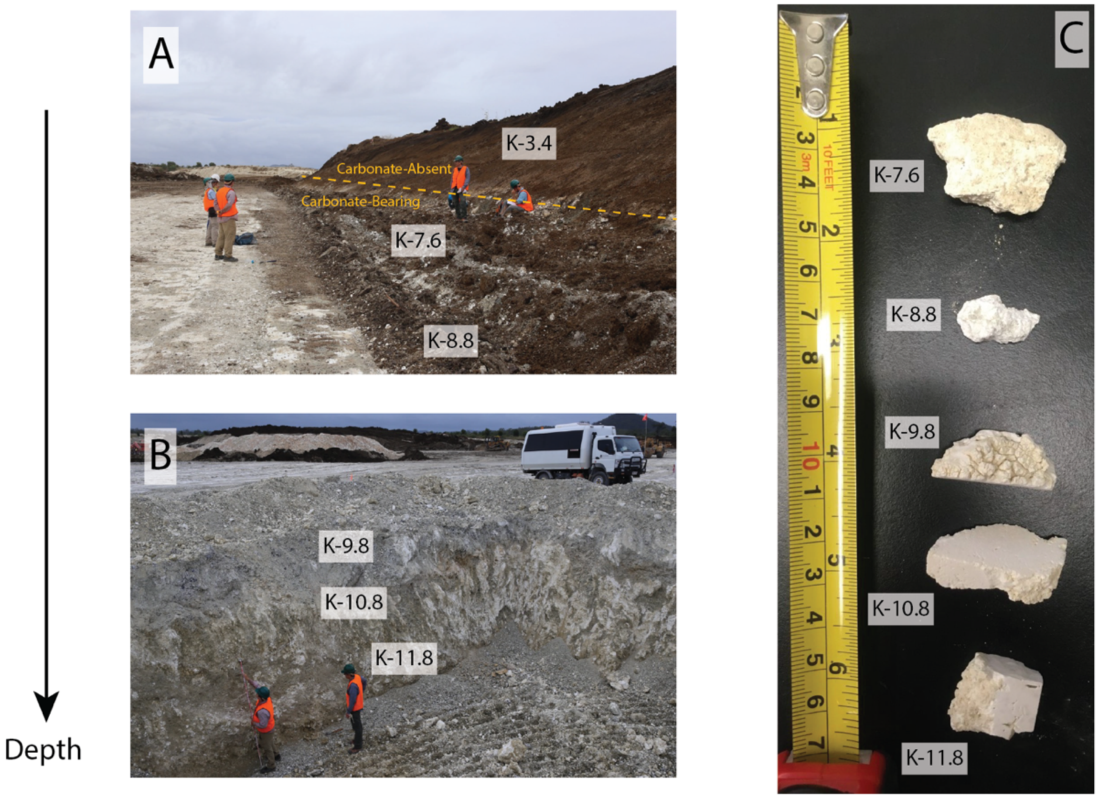

Figure 2.2. Depth transect at Kunwarara (Panels A and B) and photographs of portions of the Mg-carbonate nodules collected along the depth profile (Panel C). The people in the photographs in Panels A and B function as a semi-quantitative scale. True depth ranges at which samples were collected are available in Table 2.1. The base of the pit in Panel A at an equivalent depth to the surface of the pit in Panel B.

2.3.2 Leaching Method

Aliquots of Mg-carbonate powder (~4.5-9 mg) were produced by gently abrading carbonate fragments from a sample or using a diamond-studded high-speed rotary drill to extract 5-mm diameter cores from the sample (M22-224E: 1 aliquot). The abraded or drilled fragments were powdered lightly in an agate mortar and pestle (K-7.6: 8 aliquots & K-10.8: 2 aliquots, K-9.8: 1 aliquot, and K-11.8: 1 aliquot). The powders were subsequently loaded into 1.5 ml polypropylene centrifuge tubes. Sample batches were processed with three to four procedural blanks.

Methods for cleaning and dissolving magnesite samples for trace and minor element analysis were modified from Cao *et al.* (2020), whose protocol involves pre-cleaning carbonates in ammonium acetate and Milli-Q water, digesting in room temperature acetic acid, filtering insoluble residue, and analyzing the liquid fraction by solution ICP-MS. Because magnesite is less soluble in weak acid than other carbonate minerals, we include digestion in heated (rather than room temperature) acetic acid. The modified approach was validated by a recovery test and cross comparisons between samples that were processed by a weak nitric digest at 90°C.

The sample leaching and digestion protocol is schematically summarized in Figure 2.3. Samples were leached twice in 1.5 mL of 1.0 M ammonium acetate solution to dissolve water-soluble salts and remove adsorbed ions on grain surfaces by ion exchange with excess NH^{4+} ions. Ammonium acetate solution of pH 7 was prepared from anhydrous ammonium acetate (BioUltra Fluka Analytical) in 18.2 MΩ-cm ultrapure water (Millipore Milli-Q). The neutral pH of the ammonium acetate solution was confirmed using pH strips. Tubes containing the carbonate powder samples with ammonium acetate were shaken vigorously by hand to disperse the sample throughout the solution, sonicated for 15 minutes, shaken vigorously again, sonicated again for 15 more minutes, and shaken vigorously once more. Samples were centrifuged at 13,200 RPM for 10 minutes and the ammonium acetate solution was decanted away with a pipette, leaving behind residual Mg-carbonate material at the base of the centrifuge tubes. These steps were repeated twice.

Following the ammonium acetate rinses, samples were subsequently rinsed in 1.5 mL ultrapure Milli-Q water, shaken, and centrifuged at 13,200 RPM for 10 minutes before pipetting and discarding the supernatant. These Milli-Q rinses were repeated a total of three times to remove any residual trace elements leached from grain surfaces or incorporated in water-soluble salts.

Following these rinses, samples were resuspended in 1.5 mL of 0.3 M acetic acid, shaken, and poured into labeled 50 mL virgin polypropylene DigiTUBEs sourced from SCP SCIENCE (verified for leachable metal analyses by ICP-MS). The original centrifuge tubes were rinsed twice more with 1 mL of 0.3M acetic acid that was shaken and poured into DigiTUBEs to ensure complete transfer (>99%) of the samples from the centrifuge tubes into the DigiTUBEs. DigiTUBEs were capped and heated to 90°C for 1 to 2 hours until white carbonate powder was no longer visible (completely dissolved) and then cooled to near room temperature for >5 minutes. The solutions were filtered directly into a new set of labeled DigiTUBEs with 0.2-micron hydrophilic polyethersulfone membrane filters (Thermo Scientific) that were pre-rinsed with 0.3 M acetic acid; this step removes insoluble residual materials (likely silicates and oxides). Prior to drying, 6.5 ml of 5% nitric acid was added to the samples to oxidize acetate in solution while drying. Samples were dried down completely in DigiTUBEs with caps removed on a 90°C hot block for ~3-12 hours in a well-ventilated fume hood. Samples were then resuspended in 50 mL of 5% distilled nitric acid and left stored in capped DigiTUBEs for >12 hours at room temperature. Immediately prior to trace element analysis on the ICP-MS, samples were well shaken in DigiTUBEs to ensure that the solutions were well mixed.

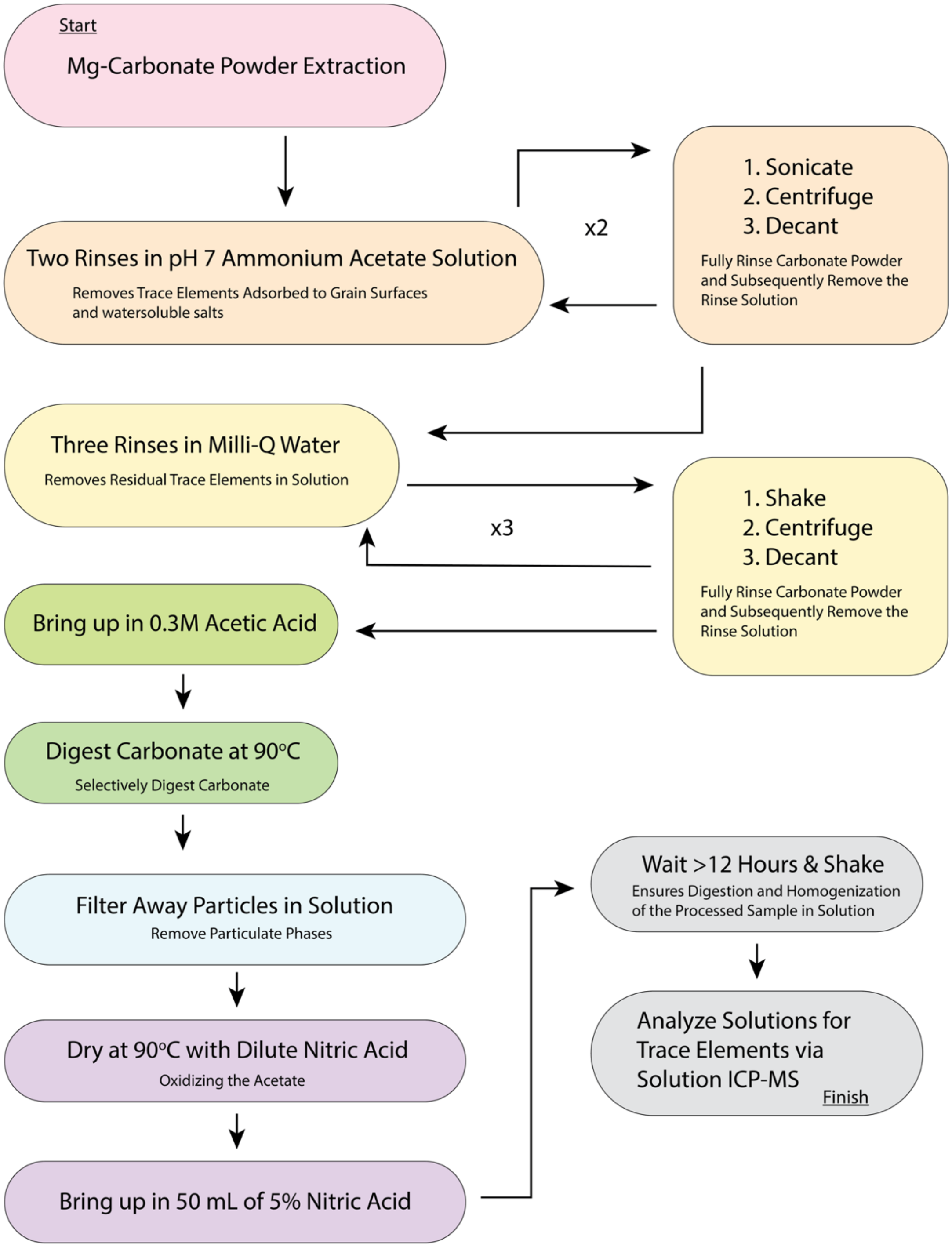

Figure 2.3. A schematic workflow diagram of the digestion protocol presented in this work modified from Cao *et al.* (2020) to be applied to magnesite±dolomite. Further details are described in Sections 2.3.2, 2.3.4, and 2.3.5.

2.3.3 Heated Digests in 5% Nitric Acid

To validate the efficacy of selectively digesting Mg-carbonate using the procedure described above, carbonate samples K-7.6 (8 aliquots), and K-10.8 (2 aliquots) were selected to undergo 5% distilled nitric acid digests that would still dissolve Fe/Mn-oxides/hydroxides. Three or more blanks were processed and analyzed with each batch of samples. Carbonate powders were weighed into 1.5 mL polypropylene centrifuge tubes. 1.5 mL of 5% nitric acid was introduced to each of the centrifuge tubes. The tubes were sonicated for 15 minutes, shaken by hand, and vented for approximately 5 seconds to release pressure build up from CO_2. The steps involving sonicating, shaking, and venting were repeated twice. Samples were then poured into DigiTUBEs. Centrifuge tubes were rinsed with 1 mL 5% nitric acid twice to remove any residual sample, and the solutions were poured into the DigiTUBEs, ensuring complete sample transfer. The samples were then digested in capped DigiTUBEs on a hot block at 90°C for 1-2 hours until none of the white powdery carbonate material was visible in solution. Solutions were filtered directly into a new set of labeled DigiTUBEs using 0.2-micron hydrophilic polyethersulfone membrane syringe filters that were pre-cleaned with 5% nitric acid. Solutions were dried down completely in DigiTUBEs at 90°C for ~3-6 hours and were then brought up to 50 mL in 5% distilled nitric acid. Samples were left stored in capped DigiTUBEs for >12 hours and shaken prior to ICP-MS analysis to ensure that solutions were well-mixed.

2.3.4 ICP-MS Trace Element Standardization

Standard solutions with initial volumes of 50 mL were prepared in 5% HNO_3. Mg was sourced from Spec Pure from Alfa Aesar, 1000 micro-g/mL Stock # 385; REEs (La, Ce, Pr, Nd, Sm, Eu, Gd, Tb, Dy, Ho, Er, Tm, Yb and Lu), Sc, Y, U, and Th used to calibrate standard solutions were sourced from Inorganic Ventures CMS-1; Sr used for standard solutions was sourced from MSSR-100PPM of Inorganic Ventures; Mo used for standard solutions was sourced from Fluka Analytical 04488-100 mL 1ppm Mo; Ca used for standard solutions was sourced from BDH Aristar Plus 82025-960 1000 ppm Ca; Cd, Co, Cr, Cu, Fe, Mn, Ni, V, and Zn used for standard solutions were sourced from Spectrum Transition Metals 44518 - 100 ppm.

A stock standard solution with the highest concentrations of trace elements contained 50,000 ppb Ca; 5,000 ppb Sr; 500 ppb Cd, Co, Cr, Cu, Fe, Mn, Ni, V, and Zn; 50 ppb of REEs, Sc, Y, U, and Th; 1 ppb Mo. Ca was standardized as a major element for analysis of sample K-7.6 due to the presence of dolomite. Five standards were produced with trace element concentrations equivalent to 10x, 100x, 1,000x, 10,000x, and 100,000x dilutions of the stock standard solution. When analyzing nearly pure magnesite samples (non-dolomitic), standards were matrix matched with 28.4 mg/L Mg to match the matrix of ~5 mg of magnesite dissolved in 50 ml of 5% nitric acid. In addition to these matrix-matched trace element standards, a 14.2 mg/L Mg solution and a 2.84 mg /L Mg solution were produced to construct calibration curves for Mg. A separate suite of standards was produced to measure trace elements (except for Ca) to match the matrix of sample K-7.6, which contained both dolomite and magnesite. The standards for trace element calibration contained 12.2 mg/L Ca and 20.0 mg/L Mg, respectively, matching digestion of ~5 mg of samples. The Ca/Mg of K-7.6 was determined via ICP-MS prior to these analyses to ensure accurate matrix matching. Standards for K-7.6 were produced with the same trace element concentrations as the standards that were matrix-matched with only Mg. Similarly, a separate suite of standards was produced with concentrations equivalent to a 2x dilution of the Ca-Mg matrix (6.1 mg/L Ca and 10.0 mg/L Mg) and a 10x dilution of the Ca-Mg matrix (1.22 mg/L Ca and 2.00 mg/L Mg) to construct calibration curves for Ca and Mg as major elements.

2.3.5 ICP-MS Protocol and Data Reduction

The isotopes ^{24}Mg, ^{43}Ca, ^{45}Sc, ^{51}V, ^{52}Cr, ^{55}Mn, ^{56}Fe, ^{59}Co, ^{60}Ni, ^{63}Cu, ^{66}Zn, ^{88}Sr, ^{89}Y, ^{95}Mo, ^{111}Cd, ^{139}La, ^{140}Ce, ^{141}Pr, ^{146}Nd, ^{147}Sm, ^{153}Eu, ^{157}Gd, ^{159}Tb, ^{163}Dy, ^{165}Ho, ^{166}Er, ^{169}Tm, ^{172}Yb, ^{175}Lu, ^{232}Th, and ^{238}U were all measured in solution using calibrated standard curves on an Agilent 8800 Triple Quadrupole ICP-MS at the Resnick Water and Environment Lab at the California Institute of Technology. Measured isotopes were selected based on natural abundance, potential interferences, and quality of the standard calibration curves. Dwell times were 0.1 seconds for Mg, Ca, Sc, Mn, Co, Ni, Cu, Zn, Cd, and Fe, and 4 seconds for all other measured elements. Three replicate scans of each element were collected, each of which consisted of 100 sweeps per replicate. All Mg data was recorded in analog mode. Concentration of other elements allowed them to by measured in pulse counting mode. Most elements were measured without using a collision cell gas, with the exception of Ca and Fe, which were measured using He [4.3 ml/min] as a collision cell gas (He-mode) to improve the quality of the calibration curve for ^{43}Ca and to prevent formation of polyatomic interferences, such as ^{40}Ar^{16}O for ^{56}Fe, that can form as the argon plasma ionizes the analyte solution. The accuracy and quality of the ^{43}Ca calibration curve in He-mode was consistently superior to that of ^{43}Ca in no-gas mode and ^{44}Ca and ^{46}Ca in either mode.

Barium forms polyatomic oxides and hydrides that interfere with REEs (Smirnova *et al.*, 2006). To account for these potential interferences, analysis of 10,000 ppb, 1,000 ppb, 100 ppb, and 10 ppb Ba in 5% nitric solutions demonstrated that the interferences become negligible at ~100 to 10 ppb Ba in solution. Ba in these solutions was sourced from a MSBA-100 ppm barium solution. ^{137}Ba, REEs, and Ba/REE ratios were qualitatively monitored in quick scan mode for every sample, and the results show that Ba counts account for <1% of the count rate of REE analyses and remained well below the analytical precision and accuracy of the REE analyses. The isotopes ^{23}Na, ^{28}Si, ^{31}P, ^{34}S, ^{35}Cl, and ^{39}K were also monitored in quick scan mode to estimate the influence of co-existing water-soluble salts, silicates, and phosphates. Counts of these isotopes remained close to procedural blank and acid blank levels in samples processed by the leaching method. Only very high counts of these masses would be indicative of contamination.

Results were converted to nanograms of element per gram of carbonate (ppb) and weight percent for elements that are traditionally considered major elements in the trigonal carbonate series (Mg, Ca, Fe, and Mn) using Equation 2.1:

$$[\mathrm{E_{carbonate}}]\left(\frac{\mathrm{g_E}}{\mathrm{g_{carbonate}}}\right) = \frac{[\mathrm{E_{solution}}]}{[\mathrm{Mg_{solution}}] + [\mathrm{Ca_{solution}}] + 60.01\left(\frac{[\mathrm{Mg_{solution}}]}{24.305} + \frac{[\mathrm{Ca}_{solution}]}{40.078}\right)} \tag{2.1}$$

Units of $\mathrm{E_{carbonate}}$ are grams of the element ($\mathrm{g_E}$) per gram carbonate ($\mathrm{g_{carbonate}}$). Equation (2.1) converts concentrations of element E in solution $[\mathrm{E_{solution}}]$ to concentrations of element in the carbonate $[\mathrm{E_{carbonate}}]$ using concentrations of Mg $[\mathrm{Mg_{solution}}]$ and Ca $[\mathrm{Ca_{solution}}]$ in solution, and molar masses of Ca (40.078 g/mol), Mg (24.305 g/mol), and CO_3 (60.01 g/mol). The last additive term in the denominator on the right side of the equation estimates the amount of CO_3 based on the measured Mg and Ca in solution.

The estimated mass of carbonate analyzed was determined by calculating the total Mg and Ca in 50 mL solution and reported as ppb concentrations in acid-soluble rock except where otherwise stated. All analytical data were corrected for acid blank background counts measured during analysis. In addition, elements that were present at concentrations of less than ten standard deviations above the average procedural blank concentrations are considered to occur below the limit of quantification and are thus not reported. Procedural blank corrections were applied to the reported data.

2.3.6 Matrix Matching Test

To test the effects of mismatching the Mg concentration of the matrix, four solutions were produced from the source solutions for the standards with the following trace element contents: 500 ppb Ca; 50 ppb Sr; 5 ppb Cd, Co, Cr, Cu, Fe, Mn, Ni, V, and Zn; 0.5 ppb of REEs, Sc, Y, U, and Th; 0.01 ppb Mo. The first solution contained 14,200 ppb Mg, which is equal to half the normal amount of matrix. The second solution contained 28,400 ppb Mg, which is the normal amount of matrix expected for 5 mg of sample. The third solution contained 42,600 ppb Mg, which is 50% more Mg than the normal amount of matrix. The fourth solution contained 56,800 ppb Mg, which is twice the normal amount of Mg used for matrix matching. These solutions were analyzed on the ICP-MS as described above (see Sections 2.3.4 and 2.3.5).

2.3.7 Recovery Test

To further assess the accuracy of this method, a recovery test was conducted by adding a known mass of each element analyzed (excluding Mg) to solutions derived from magnesite sample M22-224E by the leaching protocol described here. A 25 mL split of the solution was poured into a clean DigiTUBE. The solution was spiked with ~300 µL (weighed 0.3036 grams) of a concentrated trace element solution derived from the sources of the standard solutions (see Section 2.3.4). The trace element contributions from this spike propagated to known increases in concentrations of Ca by 99.60 ppb; REEs, Sc, Y, U, and Th by 0.5076 ppb; Cd, Co, Cr, Cu, Fe, Mn, Ni, V, and Zn by 5.076 ppb; Mo by 0.01015 ppb in the 25.3 mL M22-224E solution. Both the initial and spiked solutions were analyzed on the ICP-MS. The recovery % and spike % are calculated to assess the accuracy of this method as described in Equation 2.2:

$$\text{recovery \%} = 100 * \frac{M_{s\text{pike}} - M_{\text{initial}}}{K_{s\text{pike}}} \tag{2.2}$$

and Equation 2.3:

$$\text{spike \%} = 100 * \frac{K_{\text{spike}}}{K_{s\text{pike}} + M_{\text{initial}}} \tag{2.3}$$

respectively. Here K_{spike} is the known increase in concentration of an element resulting from the spike, M_{spike} is the measured concentration of an element in the spiked M22-224E solution and M_{initial} is the measured concentration of the initial (not spiked) M22-224E solution baseline.

2.3.8 XRF Analysis of Host Sediment Samples

Whole rock major and trace elements in host sediment samples were characterized by x-ray fluorescence (XRF) analysis as described in detail by Bucholz and Spencer (2019). Samples analyzed include K-3.4S, K-7.6S, K-8.8S, K-9.8S, and K-10.8S from the depth transect in the Kunwarara pit mine. As previously mentioned, host sediment sample K-11.8S was not analyzed for whole rock chemistry because it contained abundant carbonate cements and fragments that were not mechanically separable.

2.4 **Results**

Trace element concentrations in Mg-carbonates are presented in Tables 2.2-2.4. Calculated carbonate contents were determined by calculating the carbonate mass using the measured Mg and Ca and reporting it as a percentage of the weighed mass of the sample. Calculated carbonate content values are all lower than 100% for both the heated 5% nitric digests and the leaching method (Table 2.2). This could be attributed to a combination of factors: 1) a fraction of the sample solutions was retained in the syringe filters, 2) major insoluble phases were filtered away, and 3) fine particles suspended in solution were removed during decanting steps. The latter is only applicable to the samples processed by the leaching method. Nonetheless, there is no relationship between the calculated carbonate content and the trace element content for replicate analyses of samples such as K-7.6. Additionally, the normalization to the trigonal anhydrous carbonate series implemented when processing the data enables remediation of the factors addressed above as long as the total carbonate analyzed is within the bounds of the matrix matching experiments. This normalization is permitted by the ~blank level counts of other major elements monitored in quick scan mode and low concentration of all measured trace elements analyzed summed together following the normalization (<0.5 wt%). Matrix matching experiments reveal that trace element concentrations deviate by less than 10% from that of the regularly implemented 28,400 ppb Mg matrix. This permits the analysis of net-carbonate-masses ranging from ~2.5-10 mg per 50 ml solution to be analyzed (Section 2.6). Net carbonate masses analyzed range from 3.5-5.9 mg as calculated by multiplying the weighed mass by the calculated carbonate content as a fraction (see Table 2.2). Comparisons between the two digestion protocols implemented (leaching method and heated 5% nitric digest) are presented in detail in the following subsections to demonstrate the efficacy of the leaching protocol. Results from the accuracy tests are summarized and geochemical trends from the Kunwarara pit mine depth profile are reported.

2.4.1 Selective Digestion of Mg-Carbonate

Comparison of the sample K-7.6 processed by heated 5% nitric digests and the leaching method reveals decreases in redox sensitive trace elements and derived products (Ce anomaly) when applying our leaching protocol. The mean Fe and V concentrations determined by heated 5% nitric digests are over an order of magnitude higher than those determined by the leaching protocol (Figure 2.4). Mean concentrations of Mn determined by the leaching method match those measured by heated 5% nitric digests (Figure 2.4).

In comparison to the heated 5% nitric digest, concentrations of U and Th respectively decreased by 22%, and 32% on average when determined by the leaching method (Figure 2.4). Sc concentrations dropped by 33% on average (Figure 2.4). Ni concentrations are 7% lower on average when determined by the leaching protocol, and Co concentrations are 12%

lower on average when determined by the leaching protocol (Figure 2.4). Average concentrations of Mg, Ca, and Sr are nearly equal within 1σ for both digestion protocols; Ce concentrations are systematically lower in the leach than in the heated 5% nitric acid digestion, whereas those of other REEs and Y appear to be slightly elevated when processed by the leaching method (Figure 2.4).

The average Ce anomaly (Ce*) — where Ce* is defined as $Ce^* = 2 \times Ce_{CI}/(La_{CI}+Pr_{CI})$ — calculated from chondrite normalized (CI) REE concentrations (McDonough and Sun, 1995) is ~10% lower in the samples processed by the leaching method than in those digested in heated 5% nitric acid (Figure 2.4, Table 2.4). Even if alternative expressions for calculating Ce* (e.g., Barrat *et al.*, 2023) are applied, Ce* for the heated 5% nitric digests remains higher than those resulting from the leaching method.

Sample K-10.8 aliquots (visually/petrographically inclusion-free sample) analyzed by the two extraction techniques show ~35% decrease in the V concentrations and a ~50% decrease in the Fe concentration when utilizing the leaching protocol compared to the heated 5% nitric acid digest (Figure 2.5). Concentrations of other trace elements and Ce* are nearly indistinguishable at 1-2σ uncertainty (Figure 2.5, Tables 2.2-2.4). Elements below the limit of quantification for some replicates (Sc, Cr, Cu, Zn, Mo, Cd, Th, and U) cannot be reliably compared.

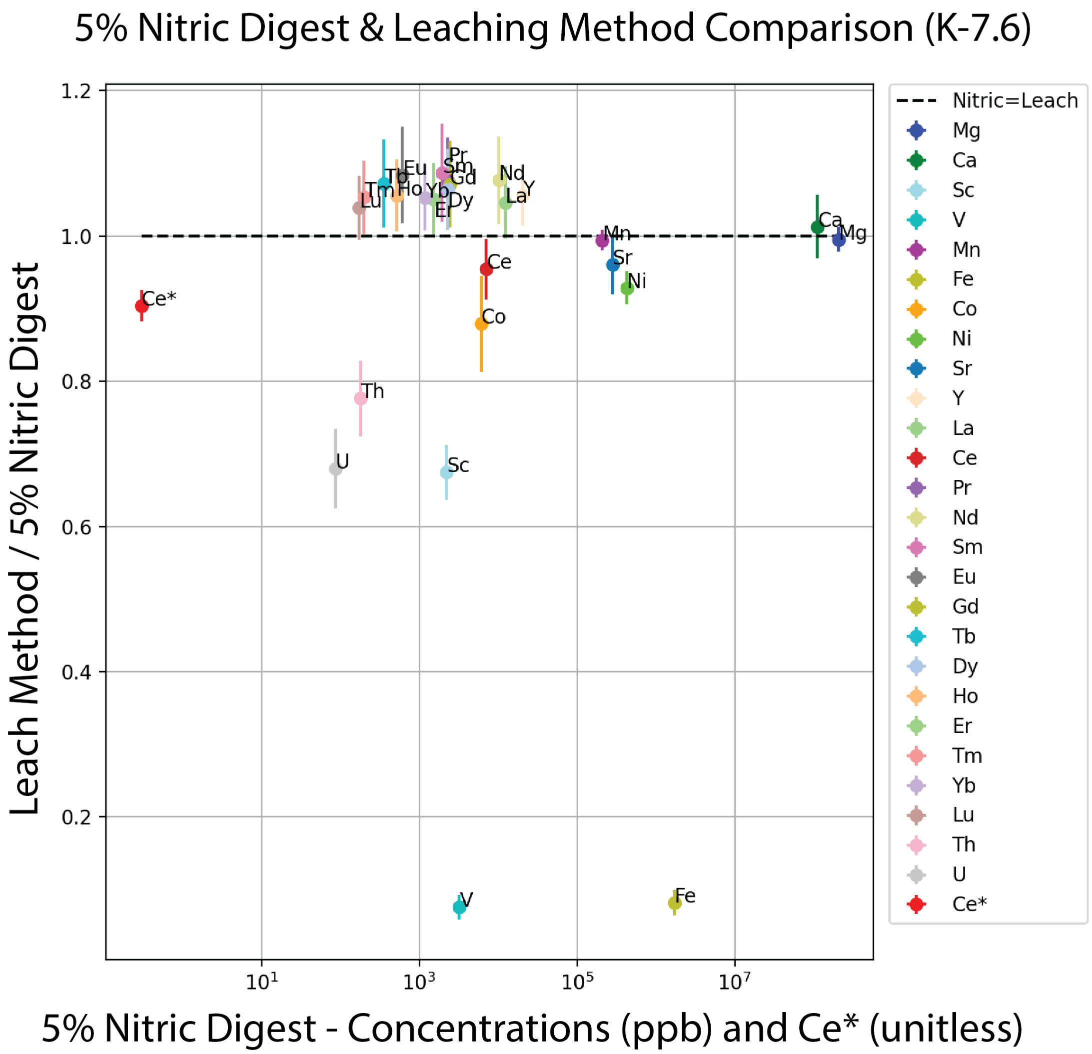

Figure 2.4. Average element concentrations and Ce* for K-7.6 determined by the 5% nitric digest (Nitric) plotted against the element concentrations and Ce* determined by the leaching method (Leach) normalized to those determined by the 5% nitric digest. Error bars represent 1σ uncertainties. The black dashed line indicates where values determined by the 5% nitric digest are equivalent those determined by the leaching method (Nitric=Leach).

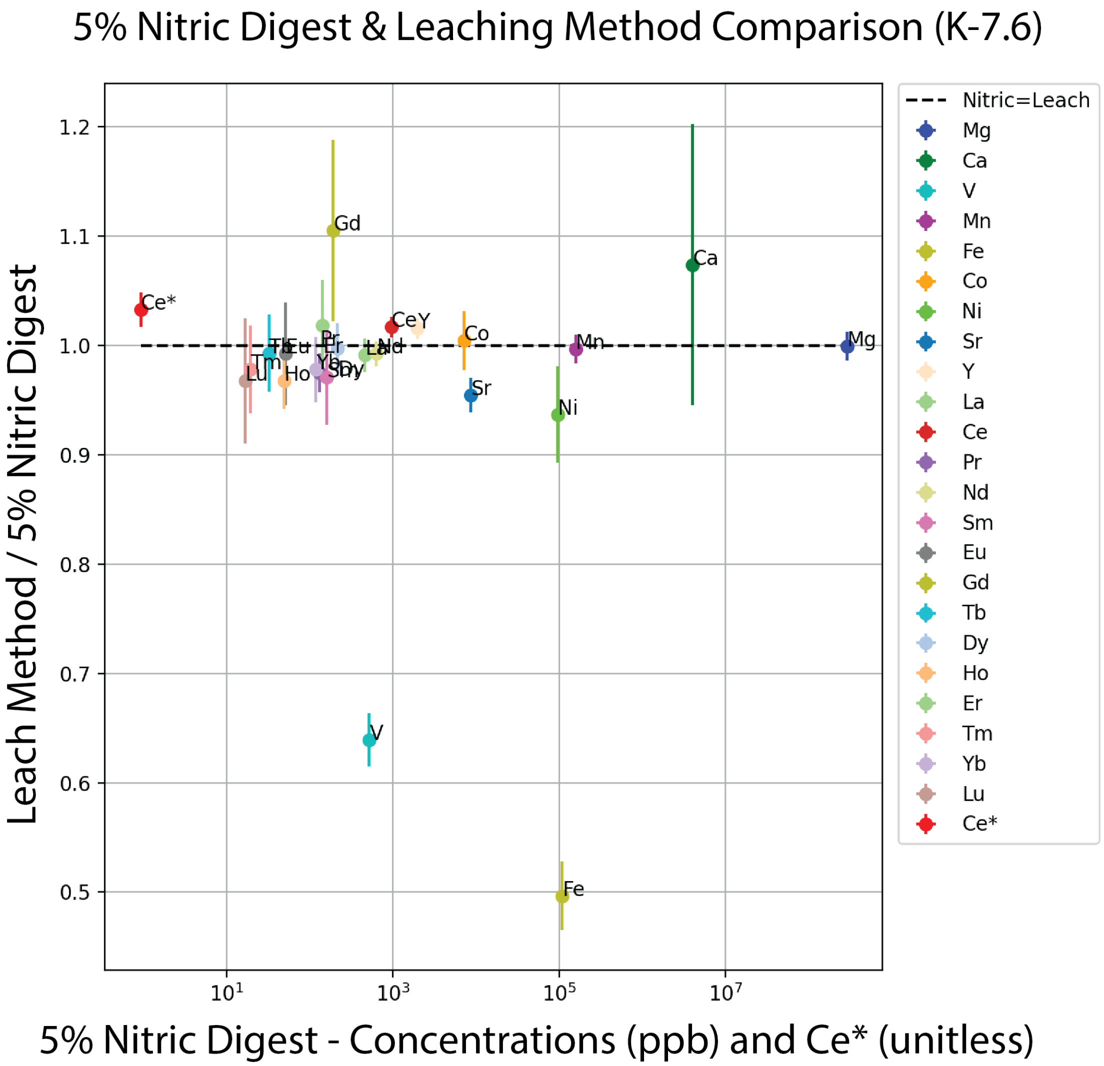

Figure 2.5. Average element concentrations and Ce* for sample K-10.8 determined by the 5% nitric digest (nitric) plotted against the element concentrations and Ce* determined by the leaching method (leach) normalized to those determined by the 5% nitric digest. Since only two aliquots of each sample were analyzed by both procedures, we plotted the average values and the 1σ precision added in quadrature and normalized by two to estimate 1σ uncertainty instead of using the standard deviation.

Table 2.2. Sample names, method, weighed masses, calculated carbonate content, and weight percent concentrations of Mg, Ca, Mn, and Fe and 1σ uncertainties. The numbers or letters in the paratheses following K-7.6 and K-10.8 indicate aliquot numbers and averages between samples processed by the same protocol (av). BQL indicates that an analysis was below the limit of quantification. In the Method column, “5% Nitric” indicates that the sample was processed by a heated 5% nitric digest while “Leach” indicates that the sample was processed by the leaching method.

Sample	Minerology	Method	Weighed Mass(mg)	Calculated Carbonate Content (%)	Mg wt%	Ca wt%	Mn wt%	Fe wt%
K-7.6 (1)	Mgs+Dol	Leach	8.3	69	20.11(22)	12.11(15)	0.02103(16)	0.00989(83)
K-7.6 (2)	Mgs+Dol	Leach	4.9	72	20.61(69)	11.42(52)	0.02076(86)	0.0154(13)
K-7.6 (3)	Mgs+Dol	Leach	6.5	55	20.12(42)	12.1(62)	0.0209(52)	0.0146(12)
K-7.6 (4)	Mgs+Dol	Leach	6.4	77	20.99(23)	10.89(26)	0.02078(24)	0.01299(94)
K-7.6 (5)	Mgs+Dol	Leach	4.8	78	20.67(65)	11.33(26)	0.02053(62)	0.0144(12)
K-7.6 (6)	Mgs+Dol	Leach	7.4	77	20.87(25)	11.06(32)	0.020753(96)	0.01142(79)
K-7.6 (7)	Mgs+Dol	Leach	5.1	78	20.91(79)	10.99(28)	0.02094(64)	0.0186(11)
K-7.6 (8)	Mgs+Dol	Leach	5.2	68	20.48(72)	11.59(22)	0.02107(79)	0.0156(14)
K-7.6 (av)	Mgs+Dol	Leach			20.59(34)	11.44(47)	0.02085(18)	0.0141(27)
K-7.6 (9)	Mgs+Dol	5% Nitric	5.1	89	20.74(38)	11.239(78)	0.02138(63)	0.1636(17)
K-7.6 (10)	Mgs+Dol	5% Nitric	6.5	88	20.737(90)	11.24(29)	0.02109(22)	0.1738(21)
K-7.6 (11)	Mgs+Dol	5% Nitric	4.8	91	20.64(24)	11.37(65)	0.02097(42)	0.1982(21)
K-7.6 (12)	Mgs+Dol	5% Nitric	5.7	89	20.66(19)	11.34(52)	0.02096(15)	0.1908(25)
K-7.6 (13)	Mgs+Dol	5% Nitric	4.7	89	20.86(25)	11.07(57)	0.02099(32)	0.1554(27)
K-7.6 (14)	Mgs+Dol	5% Nitric	5	86	20.63(44)	11.38(42)	0.02086(23)	0.1758(31)
K-7.6 (15)	Mgs+Dol	5% Nitric	4.7	88	20.77(54)	11.19(62)	0.02052(68)	0.1636(23)
K-7.6 (16)	Mgs+Dol	5% Nitric	6.1	87	20.533(26)	11.52(28)	0.021(11)	0.1524(20)
K-7.6 (av)	Mgs+Dol	5% Nitric			20.7(10)	11.29(14)	0.02097(24)	0.172(16)
K-9.8	Mgs	Leach	6.5	90	28.65(42)	0.248(44)	0.01771(19)	BQL
K-10.8 (1)	Mgs	Leach	5.9	69	28.54(58)	0.4(37)	0.01586(29)	0.00627(48)
K-10.8 (2)	Mgs	Leach	7.9	65	28.5(24)	0.455(75)	0.015349(97)	0.00447(36)
K-10.8 (3)	Mgs	5% Nitric	5	77	28.53(14)	0.408(52)	0.015766(96)	0.00989(49)
K-10.8 (4)	Mgs	5% Nitric	5.2	71	28.55(36)	0.388(18)	0.01555(27)	0.01175(34)
K-11.8	Mgs	Leach	6.4	80	28.56(21)	0.369(51)	0.01661(14)	BQL

Table 2.3. Rare earth element concentrations in carbonate samples from the Kunwarara mine in ppb by sample and method. In the Method column, "5% Nitric" indicates that the sample was processed via a 5% nitric acid digest and "Leach" indicates that the sample was processed by the leaching method. The numbers or letters in the paratheses following K-7.6 and K-10.8 indicate aliquot numbers and averages between samples processed by the same protocol (av). Uncertainties reported in the parentheses next to concentrations are 1σ.

Sample	Method	La	Ce	Pr	Nd	Sm	Eu	Gd	Tb	Dy	Ho	Er	Tm	Yb	Lu
K-7.6 (1)	Leach	13579(44)	7301(40)	2618(21)	11422(99)	2188(12)	682.9(50)	2733(28)	395.9(36)	2530(15)	565.6(27)	1666.3(67)	218.0(21)	1288.9(94)	189.6(33)
K-7.6 (2)	Leach	12710(270)	6560(160)	2496(68)	10930(270)	2116(63)	648(16)	2615(42)	379.3(60)	2426(64)	535(13)	1590(58)	209.4(96)	1250(28)	179.7(60)
K-7.6 (3)	Leach	13600(350)	6990(160)	2697(54)	11860(260)	2333(83)	719(13)	2820(94)	411(13)	2598(92)	571(18)	1672(78)	218.7(42)	1289(55)	182.8(47)
K-7.6 (4)	Leach	12612(90)	6693(38)	2440(20)	10741(22)	2065(21)	643.6(67)	2583(15)	373.4(48)	2378(21)	530.2(54)	1571(15)	201.2(26)	1212(19)	175.2(22)
K-7.6 (5)	Leach	12250(340)	6480(220)	2372(83)	10370(290)	2016(30)	624.6(76)	2468(64)	359.6(46)	2322(64)	515(17)	1512(59)	198.2(73)	1170(59)	170.2(23)
K-7.6 (6)	Leach	12544(95)	6711(44)	2435(18)	10680(100)	2079(17)	640(14)	2559(14)	374.7(20)	2384(31)	531.7(21)	1573(12)	203.9(14)	1212.2(56)	177.5(25)
K-7.6 (7)	Leach	12740(330)	6770(200)	2468(74)	10820(320)	2109(64)	646(21)	2610(100)	379.2(82)	2406(40)	542(15)	1580(65)	210.1(68)	1222(52)	175.4(71)
K-7.6 (8)	Leach	13130(220)	6820(120)	2564(60)	11220(310)	2173(53)	681(24)	2663(53)	386.1(85)	2482(76)	554(16)	1637(53)	216.2(30)	1281(17)	184.2(36)
K-7.6 (av)	Leach	12890(490)	6790(260)	2510(110)	11010(470)	2135(98)	661(31)	2630(110)	382(15)	2441(90)	543(19)	1600(54)	209.5(78)	1241(44)	179.3(61)
K-7.6 (9)	5% Nitric	12910(260)	7380(140)	2452(46)	10700(180)	2064(38)	640(14)	2535(57)	373.8(29)	2371(63)	528(12)	1558(41)	201.0(73)	1194(36)	174.19(80)
K-7.6 (10)	5% Nitric	12373.6(29)	7113(12)	2335(10)	10187(64)	1960(21)	604.9(93)	2446(30)	353.7(51)	2285(13)	514.8(48)	1516.7(43)	197.87(88)	1179.0(73)	170.3(40)
K-7.6 (11)	5% Nitric	12180(190)	7137(96)	2308(41)	10110(150)	1967(66)	611(17)	2450(82)	354.7(90)	2305(26)	515(17)	1523(17)	199.3(24)	1172(25)	173.3(20)
K-7.6 (12)	5% Nitric	12186(33)	7083(12)	2293(14)	10080(100)	1901(23)	598.7(54)	2425(24)	349.0(38)	2240.9(58)	508.2(51)	1498(16)	193.73(78)	1157.4(68)	169.6(14)
K-7.6 (13)	5% Nitric	12040(250)	7030(150)	2246(47)	9770(200)	1871(33)	578.5(41)	2330(41)	336.5(53)	2173(36)	491(12)	1456(38)	192.7(65)	1157(27)	168.3(56)
K-7.6 (14)	5% Nitric	12700(300)	7270(200)	2444(69)	10790(270)	2099(53)	650(20)	2635(64)	380.7(76)	2450(41)	544.3(41)	1623.9(44)	212.2(30)	1245(24)	182.3(40)
K-7.6 (15)	5% Nitric	11870(260)	6900(140)	2239(40)	9860(170)	1884(43)	587(22)	2382(54)	348(13)	2231(64)	502(13)	1497(43)	197.1(51)	1166(26)	170.4(34)
K-7.6 (16)	5% Nitric	12368(75)	7019(35)	2353(20)	10305(49)	1970(21)	608.9(15)	2460(35)	357.1(22)	2293(23)	510.7(54)	1511(11)	197.5(29)	1160(22)	173.3(19)
K-7.6 (av)	5% Nitric	12330(340)	7120(150)	2334(81)	10230(360)	1964(82)	610(24)	2458(93)	357(14)	2294(86)	514(16)	1523(50)	198.9(60)	1179(30)	172.7(44)
K-9.8	Leach	703.6(60)	1034.1(84)	193.24(39)	1003.3(22)	262.2(18)	94.7(25)	397.0(75)	62.83(40)	408.8(15)	91.1(25)	256.2(49)	33.16(15)	187.4(33)	28.54(84)
K-10.8 (1)	Leach	463.4(67)	983.7(58)	128.0(15)	631.4(82)	159.1(40)	50.7(36)	208(19)	32.31(76)	216.7(53)	48.1(14)	147.5(48)	18.71(91)	114.8(24)	15.9(12)
K-10.8 (2)	Leach	445.9(73)	968.5(40)	128.64(52)	629.9(67)	151.4(46)	50.4(11)	216(11)	31.79(83)	212.96(83)	47.0(12)	144.5(52)	19.33(64)	115.6(32)	16.51(81)
K-10.8 (3)	5% Nitric	468.5(42)	974.8(80)	135.1(26)	656.6(48)	162.9(82)	51.3(23)	211(15)	33.1(13)	222.5(62)	50.8(14)	148.1(40)	20.18(79)	122.1(52)	16.866(89)
K-10.8 (4)	5% Nitric	448.9(94)	945(14)	128.1(37)	614.2(85)	157.0(99)	50.6(19)	173(13)	31.4(15)	208.1(54)	47.5(10)	138.5(84)	18.71(81)	113.4(27)	16.6(13)
K-11.8	Leach	406.6(85)	1005.7(91)	132.6(36)	671.2(21)	164.9(12)	55.8(19)	215.9(70)	36.9(12)	262.2(51)	62.2(14)	186.1(19)	24.51(96)	144.2(28)	20.11(28)

Table 2.4. Trace element concentrations of Sc, V, Cr, Co, Ni, Cu, Zn, Sr, Y, Mo, Cd, Th, and U in ppb and Ce* (unitless) in carbonates from the Kunwarara mine. Uncertainties reported in parentheses next to concentrations and Ce* are 1σ. In the Method column, "5% Nitric" indicates that the sample was processed via a 5% nitric acid digest and "Leach" indicates that the sample was processed by the leaching method. The numbers or letters in the paratheses following K-7.6 and K-10.8 indicate the aliquot numbers and averages between samples processed by the same protocol (av). BQL indicates that an analysis was below the limit of quantification.

Sample	Method	Sc	V	Cr	Co	Ni	Cu	Zn	Sr	Y	Mo	Cd	Th	U	Ce*
K-7.6 (1)	Leach	1532(77)	201(17)	BQL	4994(71)	388800(1300)	3970(150)	BQL	287400(1200)	22369(89)	BQL	61.6(10)	142.7(44)	63.3(38)	0.2786(18)
K-7.6 (2)	Leach	1520(130)	317(35)	BQL	5250(340)	400000(16000)	BQL	BQL	262600(8900)	21220(550)	BQL	BQL	143.4(44)	58.5(49)	0.2657(78)
K-7.6 (3)	Leach	1590(110)	305(26)	BQL	5330(160)	393700(9600)	BQL	BQL	277700(6200)	22510(480)	BQL	BQL	152.0(23)	58.1(51)	0.2637(78)
K-7.6 (4)	Leach	1459(19)	198(20)	BQL	5410(150)	407800(6300)	3230(180)	BQL	266200(3000)	21150(230)	BQL	64.9(76)	139.1(12)	57.8(34)	0.2747(22)
K-7.6 (5)	Leach	1428(46)	260(26)	BQL	5360(230)	409500(9300)	3330(240)	BQL	257100(4500)	20620(390)	BQL	BQL	137.9(17)	54.5(42)	0.274(11)
K-7.6 (6)	Leach	1519(75)	168(16)	BQL	5522(32)	403600(2500)	3410(160)	BQL	265200(2400)	21100(210)	BQL	58.6(65)	128.7(20)	57.5(28)	0.2766(24)
K-7.6 (7)	Leach	1420(160)	244(29)	BQL	5480(330)	408000(13000)	2690(250)	BQL	266700(6800)	21250(520)	BQL	BQL	133.2(94)	58.9(42)	0.275(97)
K-7.6 (8)	Leach	1560(18)	284(26)	BQL	5333(93)	394000(13000)	3480(350)	BQL	280000(10000)	21990(690)	BQL	100(38)	147.3(31)	62.5(53)	0.268(59)
K-7.6 (av)	Leach	1503(62)	247(54)	BQL	5340(160)	400700(7800)	BQL	BQL	270000(10000)	21530(680)	BQL	BQL	140.5(75)	58.9(28)	0.272(55)
K-7.6 (9)	5% Nitric	2198(80)	3227(61)	39400(1300)	6010(140)	439000(12000)	BQL	BQL	290600(6800)	21170(390)	BQL	BQL	186.6(62)	84.4(32)	0.2978(71)
K-7.6 (10)	5% Nitric	2380(140)	3378(11)	41830(320)	5951(52)	438100(1500)	BQL	BQL	282900(1000)	20540(20)	BQL	BQL	192.0(46)	84.95(67)	0.29995(66)
K-7.6 (11)	5% Nitric	2186(50)	3142(69)	42790(890)	7050(150)	429700(9600)	10370(660)	37400(2700)	277200(4900)	20060(340)	45.9(56)	145(67)	184.4(39)	96.6(27)	0.3054(55)
K-7.6 (12)	5% Nitric	2327(38)	3548(41)	44940(520)	6138(88)	437400(3800)	BQL	BQL	280000(1700)	20209(97)	BQL	BQL	183.6(36)	89.0(14)	0.30355(96)
K-7.6 (13)	5% Nitric	2115(23)	3136(52)	38230(690)	6034(92)	431400(8600)	BQL	BQL	279700(4600)	20180(360)	BQL	71(49)	176.1(61)	84.01(75)	0.3056(79)
K-7.6 (14)	5% Nitric	2230(110)	3476(64)	42220(980)	5770(120)	424800(8000)	BQL	BQL	287000(4300)	20830(360)	BQL	103(26)	182.8(51)	92.8(47)	0.2967(98)
K-7.6 (15)	5% Nitric	2222(87)	3160(120)	39900(1400)	5840(230)	429000(12000)	BQL	BQL	273000(8300)	19650(510)	BQL	71(33)	172.2(50)	81.8(10)	0.3033(78)
K-7.6 (16)	5% Nitric	2178(40)	2944(15)	37320(330)	5771(42)	422600(1500)	BQL	BQL	282440(820)	20534(85)	BQL	BQL	170.7(28)	80.15(85)	0.2953(21)
K-7.6 (av)	5% Nitric	2229(84)	3250(200)	40800(2500)	6070(420)	431500(6300)	BQL	BQL	281600(5500)	20400(480)	BQL	BQL	181.1(74)	86.7(56)	0.3009(40)
K-9.8	Leach	363(41)	269.9(54)	BQL	10150(200)	218300(4500)	BQL	BQL	7535(39)	3168(28)	BQL	BQL	2.44(32)	7.75(66)	0.668(64)
K-10.8 (1)	Leach	BQL	322(15)	BQL	7250(110)	90600(6200)	BQL	BQL	8310(120)	2025(24)	BQL	BQL	BQL	BQL	0.962(11)
K-10.8 (2)	Leach	BQL	345.7(62)	BQL	7160(120)	88200(5300)	BQL	BQL	8212(37)	1978(14)	BQL	BQL	BQL	7.22(70)	0.967(10)
K-10.8 (3)	5% Nitric	BQL	458(14)	BQL	7260(330)	95050(530)	BQL	BQL	8630(150)	2001(13)	BQL	BQL	5.4(12)	BQL	0.927(12)
K-10.8 (4)	5% Nitric	BQL	585(27)	8000(390)	7090(110)	95900(2400)	BQL	BQL	8690(210)	1942(19)	38.3(46)	BQL	BQL	BQL	0.941(22)
K-11.8	Leach	232(44)	637(10)	BQL	2720(100)	BQL	BQL	BQL	9142(97)	2250(30)	BQL	BQL	BQL	7.05(63)	1.043(20)

2.4.2 Recovery and Matrix Matching Tests

Results from the recovery test are presented in Table 2.5. The accuracy of the ICP-MS method is better than 5%, except for Fe (27%), Zn (7%), and Sc (6%). The recovery of Fe was less accurate than that of other elements. Recall that Fe was measured using the ^{56}Fe isotope in He-mode with the intention of negating the ^{40}Ar^{16}O interference. This interference may still be problematic when analyzing ~5 mg samples with <0.02 wt% Fe (Table 2.2) that have been diluted to 50 ml, which equates to <20 ppb Fe in solution given the high relative abundance of ^{16}O in the analyte and ^{40}Ar in the ionizing argon plasma. Slight instabilities associated with this interference over time could plausibly influence recovery at low Fe concentrations. Nonetheless, analyzing solutions in He-mode mitigates the ^{40}Ar^{16}O interference, which would otherwise make measurements of trace amounts of Fe impractical.

Table 2.5. Results from the recovery test in which known amounts of trace elements were added to a split solution of sample M22-224E. Recovery % is the difference between the spiked and the initial solution, normalized to the amount of spike added, as a percentage (Eq. 2.2). Spike % is the known amount of a trace element from the spike normalized by total amount in solution, as a percentage (Eq. 2.3).

Element	Recovery %	Spike %
Ca	103	22
Sc	106	93
V	97	99
Cr	100	97
Mn	99	21
Fe	127	41
Co	99	89
Ni	98	44
Cu	99	89
Zn	107	51
Sr	98	99
Y	97	72
Mo	96	82
Cd	99	100
La	99	86
Ce	97	69
Pr	98	95
Nd	96	80
Sm	97	94
Eu	98	98
Gd	98	93
Tb	98	99
Dy	98	94
Ho	98	99
Er	98	96
Tm	98	100
Yb	98	97
Lu	98	100
Th	97	100
U	96	99

Regarding the matrix matching test, increasing or decreasing the Mg matrix by a factor of two influences concentrations of U, Mo, and Fe by less than 8%; Th by less than 7%; Ca, Cr, and Sc by less than 6%; Cd, Sr, Zn, Co, and V by less than 4%; Lu, Yb, Tm, Er, Y, Cu, Ni, and Mn by less than 3%; Ho, Dy, Tb, Gd, Sm, Pr, Ce, and La by less than 2%; Nd and Eu by less than 1% of that of the 28,400 ppb Mg solution. Results indicated that matrix matching will influence the accuracy of trace element concentrations by <10% for net-carbonate-masses of 2.5-10 mg per 50 ml solution. A summary of the results of these tests are plotted in Fig. 2.6 and reported in Table 2.S1.

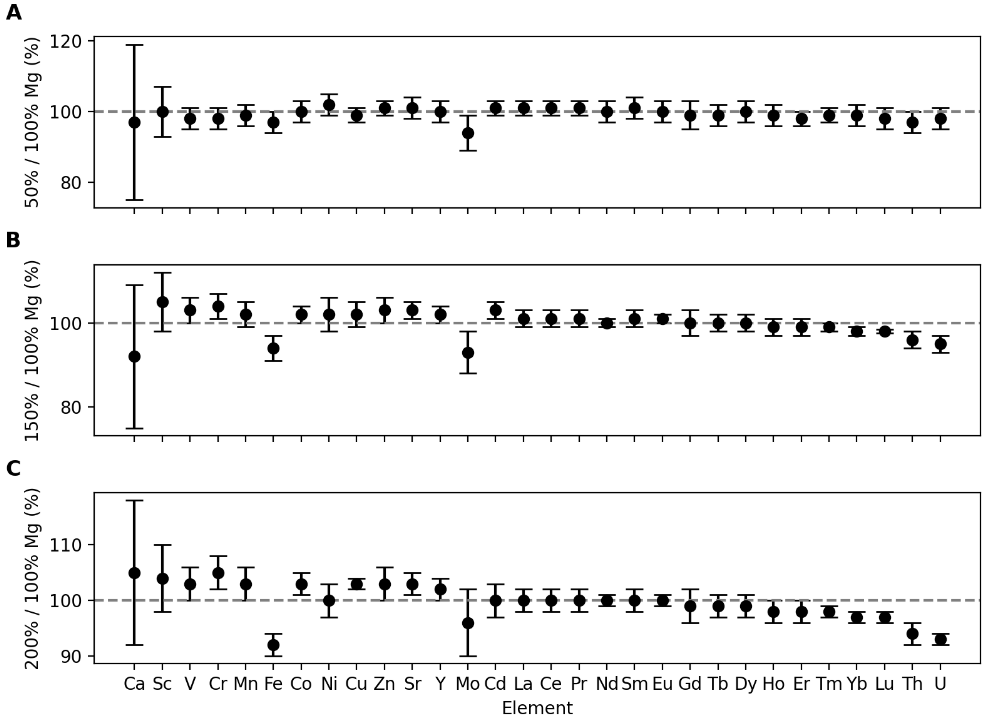

Figure 2.6. Results from matrix matching experiments by element. Concentration of the 50%, 150% and 200% Mg matrix solutions are normalized to those of the 100% Mg matrix solution in panels A (50% / 100% Mg), B (150% / 100% Mg), and C (200% / 100% Mg), respectively. The dashed grey lines indicate where concentrations of the elements in the mismatched matrix (50%, 150% and 200%) and 100% Mg matrix are the same. Uncertainties are 1σ.

In Figure 2.6, most elements are within analytical precision at ~1-2σ of those in the 28,400 ppb Mg solution. Relatively large uncertainties for Ca in the experiments can be attributed to relatively poor analytical precision associated with measuring trace amounts of ^{43}Ca with helium as a reaction cell gas. Fe depletion in the 200% Mg matrix experiment may be attributed to inconsistent deterrence of the ^{40}Ar^{16}O interferences by helium in the collision cell (Figure 2.6.C). Note that Th and U concentrations in the 200% Mg matrix experiment are also slightly depleted compared to the 100% Mg matrix.

2.4.3 Precision and Procedural Blanks of the Leaching Method

Precision includes the analytical precision associated with the instrument as well as the procedural blank corrections, which are mostly negligible. Among the REEs and Y, the 1σ precision is better than 10% of the reported concentration and is about 2% on average. The 1σ precision of Fe, Cu, V, and U spans from ~2% to ~10% of their reported concentration and the 1σ precision of Mg, Mn, and Sr is better than ~4%. The precisions of Co and Ni are better than 7% of their reported concentration and are about 3% on average. The 1σ precision of Ca and Sc widely spans from ~1% to ~18% of their reported concentrations. The 1σ precision of Ca tends to increase where Ca transitions from a major element (~10 wt%) to a minor element (<1 wt%). The 1σ precision of Cd and Th span 10-40% and 1-13% respectively.

Maximum procedural blank masses associated with the leaching method span between 100-600 nanograms for Mg, Ca, and Fe, 10-100 nanograms for Ni and Zn, 1-10 nanograms for Mn and Cu, and are less than one nanogram for all other elements analyzed (Table 2.S2). Given 5 mg of digested magnesite, the Mg blank constitutes no more than 0.05% of the analysis. Alternatively, given 5 mg of digested dolomite, the Mg and Ca blanks should account for no more than 0.1% and 0.06% of the analysis respectively.

2.4.4 Reproducibility

To assess the extent to which the external reproducibility associated with the analysis of multiple aliquots of the same powder compares to the internal uncertainty associated with analyzing individual aliquots, we define σ_{internal} as the 1σ precision on the replicate analyses, and σ_{external} as the standard deviation calculated from the reported concentrations of the replicate analyses (Tables 2.2-2.4). If the external reproducibility is as expected for a homogeneous powder given the internal uncertainties, then $\sigma_{\text{internal}}/\sigma_{\text{external}} \cong 1$. Alternatively, if the external reproducibility is greater (less reproducible) than one would expect, then $\sigma_{\text{internal}}/\sigma_{\text{external}} < 1$. If not analytical, a $\sigma_{\text{internal}}/\sigma_{\text{external}} < 1$ could be attributed to the heterogeneity of a powder. If $\sigma_{\text{internal}}/\sigma_{\text{external}} > 1$, then the internal uncertainty is greater (more uncertain) than one would expect given the external reproducibility, suggesting that the analytical precision (σ_{internal}) is overreported.

While the internal precision of each element is variable between aliquots, using the $\sigma_{\text{internal}}/\sigma_{\text{external}}$ ratios of each element and Ce*, we show that aliquots where $\sigma_{\text{internal}}/\sigma_{\text{external}} \cong 1$ are present for most elements and Ce* (Figure 2.7). Fe and V consistently exhibit $\sigma_{\text{internal}}/\sigma_{\text{external}}$ values below one. Fe $\sigma_{\text{internal}}/\sigma_{\text{external}}$ increases from ~0.1-0.2 for heated 5% nitric acid digests to ~0.3-0.5 when processed by the leaching method. V $\sigma_{\text{internal}}/\sigma_{\text{external}}$ also tends to improve when adopting the leaching method. Methodological distinctions in $\sigma_{\text{internal}}/\sigma_{\text{external}}$ appear for Ca, Co, and U as well (Figure 2.7). While $\sigma_{\text{internal}}/\sigma_{\text{external}}$ of some other redox sensitive elements (Ni, Co, and U), Sc and Ce* exhibit scatter around $\sigma_{\text{internal}}/\sigma_{\text{external}} \cong 1$ (spanning ~0-2), Sr, Th, and the REEs tend to exhibit $\sigma_{\text{internal}}/\sigma_{\text{external}}$ values spanning from about one to below. The $\sigma_{\text{internal}}/\sigma_{\text{external}}$ of Mg, Ca, and Mn exhibit a larger range compared to other elements and Ce* (spanning ~0-5).

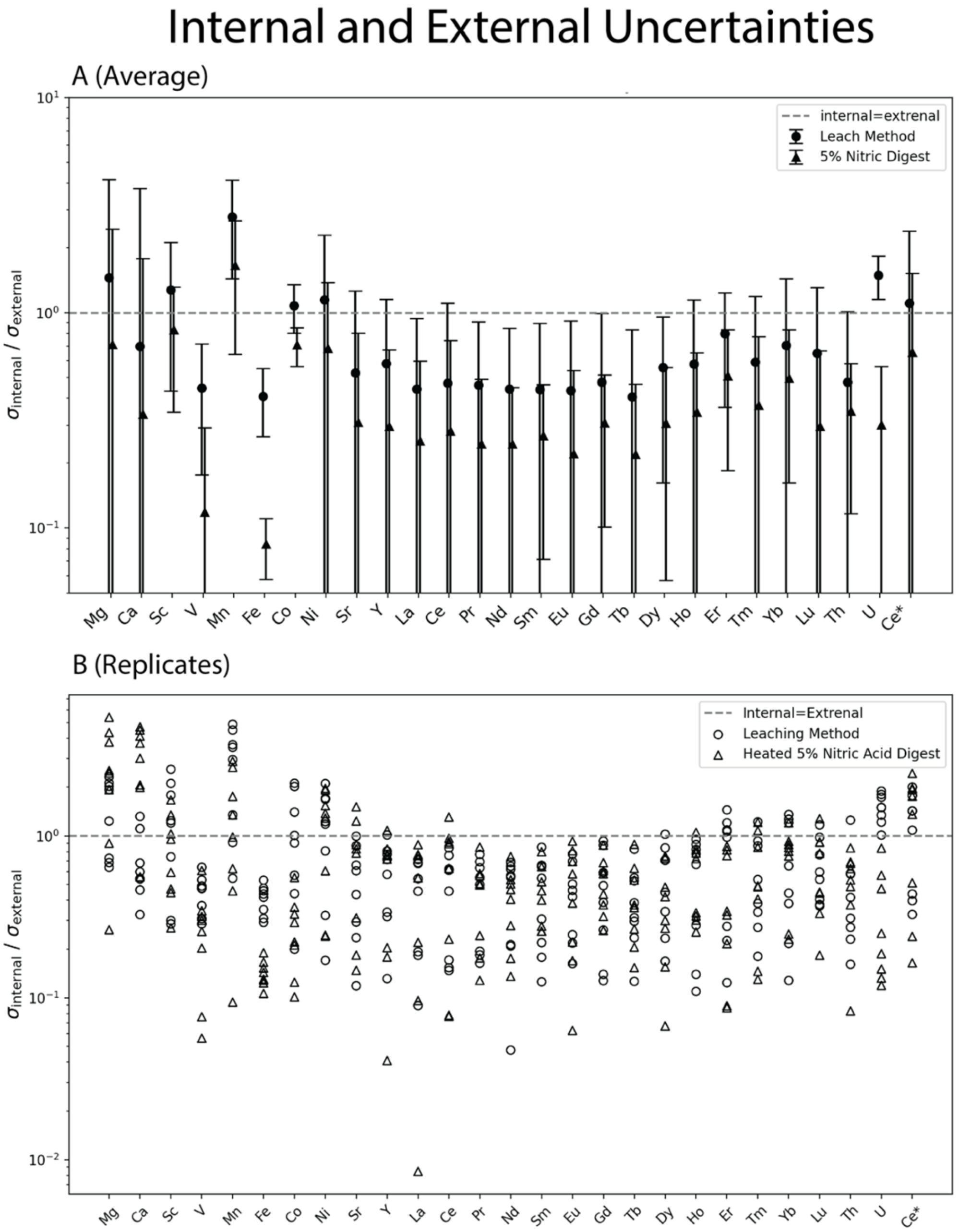

Figure 2.7. The $\sigma_{\text{internal}}/\sigma_{\text{external}}$ ratios plotted by element and Ce* for each aliquot of K-7.6 processed by the leaching method and the heated 5% nitric digestion. Panel A displays the average and standard deviation of $\sigma_{\text{internal}}/\sigma_{\text{external}}$, and Panel B displays the $\sigma_{\text{internal}}/\sigma_{\text{external}}$ of each replicate.

2.4.5 Kunwarara Depth Profile

Major and trace element data for bulk Mg-carbonate and host sediment samples from the depth profile at Kunwarara are reported in full in Tables 2.2-2.4 and Table 2.S3 and are partially summarized in Figure 2.8. We find that the Ce* of the carbonates transitions from <1 to ~1 within the 9.3-10.3 to 10.3-11.3 depth intervals (i.e., between samples K-9.8 and K-10.8) (Figure 2.8B-E). This transition corresponds to about an order of magnitude decrease in redox sensitive element concentrations from paired host-sediments/samples at the transition between sample K-9.8S and K-10.8 (Figure 2.8A). Host sediment sample K-9.8S and those above are rich in interstitial clays between sand grains and Fe/Mn oxide/hydroxide coatings, while K-10.8S has no Fe/Mn oxide/hydroxide coatings and minor clay minerals (Figure 2.9). Ce concentrations in the paired host sediment samples transition from 39±4 ppm to below detection limit (9.1 ppm) with depth when crossing this depth-horizon (Table 2.S3).

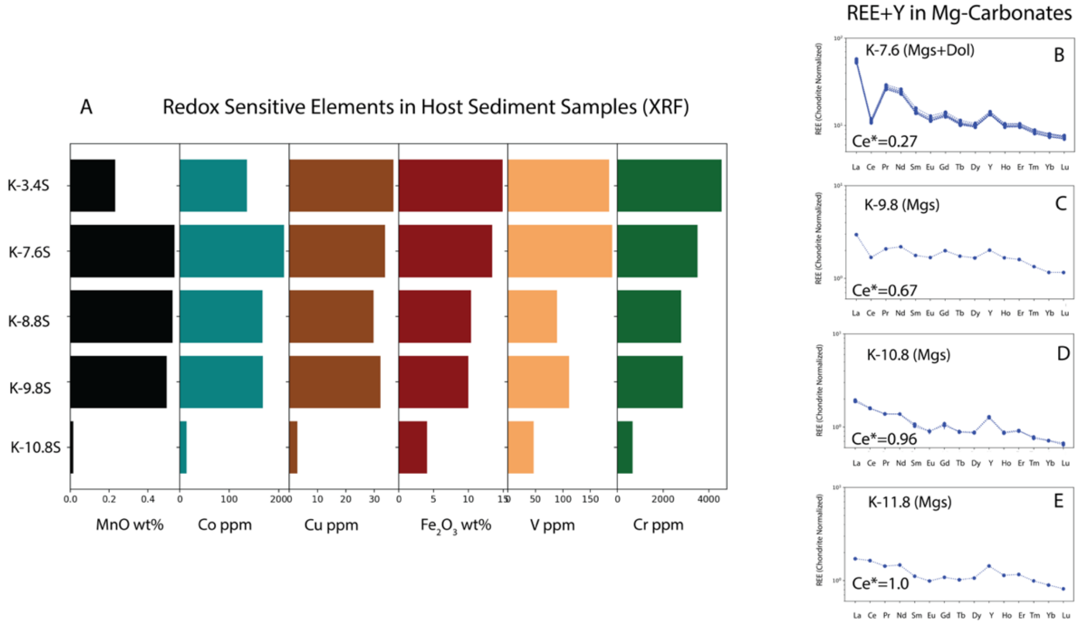

Figure 2.8. A summary of geochemical results associated with the depth transect sampled from the Kunwarara pit mine. Panel A is a plot of the concentrations of redox sensitive elements Mn, Co, Cu, Fe, V, and Cr in the host sediment samples with depth. REE+Y spider diagrams of chondrite normalized (McDonough and Sun, 1995) REE+Y values for carbonate samples K-7.6, K-9.8, K-10.8, and K-11.8 are plotted in Panels B, C, D, and E respectively. All data associated with carbonate samples in this figure are results from the leaching method. Ce* values are reported on each spider diagram. A sharp transition between Ce*<1 and Ce*~1 in the Mg-carbonate is coupled with an order of magnitude drop in the concentrations of redox sensitive elements in the sand samples with depth. This transition occurs between K-9.8S and K-10.8S. Recall that sample K-8.8 was not analyzed due to heterogeneities of the carbonate sample at the hand sample scale, and sample K-11.8S was not analyzed due to finely disseminated carbonate, which was not readily separated from the host sediment by mechanical means (Section 2.3.1).

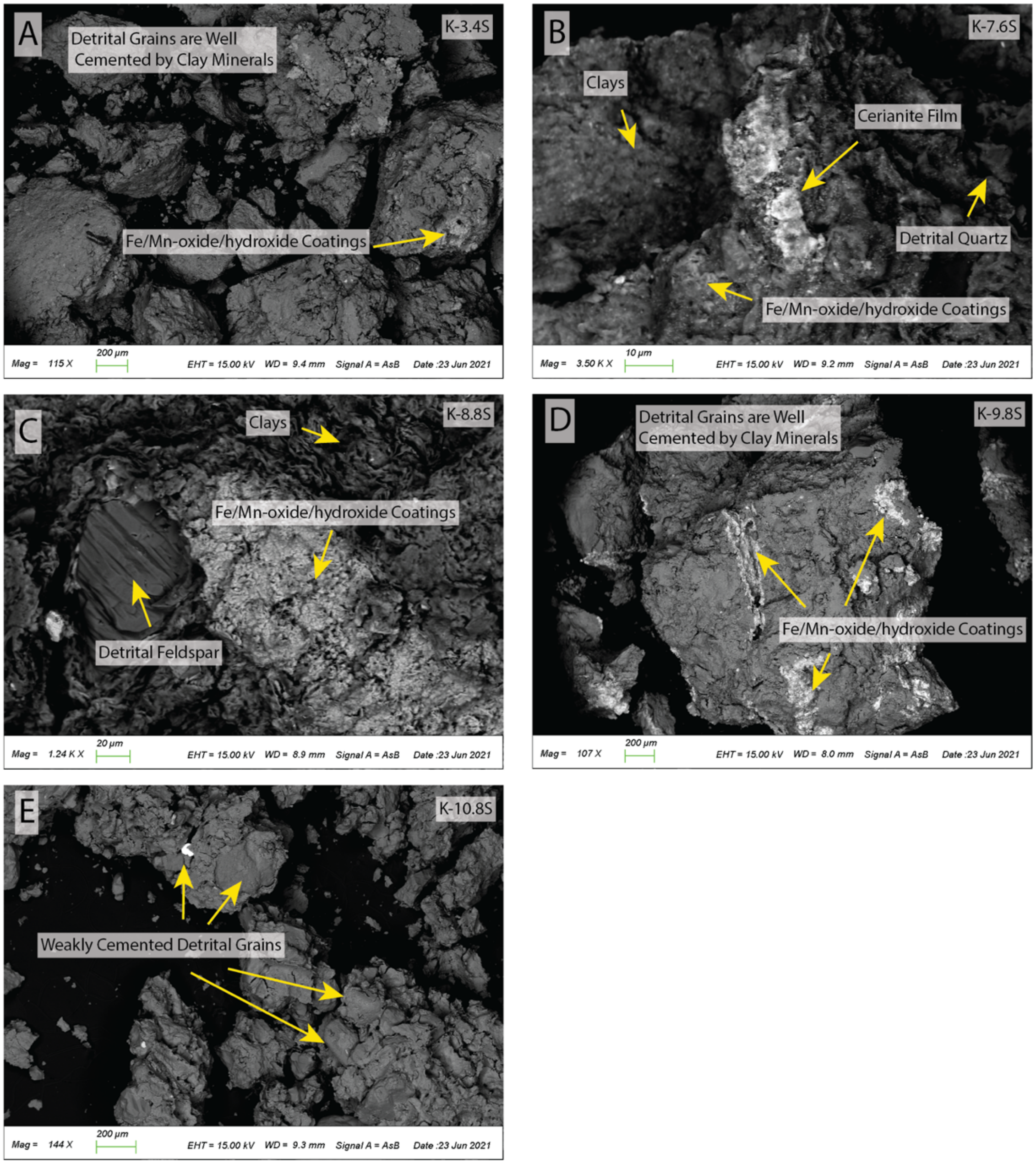

Figure 2.9. SEM images of sand matrix samples along the Kunwarara depth transect. Secondary Fe/Mn/Ce oxide/hydroxide coatings become absent with depth between samples K-9.8S and K-10.8S.

2.5 Discussion

2.5.1 Efficacy of the Leaching Method

The precision, accuracy, low detection limits, and small sample size requirements of our new analytical protocols permit investigating the geological and environmental implications of trace element budgets in Mg-carbonates. Ce* and some redox-sensitive element concentrations derived from samples processed by the leaching method are lower than those that experienced the heated 5% nitric digestion protocol (e.g., sample K-7.6S, Figure 2.3). Good reproducibility (generally consistent with analytical precision of single aliquots) associated with separately analyzing eight aliquots of rock powders derived from sample K-7.6 by the heated 5% nitric-acid digestions and by the leaching protocol rules out inhomogeneity as the cause for the decreases in Ce* and Fe, V, Th, U, Sc, Co, and Ni concentrations (Figure 2.4 and 2.7, Tables 2.2-2.4, Section 2.4.4). The lower elemental concentrations measured with the leaching method results from effectively targeting only the Mg-carbonates with the leaching digestion, minimizing contributions from co-existing Fe/Mn-oxides/hydroxides, silicates, and water-soluble salts. This is particularly important for correctly quantifying Ce* in carbonates because cerium preferentially occurs as Ce^{4+} ions under surface conditions and readily substitutes for Mn^{4+} in the Fe/Mn-oxide/hydroxide structures. Methods that invite the dissolution of Fe/Mn-oxides/hydroxides enriched in Ce will result in anomalous Ce* for the hosting carbonates. In our samples, Ce* and Fe concentrations are consistently elevated when processed by the heated 5% nitric digest as compared to the leaching method (Figure 2.4). In contrast, measured Mn contents are the same between the two methods (Figure 2.4 and 2.5). Micro-XRF maps of K-7.6 show that while Fe and Mn are both present in Fe/Mn-oxides/hydroxides and aluminosilicates in K-

7.6, considerable Mn is hosted in the Mg-carbonate, which is not the case for Fe (Figure 2.10). From this we infer that most of the Mn extracted by the leaching method and the 5% nitric acid digests is hosted by the Mg-carbonate rather than the Fe/Mn-oxides/hydroxides.

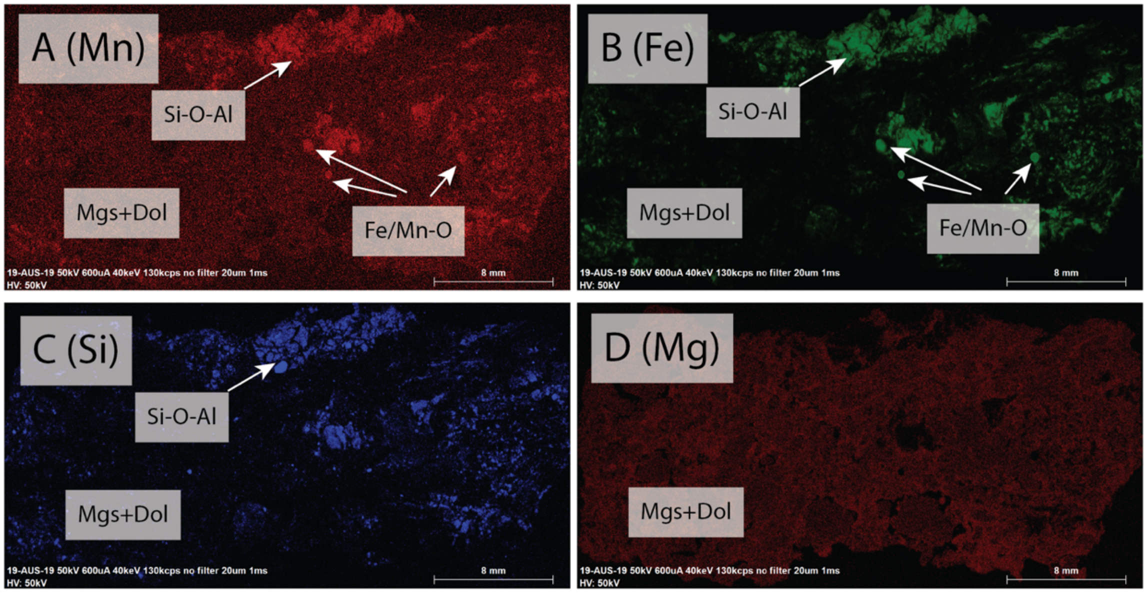

Figure 2.10. Single element micro-XRF maps of a thin section of K-7.6. Maps of Mn, Fe, Si and Mg are in panels A, B, C and D respectively. The brightness of the colors qualitatively indicates the relative presence of an element in each micro-XRF map. Mgs stands for magnesite, Dol stands for dolomite, Fe/Mn-O stands for Fe/Mn-oxides/hydroxides, and Si-O-Al stands for aluminosilicates.

In comparison to the heated 5% nitric digests, measured Fe and V concentrations in sample K-10.8 are lower when processed by the leaching method (Figure 2.5), despite the observed absence of non-carbonate inclusions in this sample (Figure 2.1C and 2.1D). We assert that these decreases in Fe and V concentrations are related to extremely sparsely distributed metal-oxides/hydroxides that are dissolved by the heated 5% nitric digestion but not by the leaching method.

REE concentrations in aliquots of K-7.6 processed by heated 5% nitric digests are slightly elevated compared to the leaching method (Figure 2.4). This is not the case for sample K-

10.8, where REE concentrations determined by both methods are nearly identical (Figure 2.5). The discrepancy in K-7.6 may result from sulfur-bearing phases that are present in trace amounts in K-7.6 but absent in K-10.8. We infer that some REEs from K-7.6 may have precipitated (and were not measured) as sulfates, or possibly fluorides or phosphates, when processed by heated 5% nitric digests due to their low sulfate, fluoride, and phosphate solubilities in acidic conditions compared to carbonate (Han, 2019, 2020). No fluoride or phosphate minerals were observed in K-7.6 or any of the other carbonates. If this discrepancy is the result of a precipitant forming in the aliquots processed in heated nitric acid, the precipitant does not appear to strongly fractionate the REEs. The leaching method we implement should remove water-soluble sulfates (e.g., gypsum) and avoid dissolving sulfides (e.g., pyrite), which would inhibit precipitation of REE-sulphates. Since we do not observe this discrepancy in sample K-10.8, we postulate that REEs from the carbonate are underrepresented in aliquots of K-7.6 that were processed in heated 5% nitric acid compared to those determined by the leaching method. This effect would not be observed in K-10.8 due to the absence of sulfur-bearing phases that are present in K-7.6. This discrepancy could also be explained if a non-carbonate Mg-rich phase (only in sample 7.6) with low REE concentrations was digested by the heated 5% nitric digest, but not by the heated 0.3 M acetic acid digest associated with the leaching method. No such non-carbonate Mg-rich phase exists in K-7.6 in the proportions needed to produce such an offset in the REEs. However, even if this were the case, this non-carbonate Mg-rich phase would need to host the same proportions of Ca, Mn, and Sr as the carbonate with respect to Mg, which is highly improbable. Regardless of its origin, this discrepancy motivates the use of the leaching method over other techniques that risk introducing elements from contaminant phases that can lead to the formation of precipitates or the addition of cations that were not carbonate-associated.

We demonstrate that the leaching method negates the influence of Fe/Mn-oxide/hydroxides, water soluble salts, and silicates when determining trace element concentrations in Mg-carbonates. Data from the heated 5% nitric acid digests confirms that previously implemented digestion protocols using strong acids (Dong *et al.*, 2016; Fernandez-Nieto *et al.*, 2003; Kilias *et al.*, 2006; Kuşcu *et al.*, 2017; Lugli *et al.*, 2000) run the risk of contamination from Fe/Mn-oxide/hydroxides. Previous selective carbonate digestion protocols using weak acids (e.g., Cao *et al.*, 2020) do not dissolve magnesite, but our results show that heated acid digests can produce complete carbonate yields without digesting accessory phases. The leaching protocol utilized here avoids these influences, which are quantifiable in Mg-carbonate samples that are seemingly free of non-carbonate inclusions (e.g., K-10.8). Our results indicate that precise and accurate trace element compositions can be determined from ~2.5-10 mg samples, which enables avoiding samples with visible non-carbonate contaminant phases in most cases.

Application of our method results in the unbiased digestion of both magnesite and dolomite, which may each inherit different trace element characteristics from similar fluids (Fernandez-Nieto *et al.*, 2003; Kilias *et al.*, 2006; Lugli *et al.*, 2000). In cases where mechanical separation is challenging, the development of methods that implement step digestions to separately assess the trace element chemistry of dolomite (or other carbonates) and magnesite would be useful. Such improvements would enable the geochemical interrogation of both magnesite and dolomite separately in complex, porous, cryptocrystalline samples of magnesite intimately associated with dolomite (e.g., K-7.6).

2.5.2 Pedogenic Magnesites Capture Redox Gradients

To show the importance of selectively digesting magnesium carbonate samples in complex matrices, we applied our leaching method to Mg-carbonates hosted in fluvial sediments sampled along a vertical profile within the Kunwarara mine. The results show that the Ce* in magnesite nodules abruptly transitions from <1 to ~1 at a depth of ~10.3 meters below the present surface (Figure 2.8B-E). Importantly, in the same horizon concentrations of redox sensitive elements in paired sand samples drop by about an order of magnitude (Figure 2.8A). This trace element change occurs at depths where the host sediments transition from detrital grains coated with Fe/Mn-oxide/hydroxide films and clays at shallower depths (Figure 2.9A-D) to grains with much lower abundance of clays and devoid of Fe/Mn-oxide/hydroxides deeper in the profile (Figure 2.9E).

We interpret this boundary as an oxidation front where water-soluble Fe^{2+} and Mn^{2+} ions in groundwater at depth precipitate as Fe^{3+}, Mn^{3+} and Mn^{4+} oxyhydroxides above the water table. Ce^{4+} preferentially substitutes Mn^{4+} in Fe/Mn-oxide/hydroxides, while other REEs remain in solution in the trivalent state (Laveuf and Cornu, 2009). The preferential scavenging of Ce^{4+} can also be enhanced by adsorption on Fe-oxide/hydroxides (e.g., Ratié *et al.*, 2023) and surface precipitation of cerianite (e.g., Braun *et al.,* 1990) under oxidizing conditions. Thus, under oxidizing conditions the fluids become depleted in Ce^{4+} and carbonates precipitated from these same oxidizing fluids have Ce*<1. In contrast, when carbonates are precipitated under more reducing conditions, the solutions are enriched in soluble Ce^{3+} and acquire Ce* signatures close to 1. Thus, correctly measuring the REE contents in magnesites becomes a useful marker for the transition of reducing to oxidizing conditions in paleoenvironments.

2.5.3 Implications for Mg-Carbonates on Earth and Mars

As demonstrated above, Mg-carbonates in rocks from Earth or Mars may have complex formation histories, and these carbonates may occur intermingled with non-carbonate phases (e.g., Clavé *et al.*, 2023; Klein *et al.*, 2022), a potential impediment for determining their major and trace element compositions. The method presented here is ideally suited for measuring the elemental composition of magnesite while removing uncertainties associated with the presence of contaminating phases, providing the targeted approach needed for properly constraining environmental conditions controlling the precipitation of Mg-carbonates on Earth and Mars.

The analysis of samples acquired along a depth profile at the Kunwarara mine demonstrate that Ce* in magnesite is a potential tracer of changes from reducing to oxidizing conditions in the geological past. It also permits determining if magnesite precipitation is coeval with or postdates Fe/Mn-oxide/hydroxide precipitation in the transition from reducing to oxidizing environments. As demonstrated here, our approach is ideally suited for extracting correct information from the carbonates themselves, avoiding the potential pitfalls associated with the coexistence of minerals of distinct origins that are today jointly hosted in surficial deposits.

For example, on Earth Mg-carbonates can result from both deep metasomatic processes or precipitation in aqueous environments under surface conditions (e.g., Braithwaite and Zedef, 1994; Zhang and Liou, 1994). Determining redox conditions, if coupled with clumped isotope thermometry of Mg-carbonates (e.g., García Del Real *et al.*, 2016), could place relevant constraints on fluid composition, pH-Eh conditions, and sources. Reported Ce* in hydrothermal and diagenetic magnesites on Earth are variable and have been used to argue for diagenetic overprinting and the existence of oxidizing fluids as early as the Archean (Dong *et al.*, 2016; Toulkeridis *et al.*, 2010).

Our approach would permit identification of changes in Mg-carbonate trace element geochemistry during weathering that could significantly alter the composition of carbonates that may have formed from deep metasomatic processes under conditions very distinct from those prevailing in the surficial environment today (e.g., Dzemua *et al.*, 2011). This could be accomplished by verifying trace element fractionation between Mg-carbonates that have recrystallized during chemical weathering and phases that precipitate as weathering products in surficial environments.

Our results demonstrate that the effective use of Ce* as a redox tracer in magnesite-forming processes requires differentiating the trace element budget of magnesite itself from that of co-existing contaminants near Earth's surface. This mineral-specific approach is needed to interrogate the paleohydrology of Mg-carbonate forming fluids.

Similarly, the Ce* of Martian magnesites and the possible co-existence of Mg-carbonates with Fe/Mn-oxyhydroxides on Mars could help place constraints on pH-Eh conditions under which these carbonates formed. As both Mg-carbonates and Fe/Mn-oxide/hydroxides have been positively identified on the surface of Mars and in Martian meteorites (e.g., Ehlmann *et al.*, 2008; Eiler *et al.*, 2002; Farley *et al.*, 2022, 2022; Gattacceca *et al.*, 2014; Lanza *et al.*, 2016; Y. Liu *et al.*, 2021, 2022; Wendt *et al.*, 2011), their trace element contents are directly relevant for unravelling key environmental aspects of Martian evolution. For example, the presence of secondary Fe/Mn-oxides/hydroxides in altered igneous and sedimentary rocks on Mars provides evidence for the existence of both surficial water and an oxidizing Martian atmosphere during the Noachian and the Hesperian (Lanza *et al.*, 2016; Y. Liu *et al.*, 2021;

Wendt *et al.*, 2011). While it is uncertain whether this high redox potential resulted from high atmospheric O_2 or halogen cycling in the early Martian atmosphere, Martian Fe/Mn-oxides/hydroxides likely formed in an aqueous environment exposed to the ancient Martian surface (Lanza *et al.*, 2016; Y. Liu *et al.*, 2021; Mitra *et al.*, 2023). But the possible coexistence of Fe/Mn-oxides/hydroxides and Mg-carbonates on the Martian surface would not necessarily indicate coeval formation, as these phases may have formed independently millions or billions of years apart. Thus, as on Earth, Mg-carbonates on Mars may have resulted from a combination of deep metasomatic processes, surficial aqueous alteration, or evaporative mineralization in a lacustrine environment (Corpolongo *et al.*, 2023; Eiler *et al.*, 2002; Farley *et al.*, 2022; Horgan *et al.*, 2020; Scheller *et al.*, 2022; Simon *et al.*, 2023).

Ce anomaly values calculated for Mg-carbonates with <0.10 mole fraction $CaCO_3$ from Martian meteorite ALH84001, where La, Ce, and Nd concentrations were determined by SIMS (Eiler *et al.,* 2002), vary from 0.45 to 1.01 (Table 2.6). The range of Ce anomalies indicates that some oxidative scavenging of Ce with respect to other REEs occurred during Mg-carbonate formation on Mars. This implies that Ce* in Martian Mg-carbonates may have captured redox conditions prevailing on Mars billions of years ago. If the ancient Martian atmosphere was less oxidizing than currently assumed, low Ce* may not have developed in surficial carbonates. Alternatively, if carbonation of Martian samples resulted from metasomatic alteration via a deeply sourced reducing fluid, the Mg-carbonates could be far removed from the ancient surficial hydrology. Therefore, following sample return from the Mars 2020 Mission, detailed analyses of Ce* of Martian carbonates separately from coexisting phases could shed light on the influence of redox reactions on diagenetic and pedogenic carbonate formation on the ancient Martian surface. The approach illustrated here would be needed to properly constrain the compositions of the carbonates separately from that of potentially coexisting contaminating minerals such as Mn-oxides.

Table 2.6. $CaCO_3$ and REE data for Mg-rich carbonates from Martian meteorite ALH84001 reported by Eiler *et al.* (2002). While $MgCO_3$, $FeCO_3$, and $MnCO_3$ contents associated with these analyses are not reported, for $CaCO_3$ mole fractions below 0.10 in ALH84001 carbonates, $MgCO_3$, $FeCO_3$, and $MnCO_3$ mole fractions for span 0.56-0.90, 0.08-0.33, and <0.01 respectively (Eiler *et al.*, 2002). Data with a CI subscripts are concentrations normalized to chondrite REE values reported by McDonough and Sun (1995). Ce^*_3 values were calculated using chondrite normalized REEs (La_{CI}, Ce_{CI}, and Nd_{CI}) instead of shale normalized REEs in Equation 3 in Barrat *et al.* (2023). The "3" subscript in Ce^*_3 is used to indicate that the Ce^*_3 Ce anomaly was calculated differently than Ce* due to the absence of Pr concentrations in Eiler *et al.* (2002).

$CaCO_3$ (Mole Fraction)	La (ppm)	Ce (ppm)	Nd (ppm)	La_{CI}	Ce_{CI}	Nd_{CI}	Ce^*_3
0.04	0.67	1.54	1.75	2.8	2.51	3.83	0.80
0.05	0.21	0.48	0.41	0.89	0.78	0.90	0.87
0.05	0.41	0.91	0.71	1.7	1.5	1.6	0.90
0.06	1.31	3.20	2.77	5.53	5.22	6.06	0.915
0.07	1.64	4.10	3.15	6.92	6.69	6.89	0.968
0.08	0.87	2.11	1.30	3.67	3.44	2.84	1.01
0.09	0.23	0.53	0.63	0.97	0.86	1.4	0.77
0.09	0.25	0.37	0.81	1.1	0.6	1.8	0.45
0.10	0.39	0.72	0.76	1.6	1.2	1.7	0.73
0.10	0.28	0.49	0.67	1.2	0.80	1.5	0.62
0.12	0.25	0.6	0.44	1.1	0.98	0.96	0.93
0.14	0.27	0.49	0.59	1.1	0.80	1.3	0.69
0.15	0.59	1.71	1.03	2.5	2.79	2.25	1.2
0.22	1.34	3.19	2.65	5.65	5.20	5.80	0.912
0.23	0.98	2.22	1.72	4.1	3.62	3.76	0.91
0.25	0.98	2.32	1.34	4.1	3.78	2.93	1.0
0.44	0.91	1.89	1.45	3.8	3.08	3.17	0.86
0.45	1.33	2.69	1.98	5.61	4.39	4.33	0.847
0.50	0.55	0.89	0.97	2.3	1.5	2.1	0.67
0.54	1.52	2.78	2.33	6.41	4.54	5.1	0.76

2.6 **Conclusion**

A leaching method for trace element characterization in Mg-carbonates by solution ICP-MS was developed. The efficacy of this method was demonstrated by comparing trace element determinations from the new method to those determined by processing the same samples by a heated 5% nitric digest. The comparison confirms that the leaching method reports lower Ce* and lower concentrations of redox sensitive elements sourced from contaminant oxide/hydroxide phases. We applied this new method to magnesite±dolomite samples from a depth profile in the Kunwarara magnesite mine. Low Ce* in the carbonates vanishes with depth, coinciding with an order of magnitude drop in redox sensitive elements in paired sand samples and the sudden absence of secondary Fe/Mn-oxide/hydroxide coatings. Results demonstrate that magnesite samples hosted in fluvial sediments can capture redox gradients associated with Fe/Mn-oxide/hydroxide formation and thus place constraints on palaeohydrological conditions near Earth's surface (pH-Eh). This also implies that Mg-carbonates that formed near the Martian surface may capture redox conditions associated with carbonate formation.

Appendix 2.A. Supplementary Material

Table 2.S1. Results from matrix matching experiments to test the effect of mismatching the Mg concentration of the matrix with 5 ppb Cd, Co, Cr, Cu, Fe, Mn, Ni, V, and Zn, 0.5 ppb of REEs, Sc, Y, U, and Th, 0.01 ppb Mo, 50 ppb Sr, and 500 ppb Ca. The 50% Mg solution contains 14,200 ppb Mg (2.5 mg magnesite / 50 mL). The 100% Mg solution contains 28,400 ppb Mg, which is the normal amount of matrix expected for 5 mg of sample (5.0 mg magnesite / 50 mL). The 150% Mg solution contained 42,600 ppb Mg, which is 50% more Mg than the normal amount of matrix (7.5 mg magnesite / 50 mL). The 200% Mg solution contained 56,800 ppb Mg, which is twice the normal amount of Mg used for matrix matching (10.0 mg magnesite / 50 mL). Values reported in the table are the amount of each element in the 50% Mg, the 150% Mg and the 200% Mg solutions reported as percentages of the same element in measured in the 100% Mg solution. Reported uncertainties are 1σ.

Element	50% / 100% Mg	150% / 100% Mg	200% / 100% Mg
Ca	97±22	92±17	105±13
Sc	100±7	105±7	104±6
V	98±3	103±3	103±3
Cr	98±3	104±3	105±3
Mn	99±3	102±3	103±3
Fe	97±3	94±3	92±2
Co	100±3	102±2	103±2
Ni	102±3	102±4	100±3
Cu	99±2	102±3	103±1
Zn	101±2	103±3	103±3
Sr	101±3	103±2	103±2
Y	100±3	102±2	102±2
Mo	94±5	93±5	96±6
Cd	101±2	103±2	100±3
La	101±2	101±2	100±2
Ce	101±2	101±2	100±2
Pr	101±2	101±2	100±2
Nd	100±3	100±1	100±1
Sm	101±3	101±2	100±2
Eu	100±3	101±1	100±1
Gd	99±3	100±3	99±3
Tb	99±3	100±2	99±2
Dy	100±3	100±2	99±2
Ho	99±3	99±2	98±2
Er	98±2	99±2	98±2
Tm	99±2	99±1	98±1

Element	50% / 100% Mg	150% / 100% Mg	200% / 100% Mg
Yb	99±3	98±1	97±1
Lu	98±3	98.0±0.4	97±1
Th	97±3	96±2	94±2
U	98±3	95±2	93±1

Table 2.S2. Elemental masses and 1σ uncertainties on the last decimal place (in parentheses) of procedural blank analyses associated with the heated 5% nitric digest (nitric) and the leaching method (leach) over multiple batches (different dates). Masses are in nanograms (ng) of the given element. BDL indicates that the procedural blank was below the detection limit of the instrument.

Date	6/24/22	6/24/22	7/1/22	8/12/22	9/15/22	9/15/22	9/30/22	10/10/22
Analysis	Leach	5% Nitric	Leach	Leach	Leach	5% Nitric	Leach	Leach
Replicates	3	3	4	4	4	4	3	3
Mg ng	570(390)	2570(880)	13(14)	78(54)	110(150)	230(180)	91(24)	340(180)
Ca ng	90(130)	290(110)	240(150)	470(310)	240(410)	240(150)	280(150)	150(120)
Sc ng	0.08(12)	0.08(11)	0.15(10)	BDL	BDL	BDL	0.153(39)	BDL
V ng	0.103(29)	0.221(55)	0.8(13)	0.052(34)	0.15(87)	0.132(42)	0.056(64)	0.206(94)
Cr ng	5.0(39)	1.1(12)	2.8(28)	0.9(14)	3.1(44)	0.9(16)	0.007(10)	6.1(52)
Mn ng	2.7(10)	2.03(54)	1.8(15)	1.1(11)	3.0(14)	1.5(11)	2.5(21)	0.82(59)
Fe ng	162(18)	32.7(46)	34(19)	30(11)	93(44)	223(76)	BDL	44.6(94)
Co ng	0.11(13)	0.089(93)	0.035(45)	BDL	0.103(75)	0.281(91)	0.061(53)	0.103(80)
Ni ng	18(24)	2.1(15)	BDL	2.0(27)	1.64(94)	3.7(18)	2.4(12)	2.2(15)
Cu ng	5.6(48)	3.1(20)	6.5(43)	2.39(12)	2.9(86)	10.3(28)	6.8(42)	6.8(44)
Zn ng	93(19)	121(32)	5.1(70)	52(12)	63.9(77)	110(11)	65.3(67)	31(29)
Sr ng	0.733(84)	1.24(54)	0.26(15)	0.59(27)	0.7(24)	1.11(24)	0.831(41)	0.972(56)
Y ng	0.025(10)	0.05(21)	0.0014(19)	0.0088(19)	0.022(16)	0.033(17)	0.0511(37)	0.093(12)
Mo ng	0.053(11)	0.0495(83)	0.042(38)	0.044(11)	0.09(66)	0.094(17)	0.12(13)	0.1144(54)
Cd ng	0.053(38)	0.023(22)	BDL	0.037(22)	0.053(22)	0.022(29)	0.046(53)	0.027(20)
La ng	0.03(13)	0.0248(75)	0.01(67)	0.02(15)	0.027(20)	0.05(13)	0.062(91)	0.098(16)
Ce ng	0.0331(46)	0.065(20)	0.0066(49)	0.041(30)	0.034(28)	0.087(18)	0.1049(93)	0.175(13)
Pr ng	0.0021(15)	0.003(18)	0.0011(15)	0.0033(39)	0.0061(52)	0.0171(54)	0.0141(62)	0.0241(14)
Nd ng	0.0173(26)	0.026(10)	0.0031(36)	0.0131(82)	0.019(15)	0.052(16)	0.056(10)	0.1022(58)
Sm ng	0.0053(26)	0.0042(16)	0.00044(62)	0.0029(14)	0.0024(33)	0.0036(24)	0.0117(18)	0.0252(23)
Eu ng	0.0022(26)	0.005(20)	0.0049(52)	0.0007(12)	0.0014(17)	0.0021(11)	0.00146(25)	0.00478(96)
Gd ng	0.017(22)	0.017(12)	0.06(52)	0.014(15)	0.01183(70)	0.014(78)	0.019(14)	0.0492(70)

Date	6/24/22	6/24/22	7/1/22	8/12/22	9/15/22	9/15/22	9/30/22	10/10/22
Analysis	Leach	5% Nitric	Leach	Leach	Leach	5% Nitric	Leach	Leach
Replicates	3	3	4	4	4	4	3	3
Tb ng	0.0013(12)	0.00057(66)	0.00019(33)	0.00059(43)	0.0013(13)	0.00153(71)	0.00193(23)	0.00255(90)
Dy ng	0.0035(25)	0.0072(28)	0.00023(40)	0.0014(11)	0.0043(34)	0.0064(22)	0.0097(13)	0.0195(16)
Ho ng	0.0013(10)	0.00093(10)	BDL	0.00025(43)	0.0012(14)	0.00111(80)	0.00088(19)	0.00239(62)
Er ng	0.0016(11)	0.0023(16)	0.000086(95)	0.0006(74)	0.0023(24)	0.0025(18)	0.09(12)	0.09(12)
Tm ng	0.00059(80)	0.00023(33)	0.000038(67)	0.00023(39)	0.0009(13)	0.00078(91)	0.000115(94)	0.00059(26)
Yb ng	0.0023(17)	0.00332(70)	BDL	0.00023(40)	0.0039(25)	0.004(10)	0.0047(11)	0.0083(20)
Lu ng	0.00062(82)	0.000134(95)	BDL	0.00023(16)	0.0008(11)	0.00031(54)	0.00054(39)	0.00033(46)
Th ng	BDL	BDL	BDL	BDL	BDL	BDL	BDL	BDL
U ng	0.0076(28)	0.015(10)	0.00163(85)	0.00421(67)	0.013(16)	0.0079(10)	0.0066(20)	0.0185(22)

Table 2.S3. Results from XRF analyses of host sediment samples from the depth profile at Kunwarara. Counting statistics uncertainties (1σ) on the last reported decimal place of concentrations are reported in parentheses. The lower limits of detection (LLD) associated with each analysis are reported in the columns to the right of each corresponding sample name. Loss on ignition (LOI), which acts as an estimation of structural water, was determined by weighing samples that were dried at 110°C for ~24 hours (to remove adsorbed water) before and after baking at 1050°C.

	Units	K-3.4S	LLD	K-7.6S	LLD	K-8.8S	LLD	K-9.8S	LLD	K-10.8S	LLD
SiO_2	wt.%	58.71(2)	0.0026	55.89(2)	0.0025	58.78(2)	0.0025	59.08(2)	0.0026	80.85(2)	0.0027
TiO_2	wt.%	1.460(2)	0.00097	1.409(2)	0.00097	0.996(1)	0.00096	0.981(1)	0.00097	0.547(1)	0.00094
Al_2O_3	wt.%	9.779(6)	0.0015	10.881(7)	0.0015	9.400(6)	0.0015	9.369(6)	0.0014	5.200(5)	0.0013
Fe_2O_3	wt.%	14.921(4)	0.00072	13.398(4)	0.00073	10.394(3)	0.0007	10.025(3)	0.0007	4.077(2)	0.00065
MgO	wt.%	3.591(7)	0.0044	4.441(7)	0.0044	7.407(9)	0.0043	8.008(9)	0.0043	2.722(6)	0.0039
CaO	wt.%	0.1424(7)	0.00057	0.951(1)	0.00058	0.2409(7)	0.00057	0.6537(9)	0.00058	0.2471(7)	0.00058
Na_2O	wt.%	0.171(3)	0.0038	0.121(3)	0.0038	0.268(3)	0.0039	0.650(4)	0.004	0.273(3)	0.0036
K_2O	wt.%	0.0156(5)	0.00048	0.0054(5)	0.00049	0.0218(5)	0.00048	0.1337(6)	0.00048	0.3614(7)	0.00047
P_2O_5	wt.%	0.0138(4)	0.00048	0.01806(4)	0.00048	0.0100(4)	0.00046	0.0157(4)	0.00047	0.0097(4)	0.00049
MnO	wt.%	0.2320(2)	0.00029	0.5372(3)	0.00028	0.5271(3)	0.00027	0.4972(3)	0.00027	0.0147(1)	0.00024
LOI	wt.%	7.87		9.42		8.79		7.56		3.02	
Rb	ppm	<d.l.	0.99	<d.l.	0.98	<d.l.	0.95	2.7(4)	0.95	15.0(4)	0.89
Ba	ppm	115(4)	8.6	491(4)	8.7	337(4)	8.6	874(4)	8.6	118(4)	8.5
Sr	ppm	42.8(5)	0.86	58.9(5)	0.85	49.5(4)	0.82	102.4(5)	0.82	53.2(4)	0.77
Nb	ppm	17.4(5)	0.88	15.6(5)	0.88	10.8(4)	0.85	13.4(4)	0.85	6.8(4)	0.79
Zr	ppm	252.7(5)	0.73	250.8(5)	0.73	141.8(4)	0.7	150.9(4)	0.7	245.8(4)	0.65
Hf	ppm	5.5(4)	1.2	4.6(4)	1.2	2.8(4)	1.1	3.1(4)	1.1	7.3(4)	1

	Units	K-3.4S	LLD	K-7.6S	LLD	K-8.8S	LLD	K-9.8S	LLD	K-10.8S	LLD
Y	ppm	24.6(5)	1.3	16.6(5)	1.3	6.2(5)	1.2	22.0(5)	1.2	11.8(4)	1.1
Zn	ppm	84.3(4)	0.99	77.2(4)	0.98	90.6(4)	0.95	91.8(4)	0.95	35.8(4)	0.88
Cu	ppm	36(1)	1.6	34(1)	1.5	30(1)	1.5	32(1)	1.5	3(1)	1.4
Ni	ppm	2489(1)	1.3	2475(1)	1.3	2853(1)	1.2	2123(1)	1.2	459.5(8)	1.1
Co	ppm	136(2)	1.6	210.4(9)	1.6	167.0(8)	1.6	167.9(8)	1.6	14.1(7)	1.5
Cr	ppm	4551(3)	1.9	3502(3)	1.9	2789(2)	1.9	2864(2)	1.9	670(2)	1.9
V	ppm	184(3)	1.7	190(3)	1.7	89(3)	1.7	111(3)	1.7	47(3)	1.7
La	ppm	13(3)	7	7(3)	7	13(3)	6.9	41(3)	7	17(3)	6.9
Ce	ppm	25(4)	9.3	77(4)	9.3	68(4)	9.2	39(4)	9.2	<d.l.	9.1
Nd	ppm	23(3)	2.1	33(3)	2.1	29(3)	2.1	26(3)	2.1	13(3)	2
Pb	ppm	2.1(6)	1.7	13.3(6)	1.7	10.2(6)	1.6	12.2(6)	1.6	2.5(5)	1.5
Th	ppm	4.6(8)	2.2	4.9(8)	2.2	<d.l.	2.1	<d.l.	2.1	6.1(7)	2

Chapter Two References

Barrat, J.-A., Bayon, G., & Lalonde, S. (2023). Calculation of cerium and lanthanum anomalies in geological and environmental samples. *Chemical Geology*, *615*, 121202. https://doi.org/10.1016/j.chemgeo.2022.121202

Boyle, E. A. (1981). Cadmium, zinc, copper, and barium in foraminifera tests. *Earth and Planetary Science Letters*, *53*(1), 11–35. https://doi.org/10.1016/0012-821X(81)90022-4

Braithwaite, C. J. R., & Zedef, V. (1994). Living hydromagnesite stromatolites from Turkey. *Sedimentary Geology*, *92*(1–2), 1–5. https://doi.org/10.1016/0037-0738(94)90051-5

Braun, J.-J., Pagel, M., Muller, J.-P., Bilong, P., Michard, A., & Guillet, B. (1990). Cerium anomalies in lateritic profiles. *Geochimica et Cosmochimica Acta*, *54*(3), 781–795. https://doi.org/10.1016/0016-7037(90)90373-S

Brown, A. J., Viviano, C. E., & Goudge, T. A. (2020). Olivine-Carbonate Mineralogy of the Jezero Crater Region. *Journal of Geophysical Research: Planets*, *125*(3). https://doi.org/10.1029/2019JE006011

Bucholz, C. E., & Spencer, C. J. (2019). Corrigendum to: ‘Strongly Peraluminous Granites across the Archean–Proterozoic Transition.’ *Journal of Petrology*, *60*(9), 1851–1851. https://doi.org/10.1093/petrology/egz049

Cao, C., Liu, X.-M., Bataille, C. P., & Liu, C. (2020). What do Ce anomalies in marine carbonates really mean? A perspective from leaching experiments. *Chemical Geology*, *532*, 119413. https://doi.org/10.1016/j.chemgeo.2019.119413

Clavé, E., Benzerara, K., Meslin, P. -Y., Forni, O., Royer, C., Mandon, L., Beck, P., Quantin-Nataf, C., Beyssac, O., Cousin, A., Bousquet, B., Wiens, R. C., Maurice, S., Dehouck, E., Schröder, S., Gasnault, O., Mangold, N., Dromart, G., Bosak, T., … the SuperCam team. (2023). Carbonate Detection With SuperCam in Igneous Rocks on the Floor of Jezero Crater, Mars. *Journal of Geophysical Research: Planets*, *128*(6), e2022JE007463. https://doi.org/10.1029/2022JE007463

Corpolongo, A., Jakubek, R. S., Burton, A. S., Brown, A. J., Yanchilina, A., Czaja, A. D., Steele, A., Wogsland, B. V., Lee, C., Flannery, D., Baker, D., Cloutis, E. A., Cardarelli, E., Scheller, E. L., Berger, E. L., McCubbin, F. M., Hollis, J. R., Hickman-Lewis, K., Steadman, K., … Abbey, W. (2023). SHERLOC Raman Mineral Class Detections of the Mars 2020 Crater Floor Campaign. *Journal of Geophysical Research: Planets*, *128*(3), e2022JE007455. https://doi.org/10.1029/2022JE007455

Dong, A., Zhu, X.-K., Li, S.-Z., Kendall, B., Wang, Y., & Gao, Z. (2016). Genesis of a giant Paleoproterozoic strata-bound magnesite deposit: Constraints from Mg isotopes. *Precambrian Research*, *281*, 673–683. https://doi.org/10.1016/j.precamres.2016.06.020

Dzemua, G. L., Mees, F., Stoops, G., & Van Ranst, E. (2011). Micromorphology, mineralogy and geochemistry of lateritic weathering over serpentinite in south-east Cameroon. *Journal of African Earth Sciences*, *60*(1–2), 38–48. https://doi.org/10.1016/j.jafrearsci.2011.01.011

Edward D. Pittman (2). (1971). Microporosity in Carbonate Rocks: GEOLOGICAL NOTES. *AAPG Bulletin*, *55*. https://doi.org/10.1306/819A3DB2-16C5-11D7-8645000102C1865D

Ehlmann, B. L., Mustard, J. F., Murchie, S. L., Poulet, F., Bishop, J. L., Brown, A. J., Calvin, W. M., Clark, R. N., Marais, D. J. D., Milliken, R. E., Roach, L. H., Roush, T. L., Swayze, G. A., & Wray, J. J. (2008). Orbital Identification of Carbonate-Bearing Rocks on Mars. *Science*, *322*(5909), 1828–1832. https://doi.org/10.1126/science.1164759

Eiler, J. M., Valley, J. W., Graham, C. M., & Fournelle, J. (2002). Two populations of carbonate in ALH84001: Geochemical evidence for discrimination and genesis. *Geochimica et Cosmochimica Acta*, *66*(7), 1285–1303. https://doi.org/10.1016/S0016-7037(01)00847-X

Farley, K. A., Stack, K. M., Shuster, D. L., Horgan, B. H. N., Hurowitz, J. A., Tarnas, J. D., Simon, J. I., Sun, V. Z., Scheller, E. L., Moore, K. R., McLennan, S. M., Vasconcelos, P. M., Wiens, R. C., Treiman, A. H., Mayhew, L. E., Beyssac, O., Kizovski, T. V., Tosca, N. J., Williford, K. H., … Zorzano, M.-P. (2022). Aqueously altered igneous rocks sampled on the floor of Jezero crater, Mars. *Science*, *377*(6614), eabo2196. https://doi.org/10.1126/science.abo2196

Fernandez-Nieto, C., Torres-Ruiz, J., Subias Perez, I., Fanlo Gonzalez, I., & Gonzalez Lopez, J. M. (2003). Genesis of Mg-Fe Carbonates from the Sierra Menera Magnesite-Siderite Deposits, Northeast Spain: Evidence from Fluid Inclusions, Trace Elements, Rare Earth Elements, and Stable Isotope Data. *Economic Geology*, *98*(7), 1413–1426. https://doi.org/10.2113/gsecongeo.98.7.1413

García Del Real, P., Maher, K., Kluge, T., Bird, D. K., Brown, G. E., & John, C. M. (2016). Clumped-isotope thermometry of magnesium carbonates in ultramafic rocks. *Geochimica et Cosmochimica Acta*, *193*, 222–250. https://doi.org/10.1016/j.gca.2016.08.003

Gattacceca, J., Rochette, P., Scorzelli, R. B., Munayco, P., Agee, C., Quesnel, Y., Cournède, C., & Geissman, J. (2014). Martian meteorites and Martian magnetic anomalies: A new perspective from NWA 7034: Martian meteorites & magnetic anomalies. *Geophysical Research Letters*, *41*(14), 4859–4864. https://doi.org/10.1002/2014GL060464

Han, K. N. (2019). Effect of Anions on the Solubility of Rare Earth Element-Bearing Minerals in Acids. *Mining, Metallurgy & Exploration*, *36*(1), 215–225. https://doi.org/10.1007/s42461-018-0029-3

Han, K. N. (2020). Characteristics of Precipitation of Rare Earth Elements with Various Precipitants. *Minerals*, *10*(2), 178. https://doi.org/10.3390/min10020178

Henjes-Kunst, F., Prochaska, W., Niedermayr, A., Sullivan, N., & Baxter, E. (2014). Sm–Nd dating of hydrothermal carbonate formation: An example from the Breitenau magnesite deposit (Styria, Austria). *Chemical Geology*, *387*, 184–201. https://doi.org/10.1016/j.chemgeo.2014.07.025

Horgan, B. H. N., Anderson, R. B., Dromart, G., Amador, E. S., & Rice, M. S. (2020). The mineral diversity of Jezero crater: Evidence for possible lacustrine carbonates on Mars. *Icarus*, *339*, 113526. https://doi.org/10.1016/j.icarus.2019.113526

Kakkassery, A. I., Haritha, A., & Rajesh, V. J. (2022). Serpentine-magnesite Association of Salem Ultramafic Complex, Southern India: A Potential Analogue for Mars. *Planetary and Space Science*, *221*, 105528. https://doi.org/10.1016/j.pss.2022.105528

Kelemen, P. B., & Matter, J. (2008). In situ carbonation of peridotite for CO $_2$ storage. *Proceedings of the National Academy of Sciences*, *105*(45), 17295–17300. https://doi.org/10.1073/pnas.0805794105

Kelemen, P. B., Matter, J., Streit, E. E., Rudge, J. F., Curry, W. B., & Blusztajn, J. (2011). Rates and Mechanisms of Mineral Carbonation in Peridotite: Natural Processes and Recipes for Enhanced, in situ CO $_2$ Capture and Storage. *Annual Review of Earth and Planetary Sciences*, *39*(1), 545–576. https://doi.org/10.1146/annurev-earth-092010-152509

Kilias, S. P., Pozo, M., Bustillo, M., Stamatakis, M. G., & Calvo, J. P. (2006). Origin of the Rubian carbonate-hosted magnesite deposit, Galicia, NW Spain: Mineralogical, REE, fluid inclusion and isotope evidence. *Mineralium Deposita*, *41*(7), 713–733. https://doi.org/10.1007/s00126-006-0075-5

Klein, F., Goldsby, D. L., Lin, J., & Andreani, M. (2022). Carbonation of Serpentinite in Creeping Faults of California. *Geophysical Research Letters*, *49*(15). https://doi.org/10.1029/2022GL099185

Kuşcu, M., Cengiz, O., & Kahya, A. (2017). Trace element contents and C-O isotope geochemistry of the different originated magnesite deposits in Lake District

(Southwestern Anatolia), Turkey. *Arabian Journal of Geosciences*, *10*(15), 339. https://doi.org/10.1007/s12517-017-3102-1

Lanza, N. L., Wiens, R. C., Arvidson, R. E., Clark, B. C., Fischer, W. W., Gellert, R., Grotzinger, J. P., Hurowitz, J. A., McLennan, S. M., Morris, R. V., Rice, M. S., Bell, J. F., Berger, J. A., Blaney, D. L., Bridges, N. T., Calef, F., Campbell, J. L., Clegg, S. M., Cousin, A., … Zorzano, M.-P. (2016). Oxidation of manganese in an ancient aquifer, Kimberley formation, Gale crater, Mars: Manganese Fracture Fills in Gale Crater. *Geophysical Research Letters*, *43*(14), 7398–7407. https://doi.org/10.1002/2016GL069109

Laveuf, C., & Cornu, S. (2009). A review on the potentiality of Rare Earth Elements to trace pedogenetic processes. *Geoderma*, *154*(1–2), 1–12. https://doi.org/10.1016/j.geoderma.2009.10.002

Leask, E. K., Ehlmann, B. L., Greenberger, R. N., Pinet, P., Daydou, Y., Ceuleneer, G., & Kelemen, P. (2021). Tracing Carbonate Formation, Serpentinization, and Biological Materials With Micro-/Meso-Scale Infrared Imaging Spectroscopy in a Mars Analog System, Samail Ophiolite, Oman. *Earth and Space Science*, *8*(11). https://doi.org/10.1029/2021EA001637

Liu, Y., Fischer, W. W., Ma, C., Beckett, J. R., Tschauner, O., Guan, Y., Lingappa, U. F., Webb, S. M., Prakapenka, V. B., Lanza, N. L., & Agee, C. B. (2021). Manganese oxides in Martian meteorites Northwest Africa (NWA) 7034 and 7533. *Icarus*, *364*, 114471. https://doi.org/10.1016/j.icarus.2021.114471

Liu, Y., Tice, M. M., Schmidt, M. E., Treiman, A. H., Kizovski, T. V., Hurowitz, J. A., Allwood, A. C., Henneke, J., Pedersen, D. A. K., VanBommel, S. J., Jones, M. W. M., Knight, A. L., Orenstein, B. J., Clark, B. C., Elam, W. T., Heirwegh, C. M., Barber, T., Beegle, L. W., Benzerara, K., … Zorzano, M.-P. (2022). An olivine cumulate outcrop on the floor of Jezero crater, Mars. *Science*, *377*(6614), 1513–1519. https://doi.org/10.1126/science.abo2756

Liu, Y.-G., Miah, M. R. U., & Schmitt, R. A. (1988). Cerium: A chemical tracer for paleo-oceanic redox conditions. *Geochimica et Cosmochimica Acta*, *52*(6), 1361–1371. https://doi.org/10.1016/0016-7037(88)90207-4

Lu, J., Chen, W., Zhang, W., Liu, H., Simonetti, A., Hu, Z., Liu, Y., Zhao, K., & Jiang, S. (2022). Determination of carbon isotopes in carbonates (calcite, dolomite, magnesite, and siderite) by femtosecond laser ablation multi-collector ICP-MS. *Journal of Analytical Atomic Spectrometry*, *37*(2), 278–288. https://doi.org/10.1039/D1JA00356A

Lugli, S., Torres-Ruiz, J., Garuti, G., & Olmedo, F. (2000). Petrography and Geochemistry of the Eugui Magnesite Deposit(Western Pyrenees, Spain): Evidence for the Development of a PeculiarZebra Banding by Dolomite

Replacement. *Economic Geology*, *95*(8), 1775–1791. https://doi.org/10.2113/gsecongeo.95.8.1775

McDonough, W. F., & Sun, S. -s. (1995). The composition of the Earth. *Chemical Geology*, *120*(3–4), 223–253. https://doi.org/10.1016/0009-2541(94)00140-4

Mervine, E. M., Sims, K. W. W., Humphris, S. E., & Kelemen, P. B. (2015). Applications and limitations of U–Th disequilibria systematics for determining ages of carbonate alteration minerals in peridotite. *Chemical Geology*, *412*, 151–166. https://doi.org/10.1016/j.chemgeo.2015.07.023

Milburn, D., & Wilcock, S. (1994). The Kunwarara magnesite deposit, Central Queensland. *In Field Conference '94 Capricorn Region: Geological Society of Australia*, 99–107.

Milburn, D., & Wilcock, S. (1998). Kunwarara Magnesite Depsoit. *Geology of Australian and Papua New Guinean Mineral Deposits*, 815–818.

Mitra, K., Moreland, E. L., Ledingham, G. J., & Catalano, J. G. (2023). Formation of manganese oxides on early Mars due to active halogen cycling. *Nature Geoscience*, *16*(2), 133–139. https://doi.org/10.1038/s41561-022-01094-y

Ratié, G., Zhang, K., Iqbal, M., Vantelon, D., Mahé, F., Rivard, C., Komárek, M., Bouhnik-Le Coz, M., Dia, A., Hanna, K., Davranche, M., & Marsac, R. (2023). Driving forces of Ce(III) oxidation to Ce(IV) onto goethite. *Chemical Geology*, *633*, 121547. https://doi.org/10.1016/j.chemgeo.2023.121547

Scheller, E. L., Razzell Hollis, J., Cardarelli, E. L., Steele, A., Beegle, L. W., Bhartia, R., Conrad, P., Uckert, K., Sharma, S., Ehlmann, B. L., Abbey, W. J., Asher, S. A., Benison, K. C., Berger, E. L., Beyssac, O., Bleefeld, B. L., Bosak, T., Brown, A. J., Burton, A. S., … Zorzano, M.-P. (2022). Aqueous alteration processes in Jezero crater, Mars—Implications for organic geochemistry. *Science*, *378*(6624), 1105–1110. https://doi.org/10.1126/science.abo5204

Scheller, E. L., Swindle, C., Grotzinger, J., Barnhart, H., Bhattacharjee, S., Ehlmann, B. L., Farley, K., Fischer, W. W., Greenberger, R., Ingalls, M., Martin, P. E., Osorio-Rodriguez, D., & Smith, B. P. (2021). Formation of Magnesium Carbonates on Earth and Implications for Mars. *Journal of Geophysical Research: Planets*, *126*(7). https://doi.org/10.1029/2021JE006828

Searston, S. (1998). *Resource Estimation and the kunwarara Magnesite Deposit* [Masters Thesis]. University of Tasmania.

Simon, J. I., Hickman-Lewis, K., Cohen, B. A., Mayhew, L. E., Shuster, D. L., Debaille, V., Hausrath, E. M., Weiss, B. P., Bosak, T., Zorzano, M. -P., Amundsen, H. E. F., Beegle, L. W., Bell, J. F., Benison, K. C., Berger, E. L., Beyssac, O., Brown,

A. J., Calef, F., Casademont, T. M., … Williford, K. H. (2023). Samples Collected From the Floor of Jezero Crater With the Mars 2020 Perseverance Rover. *Journal of Geophysical Research: Planets*, *128*(6), e2022JE007474. https://doi.org/10.1029/2022JE007474

Smirnova, E. V., Mysovskaya, I. N., Lozhkin, V. I., Sandimirova, G. P., Pakhomova, N. N., & Smagunova, A. A. (2006). Spectral interferences from polyatomic barium ions in inductively coupled plasma mass spectrometry. *Journal of Applied Spectroscopy*, *73*(6), 911–917. https://doi.org/10.1007/s10812-006-0175-0

Smrzka, D., Zwicker, J., Bach, W., Feng, D., Himmler, T., Chen, D., & Peckmann, J. (2019). The behavior of trace elements in seawater, sedimentary pore water, and their incorporation into carbonate minerals: A review. *Facies*, *65*(4), 41. https://doi.org/10.1007/s10347-019-0581-4

Tostevin, R., Shields, G. A., Tarbuck, G. M., He, T., Clarkson, M. O., & Wood, R. A. (2016). Effective use of cerium anomalies as a redox proxy in carbonate-dominated marine settings. *Chemical Geology*, *438*, 146–162. https://doi.org/10.1016/j.chemgeo.2016.06.027

Toulkeridis, T., Peucker-Ehrenbrink, B., Clauer, N., Kröner, A., Schidlowski, M., & Todt, W. (2010). Pb–Pb age, stable isotope and chemical composition of Archaean magnesite, Barberton Greenstone Belt, South Africa. *Journal of the Geological Society*, *167*(5), 943–952. https://doi.org/10.1144/0016-76492009-140

Wendt, L., Gross, C., Kneissl, T., Sowe, M., Combe, J.-P., LeDeit, L., McGuire, P. C., & Neukum, G. (2011). Sulfates and iron oxides in Ophir Chasma, Mars, based on OMEGA and CRISM observations. *Icarus*, *213*(1), 86–103. https://doi.org/10.1016/j.icarus.2011.02.013

Yu, J., Day, J., Greaves, M., & Elderfield, H. (2005). Determination of multiple element/calcium ratios in foraminiferal calcite by quadrupole ICP-MS: FORAMINIFERAL CALCITE. *Geochemistry, Geophysics, Geosystems*, *6*(8), n/a-n/a. https://doi.org/10.1029/2005GC000964

Zhang, R. Y., & Liou, J. G. (1994). Significance of magnesite paragenesis in ultrahigh-pressure metamorphic rocks. *American Mineralogist*, *79*(3–4), 397–400.

Zhao, Y., Wei, W., Santosh, M., Hu, J., Wei, H., Yang, J., Liu, S., Zhang, G., Yang, D., & Li, S. (2022). A review of retrieving pristine rare earth element signatures from carbonates. *Palaeogeography, Palaeoclimatology, Palaeoecology*, *586*, 110765. https://doi.org/10.1016/j.palaeo.2021.110765

Chapter 3

FRAMEWORK FOR A VOLUME MODEL FOR MONOCLINIC AMPHIBOLE

3.1 Abstract

We developed a framework for a volume model for monoclinic amphiboles that can be applied to a new amphibole solution model compatible with the MELTS algorithm. A calibrated model permits estimation of amphibole volumes for compositions in the oxide space $SiO_2\text{-}TiO_2\text{-}Al_2O_3\text{-}Cr_2O_3\text{-}FeO\text{-}Fe_2O_3\text{-}MnO\text{-}MgO\text{-}Na_2O\text{-}K_2O\text{-}H_2O\text{-}F$, expressed as linear combinations of the end-member components tremolite [$\square Ca_2Mg_5Si_8O_{22}(OH)_2$], cummingtonite [$\square Mg_7Si_8O_{22}(OH)_2$], grunerite [$\square Fe^{2+}_7Si_8O_{22}(OH)_2$], permanganogrünerite [$\square Mn_7Si_8O_{22}(OH)_2$], pargasite [$NaCa_2(Mg_4Al)(Al_2Si_6)O_{22}(OH)_2$], magnesiohastingsite [$NaCa_2(Mg_4Fe^{3+})(Al_2Si_6)O_{22}(OH)_2$], tschermakite [$\square Ca_2(Mg_3Al_2)(Al_2Si_6)O_{22}(OH)_2$], chromiopargasite [$NaCa_2(Mg_4Cr^{3+})(Al_2Si_6)O_{22}(OH)_2$], K-richterite [$K(NaCa)Mg_5Si_8O_{22}(OH)_2$], glaucophane [$\square Na_2(Mg_3Al_2)Si_8O_{22}(OH)_2$], kaersutite [$NaCa_2(Mg_3Ti^{4+}Al)(Al_2Si_6)O_{22}(O)_2$], oxymagnesiohastingsite [$NaCa_2(Mg_2Fe^{3+}_3)(Al_2Si_6)O_{22}(O)_2$] and fluorotremolite [$\square Ca_2Mg_5Si_8O_{22}(F)_2$]. The framework accounts for A-B ordering, B-C ordering, and C-T ordering in the amphibole lattice, although the ordering state is fixed at each end member. These components were chosen to allow the incorporation of minor components that are not present in the existing amphibole models that accompany the MELTS algorithm. These minor components may help stabilize amphibole through their configurational contribution to the Gibbs energy. We used this framework to fit a preliminary volume model for clino-amphiboles using site

occupancy data sourced from x-ray refinements from the American Mineralogist Crystal Structure Database and the Istituto di Geoscienze e Georisorse (Pavia, Italy) databases plus additional refinements from peer-reviewed journals. We initially fit a linear model and then used volume residuals and χ^2 statistics to select second-order parameters that capture nonlinear mixing behavior. We test the quality of the fit parameters using χ^2 statistics and by a Monte Carlo scheme aimed at gauging the quality of the model parameters, given measured and estimated uncertainties in the data. Interrogation of the available x-ray refinement data uncovers regions in amphibole composition-ordering space that are insufficiently characterized to be confidently described by our model (particularly Mn-amphiboles). We further address regions where x-ray refinement data is lacking in high pressure and high temperature regimes, which will be a limiting factor in terms of extending the calibration to account for compressibility and thermal expansion.

3.2 Introduction

The MELTS algorithm has been widely used to model the thermodynamical evolution of magmas in chemically complex geological systems. The family of MELTS models have been optimized for simulating magmatic evolution in a variety of important compositional and pressure-temperature ranges (e.g., Asimow *et al*., 2004; Ghiorso *et al.*, 2002; Ghiorso and Sack, 1995; Gualda *et al.*, 2012), and have been remarkably successful in regimes where amphibole is absent. However, amphibole rarely crystalizes in current implementations of the MELTS software, even under conditions where well-controlled experiments definitely indicate that amphibole ought to be stable (e.g., Mutch *et al*., 2016). We speculate that this is due to the absence of minor components (elements) that are frequently incorporated into the crystal lattices of natural (e.g., Evans and Yang, 1998; Tribaudino *et al.*, 2022) and experimentally produced (e.g., Mutch *et al.*, 2016) amphiboles but are not currently accounted for in any of the amphibole solution models used by MELTS (Ghiorso *et al.*, 2002; Gualda *et al.*, 2012). The decrease in Gibbs energy required for amphibole stabilization in the current implementations of the model (affinity) often amounts to several kJ/mol, which is on the order of the configurational entropy contribution to the Gibbs energy associated with substitution of small amounts of these minor components (~1 mol%) onto sites in the crystal lattice at magmatic temperatures (i.e. 1 mol% of a substitution on a site at 1000 K adds $-RT(.01)\ln[.01] = 383$ J/mol to the Gibbs energy). Compared to the configurational entropy contribution, changes in the vibrational Gibbs energy associated with such concentrations of these minor components would likely be small or perhaps even negligible.

Improving the MELTS algorithm with a working solution model for amphibole will enable thermodynamic modeling of intermediate and felsic magma systems including amphibole-crystallizing melts of dioritic, andesitic, and dacitic composition. Such a leap forward could aid in improvements to crustal barometers applied to igneous rocks, which are currently highly uncertain and potentially inaccurate (e.g., Bardelli *et al.*, 2023; Putirka, 2016; Wieser *et al.*, 2023). Additionally, successful implementation could enable petrologists to place constraints on mechanisms associated with the formation of the continental crust, which are not well understood (Aarons *et al.*, 2021; Collins *et al.,* 2020).

A preliminary step needed to produce such a model is to develop a volume model for monoclinic amphiboles that predicts how amphibole volumes change as a function of composition and ordering at STP, including the influence of minor components. Changes in volume associated with minor components are important because molar volume is the pressure derivative of molar Gibbs energy at constant temperature, and while the differences in volume associated with the incorporation of a minor component may be small in most natural amphiboles, they can be meaningful with respect to Gibbs energy when integrating over GPa-scale pressure intervals. Previous volume calibrations utilized in amphibole solution models estimate end-member volumes, citing studies that require extrapolations from analogous end members, while doing little to assess non-linearity associated with mixing between end members (e.g., Ghiorso *et al.*, 1995).

We outline the framework for a volume model for monoclinic amphiboles and test its viability utilizing available x-ray diffraction (XRD) refinement data for a diverse range of such amphiboles. We begin by setting the framework of the model, and then describe the assembly and filtering of a collection of XRD refinements for amphiboles with site occupancies that are compatible with our formulation. The site occupancy data derived from Rietveld refinements of amphiboles with well-determined compositions are mapped to the mole fractions of compositionally independent amphibole end members and ordering parameters that define our model space. We then initially fit a "first-order" model that includes only linear parameters. Second-order parameters are then added sparingly, incorporated only when the data indicate obvious non-ideal mixing along binary joins or when they dramatically improve the quality of the fit. When a second-order parameter is selected, the entire model is refit (all linear and second-order parameters).

We estimate the extent to which the uncertainties associated with the compositional, volume and (to a lesser extent) ordering data influence the model parameters by applying a Monte Carlo scheme to our weighted least squares regression. We discuss the extent to which different model parameters are robust, map the regimes in composition and ordering space where available data is limited, and suggest experiments that could be useful to remove these gaps in the data set. Finally, we discuss formulations that could be used to estimate the thermal expansion and compressibility of amphiboles once a greater quantity of diffraction data collected at nonambient conditions is available.

3.3 Methods

3.3.1 Selection of Compositional End Members and Ordering Parameters

The continually growing amphibole supergroup is immense, with over 100 named end-member compositions (e.g., Hawthorne *et al.*, 2012; 2022; Holtstam *et al.*, 2022) due to the many viable ionic substitutions that are accommodated in the amphibole crystal lattice. The objective of this endeavor is to lay out the framework for a volume model that predicts how the unit cell volumes of *C2/m* clino-amphiboles change with variations in composition and ordering state at standard temperature and pressure (STP). The amphibole structure hosts (per formula unit) eight tetrahedral cation sites grouped into four T1 sites and four T2 sites; five strictly octahedral cation sites consisting of two M1 sites, two M2 sites and one M3 site; two cation sites of six- to eight-fold coordination deemed the two M4 sites, and one ten- to twelve-fold coordination cation site termed the A site (Ernst, 1968). The amphibole structure hosts twenty-four anion sites per formula unit, all of which strictly host O^{2-} except for two O3 sites, which can host OH^-, F^-, and Cl^- in addition to O^{2-} anions (Ernst, 1968; Hawthorne *et al.,* 2012). We decided to simplify the crystallographic sites in the model by grouping T as the sum of the four T1 and the four T2 sites, C as the sum of the two M1 sites, the two M2 sites and the one M3 site, and B as the sum of the two M4 sites. These simplifications may conceal some potentially significant correlations, such as the positive correlation between the b axis length and the mean radius of the M2 cations highlighted by Ernst (1968). Since M2 is not separate from M1 and M3 in our formulation, our model would not directly capture this behavior. However, these simplifications allow incorporation of XRD refinements where ordering between among M1, M2, and M3 sites or between T1 and T2 sites is either not given or not well-determined.

We defined compositional and order parameters that allow, per formula unit, Si^{4+} and Al^{3+} in the eight T sites; Mg^{2+}, Fe^{2+}, Al^{3+}, Fe^{3+}, Cr^{3+}, Ti^{4+}, and Mn^{2+} in the five C sites; Ca^{2+}, Mg^{2+}, Fe^{2+}, Na^{+}, and Mn^{2+} in the two B sites; Na^{+}, K^{+}, Ca^{2+}, and vacancies (☐) in the A site; and OH^{-}, F^{-}, and O^{2-} in the two O3 sites, all of which are charge balanced by twenty-two oxygens (O^{2-}). Because our intent is to produce a model that ultimately will be incorporated into the MELTS family of thermodynamic models (Ghiorso *et al.,* 2002; Gualda *et al.,* 2012) we limit our ambition to those elements and oxidation states presently considered in the MELTS model, which excludes a large number of amphibole species that have essential Li, Be, Pb, Zn, V, Zr, or Cl (Hawthorne *et al.*, 2012). These elements are not (and may never) be present in the MELTS models. Selected ions were also chosen based on their presence in structural refinement data and their proportions in magmatic amphiboles. Oxidation states of cations not considered in MELTS were also excluded from the model (e.g., Mn^{4+}, Mn^{3+}, Cr^{6+}, Ti^{3+}, Ti^{2+}). While Ti^{4+} can be hosted on the C sites and the T sites (e.g., Oberti *et al.*, 1992), we choose to only allow Ti^{4+} on the C sites, where it is typically situated in most amphiboles. The same is the case for similar instances for other elements (e.g., we rejected amphiboles with Na^{+} on C sites in the Istituto di Geoscienze e Georisorse [IGG] database).

We anticipate that these minor simplifications will still facilitate the desirable stabilization of amphibole in the MELTS software.

Assuming twenty-two moles of non-hydroxyl oxygen, we tabulated the total moles of each ion (as site occupancy data in the form of mole fraction of each ion on each site) as described in Equation 3.1:

$$\begin{bmatrix} K_A^+ \\ Ti_C^{4+} \\ Cr_C^{3+} \\ Mn_B^{2+} + Mn_C^{2+} \\ Fe_B^{2+} + Fe_C^{2+} \\ F_{O3}^- \\ Fe_C^{3+} \\ Na_A^+ + Na_B^+ \\ Ca_A^{2+} + Ca_B^{2+} \\ OH_{O3}^- \\ Si_T^{4+} \\ Al_C^{3+} + Al_T^{3+} \\ Mg_B^{2+} + Mg_C^{2+} \end{bmatrix} = \begin{bmatrix} K^+ \\ Ti^{4+} \\ Cr^{3+} \\ Mn^{2+} \\ Fe^{2+} \\ F^- \\ Fe^{3+} \\ Na^+ \\ Ca^{2+} \\ OH^- \\ Si^{4+} \\ Al^{3+} \\ Mg^{2+} \end{bmatrix} \tag{3.1}$$

except for O^{2-} on the hydroxyl (O3) site and vacancies on A, which are both implicit, and are not necessary to map from site occupancies to compositional parameters described later in this section.

Thirteen compositionally independent amphibole end members were selected to span the range of amphiboles that can be constructed by the site-specific ions permitted by our framework (Table 3.1). Note that a wide variety of amphibole species can be produced by linear combinations of these end members (e.g., ferroactinolite, $(\square)(Ca_2)(Fe_5)(Si_8)O_{22}(OH)_2$, is equivalent to tremolite + (5/7)grunerite –(5/7)cummingtonite) and need not be explicit end members in order to capture their volumes. Ordering parameters that characterize A-B ordering of Ca and B-C ordering of Mg and Fe are described in Equations 3.2-3.4:

$$S_1 = S_{Fe} = \frac{Fe_B^{2+}}{2} - \frac{Fe_C^{2+}}{5}; \tag{3.2}$$

$$S_2 = S_{Mg} = \frac{Mg_B^{2+}}{2} - \frac{Mg_C^{2+}}{5}; \tag{3.3}$$

$$S_3 = S_{Ca} = Ca_A^{2+}. \tag{3.4}$$

The A-B ordering of Na, B-C ordering of Mn, and C-T ordering of Al are implicit. While a B-C ordering parameter for Mn is potentially significant in the volume of some Mn-rich compositions, we prefer to parameterize in terms of the ordering of Mg and keep the Mn ordering implicit because Fe and Mn have similar x-ray scattering characteristics and are often clumped together when assessing cation ordering in amphiboles (e.g., Yong *et al.*, 2019). If the molar Fe/Mn ratio of an amphibole is very large or very small, or if the mole fractions of both Mn and Fe are very small, then the use of Fe and Mg B-C ordering parameters determined by Rietveld refinement of XRD data should suffice. For amphiboles with intermediate Fe/Mn (maybe ~0.5-5), we suggest that Fe-Mn site ordering be verified by alternative techniques such as neutron diffraction (e.g., Reece *et al.*, 2002). Note, we do use the implicitly determined B-C ordering parameter for Mn to map from our independent variable vectors back to site occupancies later in this work.

Table 3.1. Compositional end members in $AB_2C_5T_8O_{22}(O3)_2$ form. Fe refers to Fe^{2+} unless specifically shown otherwise. All other valence states are in accordance with those outlined in the framework.

End member	Reference Name	Chemical Formulation
R_1	Tremolite	$(\square)(Ca_2)(Mg_5)(Si_8)O_{22}(OH)_2$
R_2	Cummingtonite	$(\square)(Mg_2)(Mg_5)(Si_8)O_{22}(OH)_2$
R_3	Grünerite	$(\square)(Fe_2)(Fe_5)(Si_8)O_{22}(OH)_2$
R_4	Permanganogrünerite	$(\square)(Mn_2)(Mn_5)(Si_8)O_{22}(OH)_2$
R_5	Pargasite	$(Na)(Ca_2)(Mg_4Al)(Al_2Si_6)O_{22}(OH)_2$
R_6	Magnesiohastingsite	$(Na)(Ca_2)(Mg_4Fe^{3+})(Al_2Si_6)O_{22}(OH)_2$
R_7	Tschermakite	$(\square)(Ca_2)(Mg_3Al_2)(Al_2Si_6)O_{22}(OH)_2$
R_8	Chromiopargasite	$(Na)(Ca_2)(Mg_4Cr^{3+})(Al_2Si_6)O_{22}(OH)_2$
R_9	K-Richterite	$(K)(NaCa)(Mg_5)(Si_8)O_{22}(OH)_2$
R_{10}	Glaucophane	$(\square)(Na_2)(Mg_3Al_2)(Si_8)O_{22}(OH)_2$
R_{11}	Kaersutite	$(Na)(Ca_2)(Mg_3Ti^{4+}Al)(Al_2Si_6)O_{22}(O)_2$
R_{12}	Oxymagnesiohastingsite	$(Na)(Ca_2)(Mg_2Fe^{3+}{}_3)(Al_2Si_6)O_{22}(O)_2$
R_{13}	Fluorotremolite	$(\square)(Ca_2)(Mg_5)(Si_8)O_{22}(F)_2$

Molar bulk ionic abundance vectors calculated site from occupancies via Equation 3.1 are mapped to the compositional end members (the $\vec{R}$ vector) by matrix multiplication as shown in Equation 3.5 (overbars indicate repeating decimals):

$$\begin{bmatrix} -0.58\bar{3} & -0.\bar{3} & -0.25 & -0.1\bar{6} & -0.1\bar{6} & -0.58\bar{3} & -0.25 & -0.08\bar{3} & 0.\bar{3} & -0.08\bar{3} & 0.1\bar{6} & -0.25 & -0.1\bar{6} \\ -0.13541\bar{6} & -0.041\bar{6} & 0.09375 & 0.0863\overline{095238} & 0.0863\overline{095238} & -0.13541\bar{6} & 0.09375 & -0.13541\bar{6} & -0.2708\bar{3} & -0.13541\bar{6} & -0.041\bar{6} & 0.09375 & 0.2291\bar{6} \\ 0 & 0 & 0 & 0 & 0.\overline{142857} & 0 & 0 & 0 & 0 & 0 & 0 & 0 & 0 \\ 0 & 0 & 0 & 0.\overline{142857} & 0 & 0 & 0 & 0 & 0 & 0 & 0 & 0 & 0 \\ -0.2708\bar{3} & -3.08\bar{3} & -0.8125 & 0.458\bar{3} & 0.458\bar{3} & -1.2708\bar{3} & -0.8125 & 0.7291\bar{6} & 0.458\bar{3} & -1.2708\bar{3} & -0.08\bar{3} & 0.1875 & 0.458\bar{3} \\ -0.0625 & 2.75 & -0.1875 & -0.125 & -0.125 & 1.4375 & 0.8125 & -0.0625 & -0.125 & 1.4375 & -0.25 & -0.1875 & -0.125 \\ 0.3958\bar{3} & 0.58\bar{3} & 0.1875 & -0.208\bar{3} & -0.208\bar{3} & 0.3958\bar{3} & 0.1875 & -0.6041\bar{6} & -0.208\bar{3} & 0.3958\bar{3} & 0.08\bar{3} & 0.1875 & -0.208\bar{3} \\ 0 & 0 & 1 & 0 & 0 & 0 & 0 & 0 & 0 & 0 & 0 & 0 & 0 \\ 1 & 0 & 0 & 0 & 0 & 0 & 0 & 0 & 0 & 0 & 0 & 0 & 0 \\ -0.34375 & 0.125 & -0.03125 & -0.1875 & -0.1875 & 0.15625 & -0.03125 & 0.15625 & -0.1875 & 0.15625 & 0.125 & -0.03125 & -0.1875 \\ 0 & 1 & 0 & 0 & 0 & 0 & 0 & 0 & 0 & 0 & 0 & 0 & 0 \\ 0.0208\bar{3} & -0.91\bar{6} & 0.0625 & 0.041\bar{6} & 0.041\bar{6} & -0.4791\bar{6} & 0.0625 & 0.0208\bar{3} & 0.041\bar{6} & -0.4791\bar{6} & 0.08\bar{3} & 0.0625 & 0.041\bar{6} \\ 0 & 0 & 0 & 0 & 0 & 0 & 0 & 0 & 0 & 0 & 0 & 0 & 0 \end{bmatrix} * \begin{bmatrix} K^{+} \\ Ti^{4+} \\ Cr^{3+} \\ Mn^{2+} \\ Fe^{2+} \\ F^{-} \\ Fe^{3+} \\ Na^{+} \\ Ca^{2+} \\ OH^{-} \\ Si^{4+} \\ Al^{3+} \\ Mg^{2+} \end{bmatrix} = \begin{bmatrix} R_1 \\ R_2 \\ R_3 \\ R_4 \\ R_5 \\ R_6 \\ R_7 \\ R_8 \\ R_9 \\ R_{10} \\ R_{11} \\ R_{12} \\ R_{13} \end{bmatrix}. \qquad (3.5)$$

Order parameters (the $\vec{S}$ vector) are directly calculated from site occupancy derived from the Rietveld refinements as described in Equations 3.2-3.4. The implicit ordering parameter that describes B-C ordering of Mn is also calculated using the site occupancy data via Equation 3. 6:

$$S_{Mn} = \frac{Mn_B^{2+}}{2} - \frac{Mn_C^{2+}}{5} \tag{3.6}$$

and is stored for future operational use (not as an independent variable in the volume model). The resulting *R*-*S* parameters form the independent variables for our model of amphibole volumes as a function of their composition and ordering state at STP, which we now proceed to calibrate on the basis of structural refinement data gathered from amphiboles at STP.

3.3.2 Linear Model

The general form of the model is described in Equation 3.7, wherein the a_i coefficients express linear dependence of volumes on compositional parameters (i.e., the unit cell volumes of the 13 pure end members); b_i coefficients express linear dependence on ordering parameters; and $a_{i,j}$, $b_{i,j}$, and $c_{i,j}$ coefficients account for the second-order behavior associated with product of two R parameters, two S parameters, or an $R*S$ pair, respectively:

$$\begin{aligned} V(\vec{R},\vec{S}) &= \textstyle\sum_{i=1}^{13} a_i R_i + \sum_{i=1}^{3} b_i S_i + \sum_{i=1}^{13}\sum_{j=1}^{13} a_{i,j} R_i R_j \\ &\quad + \textstyle\sum_{i=1}^{3}\sum_{j=1}^{3} b_{i,j} S_i S_j + \sum_{i=1}^{13}\sum_{j=1}^{3} c_{i,j} R_i S_j \end{aligned} \tag{3.7}$$

The function $V(\vec{R},\vec{S})$ is compatible with the coding of solid volume models in MELTS, which requires that the volume model yield the end-member volume $V_i = a_i$ for each pure end member, when $R_i = 1$, and all other R_j and all S values are zero. This was an additional criterion on the selection of end members; they are each constructed so that S_{Fe} is fixed at zero in the pure end member and this allows its use in the linear model. Thus, we set first order model coefficients (b_2 and b_3) corresponding to S_{Mg} and S_{Ca} to zero. As previously mentioned, S_{Mn} is not used to model volume. Note, V is expressed as unit cell volume in Å^3; it is simple to convert it to molar volume in J/bar or cm^3/mol using Avogadro's number and the $Z = 2$ multiplicity of the formula unit in the unit cell.

To fit the first order model, we define a linear least squares problem

$$\mathbb{A}_{\text{Linear}}\vec{X}_{\text{Linear}} = \vec{B}, \tag{3.8}$$

where the rows of matrix $\mathbb{A}$ contain the $\vec{R}$-$\vec{S}$ vector for each data point weighted by their uncertainties and the $\vec{B}$ vector is the corresponding unit cell volume data weighted by its uncertainties:

$$\mathbb{A}_{Linear} = \begin{bmatrix} \frac{R_{1,1}}{\sigma_{R_{1,1}}} & \frac{R_{2,1}}{\sigma_{R_{2,1}}} & \frac{R_{3,1}}{\sigma_{R_{3,1}}} & \frac{R_{4,1}}{\sigma_{R_{4,1}}} & \frac{R_{5,1}}{\sigma_{R_{5,1}}} & \frac{R_{6,1}}{\sigma_{R_{6,1}}} & \frac{R_{7,1}}{\sigma_{R_{7,1}}} & \frac{R_{8,1}}{\sigma_{R_{8,1}}} & \frac{R_{9,1}}{\sigma_{R_{9,1}}} & \frac{R_{10,1}}{\sigma_{R_{10,1}}} & \frac{R_{11,1}}{\sigma_{R_{11,1}}} & \frac{R_{12,1}}{\sigma_{R_{12,1}}} & \frac{R_{13,1}}{\sigma_{R_{13,1}}} & \frac{S_{Fe,1}}{\sigma_{S_{Fe,1}}} \\ \vdots & \vdots & \vdots & \vdots & \vdots & \vdots & \vdots & \vdots & \vdots & \vdots & \vdots & \vdots & \vdots & \vdots \\ \frac{R_{1,n}}{\sigma_{R_{1,n}}} & \frac{R_{2,n}}{\sigma_{R_{2,n}}} & \frac{R_{3,n}}{\sigma_{R_{3,n}}} & \frac{R_{4,n}}{\sigma_{R_{4,n}}} & \frac{R_{5,n}}{\sigma_{R_{5,n}}} & \frac{R_{6,n}}{\sigma_{R_{6,n}}} & \frac{R_{7,n}}{\sigma_{R_{7,n}}} & \frac{R_{8,n}}{\sigma_{R_{8,n}}} & \frac{R_{9,n}}{\sigma_{R_{9,n}}} & \frac{R_{10,n}}{\sigma_{R_{10,n}}} & \frac{R_{11,n}}{\sigma_{R_{11,n}}} & \frac{R_{12,n}}{\sigma_{R_{12,n}}} & \frac{R_{13,n}}{\sigma_{R_{13,n}}} & \frac{S_{Fe,n}}{\sigma_{S_{Fe,n}}} \end{bmatrix} \tag{3. 9}$$

$$\vec{B} = \begin{bmatrix} \frac{V_1}{\sigma_{V_1}} \\ \vdots \\ \frac{V_n}{\sigma_{V_{\text{n}}}} \end{bmatrix} \tag{3.10}$$

where n is the number of data points in the filtered data set. The model vector:

$$\vec{X}_{\text{Linear}} = [a_1 \cdots a_{13}, b_1]^T \tag{3.11}$$

is calibrated via weighted least squares minimization using the singular value decomposition. Composition and ordering data uncertainties are propagated from uncertainty in the reported site occupancy data. Volume data in $\vec{B}$ (Eq. (3.10) and the R's and S's in $\mathbb{A}$ (Eq. (3.9)) are weighted by the stated uncertainty on volume or by 1 Å^3, whichever is largest. This minimum volume uncertainty was adopted because several references state only the random component of their uncertainty, which may be extremely small (e.g., V=905.733 Å^3, σ=0.002 Å^3 for a tremolite in Antao *et al.*, 2008). Using this nominal error as a weight in the weighted least squares regression would excessively bias the model towards the subset of the data that neglect to include systematic error in their published uncertainties. The cutoff of 1 Å^3 represents our estimate of interlaboratory and other biases and yields better balance of weights among the data sources at this stage of fitting. The nominal σ values reported with each amphibole volume datum are retained for referenced in the supplementary data file (Swindle, 2023).

3.3.3 Second-Order Parameters

As with the linear model, the second-order model terms must also vanish at each pure endmember. This is accomplished by requiring that (i) $a_{i,i}$ and $b_{i,i}$ are zero for all i (except for $b_{1,1}$ since S_{Fe} is zero at all end member R's); (ii) $b_{2,3} = 0$, since S_{Mg} and S_{Ca} may not be zero in pure end-member compositions; and (iii) those $c_{i,j}$ parameters that do not vanish at all pure end members are zero (e.g., $c_{2,1}$ corresponding to an $S_{Mg}*R_1$ term is not permitted because pure end-member tremolite ($R_1 = 1$) has $S_{Mg} = -1$, whereas $c_{2,2}$ corresponding to an $S_{Mg}*R_2$ term is allowable because pure end-member cummingtonite ($R_2 = 1$) has $S_{Mg} = 0$).

When selecting second-order parameters to add to the linear model, we consider (i) the extent to which binary joins between pairs of end members show non-linearity in the available volume data close to the binary and (ii) the extent to which adding a given second-order parameters improves the quality of the fit. To avoid overfitting, it is wise to be conservative about the number of second-order parameters included in such a model unless the data indicate obvious non-linearity. As with the linear scheme, for each trial set of second-order parameters to be included in the model, we solve a weighted linear least-squares problem, extending the unknown $\vec{X}$ vector by addition of the active parameters to the right side of $\vec{X}_{\mathrm{Linear}}$ and extending the $\mathbb{A}$ matrix by addition of columns containing the relevant products of R and S quantities (weighted by uncertainties on the products) to the right side of $\mathbb{A}_{Linear}$. Data vector $\vec{B}$ remains the same.

3.3.4 R-S Validation Function $F(\vec{R},\vec{S})$

The region of composition and ordering space corresponding to physically realizable stoichiometric amphiboles, with non-negative fractions of all ions on all sites and unity sums of site fractions on each site (accounting for vacancies on A), needs to be defined in order to guarantee that the calculation of thermodynamic functions such as configurational entropy and Gibbs energy is valid. Locating this physically realizable subspace of the overall $(\vec{R},\vec{S})$ vector space is also valuable for assessing the extent to which estimated uncertainties in *R* and *S* data influence the calibration of the volume model. It is easy to show that the physically realizable space is smaller than that defined by the simplest criteria $\{\sum_{i=1}^{13} R_i = 1$ and $-1 \leq S_i \leq 1\}$. For instance, R_3, R_4, R_8, R_9, R_{11}, and R_{13} cannot be negative because these correspond to negative quantities of Fe^{2+}, Mn, Cr, K, Ti, and F. Also, some combinations of composition and order parameters are non-physical, e.g. $R_1 = 1$, $S_{Ca} \neq 0$ and $R_{i\neq 1} = 0$, since all the Ca in tremolite must be on the B site, which forces vacancy on the A site.

To determine whether a given $(\vec{R},\vec{S})$ vector corresponds to a valid amphibole, we first verify that $\sum_{i=1}^{13} R_i = 1$; any vector not satisfying this criterion is immediately rejected. Then we reverse the procedure defined above to compute $(\vec{R},\vec{S})$ from site occupancies, and instead compute site occupancies from $(\vec{R},\vec{S})$ and verify that the obtained site occupancies are consistent with our framework. At this stage we use S_{Mn} instead of S_{Mg}. This is simpler because $\mathrm{Mn}^{2+}{}_{\mathrm{B}}$ and $\mathrm{Mn}^{2+}{}_{\mathrm{C}}$ follow directly from S_{Mn} and R_4. This is not the case for Mg, since total Mg is a function of eleven compositional end members, many of which fix S_{Mg} to a non-zero number at the end member. This is a mathematical convenience and is not affected by the precision issues mentioned above that guided us away from using S_{Mn} in the volume model calibration. The mapping function from $(\vec{R},\vec{S})$ to explicit site occupancies is given by Equation 3.12:

$$\begin{bmatrix} 8 & 8 & 8 & 8 & 6 & 6 & 6 & 6 & 8 & 8 & 6 & 6 & 8 & 0 & 0 & 0 \\ 0 & 0 & 0 & 0 & 0 & 0 & 0 & 0 & 0 & 0 & 0 & 0 & 0 & 0 & 0 & 1 \\ 2 & 0 & 0 & 0 & 2 & 2 & 2 & 2 & 1 & 0 & 2 & 2 & 2 & 0 & 0 & -1 \\ 0 & 0 & 0 & 0 & 0 & 1 & 0 & 0 & 0 & 0 & 0 & 3 & 0 & 0 & 0 & 0 \\ 0 & 0 & 0 & 0 & 0 & 0 & 0 & 0 & 0 & 0 & 0 & 0 & 2 & 0 & 0 & 0 \\ 0 & 0 & 0 & 0 & 0 & 0 & 0 & 1 & 0 & 0 & 0 & 0 & 0 & 0 & 0 & 0 \\ 0 & 0 & 0 & 0 & 0 & 0 & 0 & 0 & 0 & 0 & 1 & 0 & 0 & 0 & 0 & 0 \\ 2 & 2 & 2 & 2 & 2 & 2 & 2 & 2 & 2 & 2 & 0 & 0 & 0 & 0 & 0 & 0 \\ 0 & 0 & 2 & 0 & 0 & 0 & 0 & 0 & 0 & 0 & 0 & 0 & 0 & 10/7 & 0 & 0 \\ 0 & 0 & 5 & 0 & 0 & 0 & 0 & 0 & 0 & 0 & 0 & 0 & 0 & -10/7 & 0 & 0 \\ 0 & 0 & 0 & 2 & 0 & 0 & 0 & 0 & 0 & 0 & 0 & 0 & 0 & 0 & 10/7 & 0 \\ 0 & 0 & 0 & 5 & 0 & 0 & 0 & 0 & 0 & 0 & 0 & 0 & 0 & 0 & -10/7 & 0 \\ 8 & 8 & 8 & 8 & 9 & 8 & 10 & 8 & 8 & 10 & 9 & 8 & 8 & 0 & 0 & 0 \\ 15 & 15 & 15 & 15 & 16 & 16 & 15 & 16 & 15 & 15 & 16 & 16 & 15 & 0 & 0 & -1 \\ -15 & -15 & -15 & -15 & -15 & -15 & -15 & -15 & -14 & -13 & -15 & -15 & -15 & 0 & 0 & 1 \\ 0 & 0 & 0 & 0 & 0 & 0 & 0 & 0 & 1 & 0 & 0 & 0 & 0 & 0 & 0 & 0 \end{bmatrix} \begin{bmatrix} R_1 \\ R_2 \\ R_3 \\ R_4 \\ R_5 \\ R_6 \\ R_7 \\ R_8 \\ R_9 \\ R_{10} \\ R_{11} \\ R_{12} \\ R_{13} \\ S_{Fe} \\ \boldsymbol{S_{Mn}} \\ S_{Ca} \end{bmatrix} \begin{bmatrix} 0 \\ 0 \\ 0 \\ 0 \\ 0 \\ 0 \\ 0 \\ 0 \\ 0 \\ 0 \\ 0 \\ 0 \\ -8 \\ -15 \\ 15 \\ 0 \end{bmatrix} = \begin{bmatrix} Si_T^{4+} \\ Ca_A^{2+} \\ Ca_B^{2+} \\ Fe_C^{3+} \\ F_{O3}^{-} \\ Cr_C^{3+} \\ Ti_C^{4+} \\ OH_{O3}^{-} \\ Fe_B^{2+} \\ Fe_C^{2+} \\ Mn_B^{2+} \\ Mn_C^{2+} \\ Al_C^{3+} \\ Na_A^{+} \\ Na_B^{+} \\ K_A^{+} \end{bmatrix} \tag{3.12}$$

whereas the implicit site occupancies for $\mathrm{Al}^{3+}{}_{\mathrm{T}}$, $\mathrm{O}^{2-}{}_{\mathrm{O3}}$, $\square_{\mathrm{A}}$, $\mathrm{Mg}^{2+}{}_{\mathrm{B}}$, and $\mathrm{Mg}^{2+}{}_{\mathrm{C}}$ are shown in Equations 3.13-3.17:

$$Al_T^{3+} = 8 - Si_T^{4+}; \tag{3.13}$$

$$O_{O3}^{-2} = 2 - F_{O3}^{-} - OH_{O3}^{-}; \tag{3.14}$$

$$\square_A = 1 - K_A^{+} - Na_A^{+} - Ca_A^{2+}; \tag{3.15}$$

$$Mg_B^{2+} = 2 - Na_B^{+} - Fe_B^{2+} - Ca_B^{2+} - Mn_B^{2+}; \tag{3.16}$$

$$Mg_C^{2+} = 5 - Fe_C^{2+} - Mn_C^{2+} - Ti_C^{4+} - Cr_C^{3+} - Fe_C^{3+} - Al_C^{3+}. \tag{3.17}$$

If any of the site occupancies or vacancies (including the implicit ones) are negative, then the $(\vec{R}, \vec{S})$ vector is not consistent with a real amphibole. Otherwise, the amphibole is valid.

3.3.5 Available Data

X-ray refinement data of well-characterized amphiboles sourced from the American Mineralogist Crystal Structure Database (AMCSD), the IGG database and others available in peer reviewed literature collectively yield a dataset of cell volumes of amphiboles associated with compositional and ordering constraints in the form of mole fractions of the elements on each site (Downs and Hall-Wallace, 2003; Hirschmann *et al.*, 1994; Swindle, 2023; Oberti and Boiocchi, 2023). Some pre-processing was required before we could fit these data to our model. First, minor compositional adjustments were made for exotic elements (e.g., Sr, Li, Co, Pb, Ni) with mole fractions ≤0.01 on any site; these were replaced with the most analogous element accounted for in our composition space. Next, small adjustments to the mole fractions of some elements were allowed to enforce perfect charge balance and full occupancy of all sites except for the A site, which can span 0-100 mol% occupancy due to vacancies. These adjustments were usually within the uncertainties of the compositional analyses when reported; any data entry requiring adjustments outside the stated uncertainties to bring it into conformity with our model space were rejected at this stage. Data where uncertainties in lattice parameters or unit cell volumes are not reported were also rejected. The size of the dataset that results from this procedure is $n = 532$. Using the operations discussed in Section 3.3.1 (Equations 3.1-3.5), we mapped the site occupancies to $(\vec{R}, \vec{S})$ vectors, which are reported in the supplementary data set (Swindle, 2023). Data cover a wide range of the *R*-*S* parameter space (Figure 3.1). Given that R_3, R_4,

R_8, R_9, R_{11}, R_{13}, and S_{Ca} cannot be negative, perhaps the most obvious region of limited data in R-S space is $R_4 > 0.2$, which includes only one sample (R_4=0.32). R_4 is mole fraction of permanganogrünerite, so this corresponds to limited coverage of Mn-rich compositions. The diverse range of amphiboles used to calibrate the model are listed in Table 3.2 in accordance with the nomenclature of the amphibole supergroup as described by Hawthorne *et al.* (2012). Volumes span from ~870-945 Å^3 (Figure 3.2). We fit this dataset first to a linear model for amphibole unit cell volumes as a function of $\vec{R}$ and S_{Fe}, as described above.

The quality of the fit after the linear stage and at each subsequent stage of adding second-order parameters is assessed using the reduced χ^2 value of the model:

$$\chi^2 = \left(\frac{1}{n}\right) \sum_{i=1}^{n} \left(\frac{V(\vec{R},\vec{S})_i - V_{i,\text{measured}}}{\sigma_{V_i}}\right)^2, \tag{3.18}$$

where n is the number of data used and σ_{V_i} for each data point is either the stated uncertainty on unit cell volume or 1 Å^3, whichever is greater. Reduced χ^2 values that are much greater than one indicate that the model fit has not fully captured the data, reduced χ^2 values that are around one indicate that the estimations made by the model are in accord with the variance of the observations, and reduced χ^2 values that are less than one indicate that the model is likely over-fitting the data. Second-order parameters were added to the model based on the binary joins, pseudo-joins, and sequentially adding second-order parameters in the order in which the reduced χ^2 is most minimized.

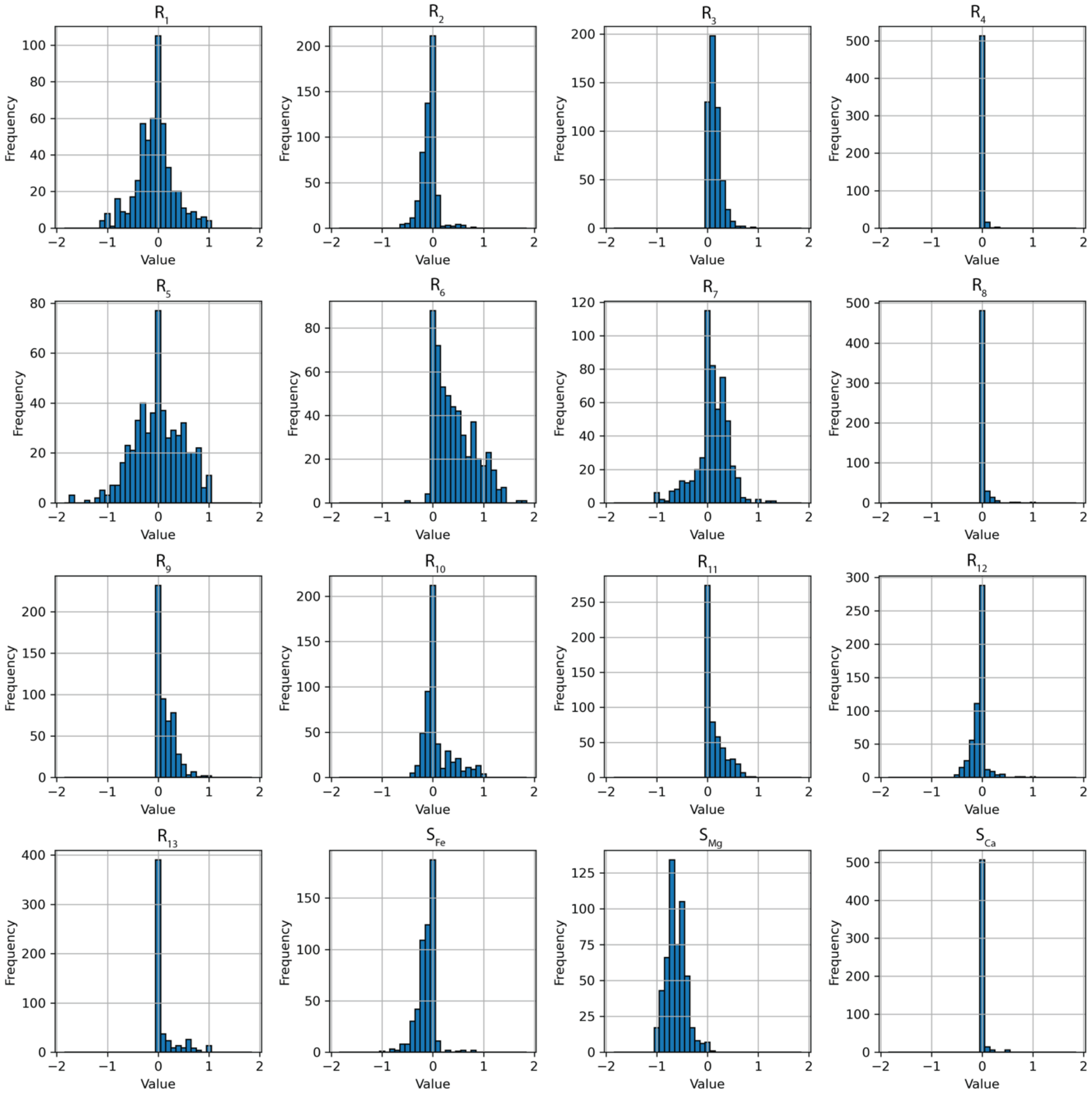

Figure 3.1. Histograms displaying the ranges of *R*-*S* parameters in valid data available from refinements.

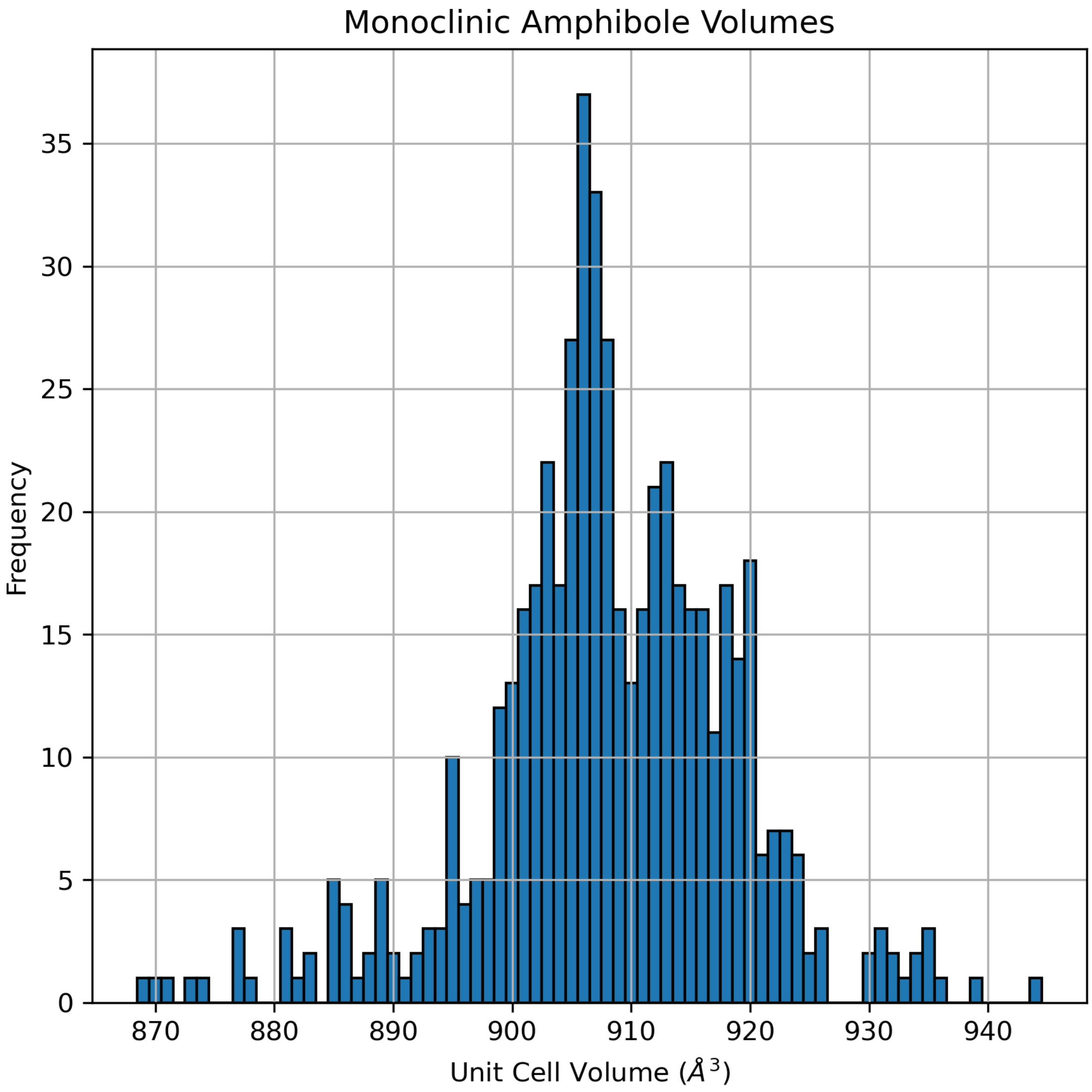

Figure 3.2. Histogram of monoclinic amphibole volumes from x-ray refinement data.

Table 3.2. Number of viable x-ray refinements sorted by amphibole nomenclature as described in Hawthorne *et al.* (2012). The X-ray Refinements column displays the number of x-ray refinements most closely corresponding to each assigned name in the Amphibole Name column. See Hawthorne *et al.* (2012) for a description of the rootname stoichiometry for rootname4 and rootname8.

Amphibole Name	X-ray Refinements
Actinolite	10
Arfvedsonite	1
Barroisite	5
Cannilloite	1
Chromio-fluoro-eckermannite	2
Chromio-pargasite	2
Clino-suenoite	2
Cummingtonite	5
Eckermannite	2
Edenite	4
Ferri-fluoro-katophorite	4
Ferri-katophorite	3
Ferri-rootname4	21
Ferri-sadanagaite	2
Ferri-taramite	1
Ferri-winchite	3
Ferro-actinolite	7
Ferro-glaucophane	3
Ferro-hornblende	9
Ferro-pargasite	3
Ferro-rootname4	1
Ferro-taramite	1
Ferro-tschermakite	1
Fluoro-cannilloite	5
Fluoro-edenite	8
Fluoro-katophorite	1
Fluoro-nybøite	6
Fluoro-pargasite	10
Fluoro-richterite	5
Fluoro-rootname8	2
Fluoro-taramite	2

Amphibole Name	X-ray Refinements
Fluoro-tremolite	4
Glaucophane	9
Grunerite	3
Hastingsite	9
Katophorite	9
Magnesio-arfvedsonite	2
Magnesio-ferri-hornblende	11
Magnesio-fluoro-arfvedsonite	1
Magnesio-fluoro-hastingsite	2
Magnesio-hastingsite	55
Magnesio-riebeckite	2
Nybøite	5
Pargasite	123
Potassic-ferri-rootname4	1
Potassic-ferri-sadanagaite	2
Potassic-ferro-ferri-katophorite	1
Potassic-ferro-ferri-sadanagaite	4
Potassic-ferro-ferri-taramite	1
Potassic-ferro-pargasite	1
Potassic-ferro-taramite	1
Potassic-fluoro-pargasite	3
Potassic-hastingsite	3
Potassic-magnesio-hastingsite	2
Potassic-pargasite	1
Potassic-richterite	4
Richterite	21
Rootname4	14
Taramite	12
Ti-rich chromio-fluoro-katophorite	1
Ti-rich ferri-sadanagaite	9
Ti-rich fluoro-katophorite	1
Ti-rich katophorite	1
Ti-rich magnesio-ferri-hornblende	1
Ti-rich magnesio-hastingsite	9
Ti-rich pargasite	34
Ti-rich potassic-ferri-sadanagaite	1
Ti-rich potassic-sadanagaite	2

Amphibole Name	X-ray Refinements
Ti-rich sadanagaite	1
Tremolite	21
Tschermakite	1
Winchite	12

3.3.6 Influence of Uncertainties

When fitting our model, data in the rows of the $\mathbb{A}$ matrix and the $\vec{B}$ vector are normalized by their uncertainties. In the $\vec{B}$ vector of volumes, as discussed above we use either the stated uncertainty or 1 Å^3, whichever is larger. This weights the influence of each data point by the precision of its volume measurement, while avoiding excessive weights from data that report only the random component of the error. The handling of uncertainty in the $\mathbb{A}$ matrix is, however, a much more complex issue. The site occupancies reported in x-ray refinements are the result of estimation procedures involving either synthesis (for pure synthetic amphiboles) or electron probe analysis (for natural or complex synthetic amphiboles), Mössbauer spectroscopy, infrared spectroscopy, and refinement of site occupancies from X-ray scattering factors. The true uncertainty in bulk composition and site occupancy from this procedure is rarely stated explicitly in the literature. Hence, an assessment of how uncertainty in the site occupancy and volume data propagate to uncertainty in calibrated volume model parameters is crucial to assess the reliability of the calibration and its power to accurately predict volumes of arbitrary amphiboles. We designed a Monte Carlo approach to quantify the influence that the estimated data quality of the $\mathbb{A}$ matrix and the measured or assumed uncertainty on the volumes (i.e., no less than 1 Å^3 and the highest reported in a given publication if it does not report uncertainty for every datum) has on the fitted model parameters. The approach we develop involves generating a series of trial $\mathbb{A}$ matrices and $\vec{B}$ vectors and fitting each trial to obtain a trial set of model parameter values via weighted least squares regression. The average and the standard deviation of each model parameter defines the quality of the fit for that parameter; parameters whose measured uncertainty overlaps zero at the 1σ level are likely to be insignificant and may ultimately be excluded from the final model. For studies (the majority in the dataset) where electron probe uncertainties are not reported, we use the following approximation of typical electron probe uncertainties on the concentration of an element as a function of that concentration:

$$\sigma_{\text{estimated}}(X) = \begin{cases} 0.0023 * X^{-0.651}, X \neq 0 \\ \sigma_{\text{estimated}}(0) = 0 \end{cases}, \tag{3.24}$$

where X is the mole fraction of the component (element/ion) in oxide form and $\sigma_{\text{estimated}}$ is the estimated uncertainty on that component. Elements that were not reported as present in specific amphiboles analyses are fixed at $X = \sigma_{\text{estimated}} = 0$. These estimated uncertainties are not necessarily Gaussian since: 1) mole fractions of elements and vacancies cannot be negative and yet the $1\sigma_{\text{estimated}}$ band begins to cross zero near the analytical detection limit, and 2) the composition must be consistent with the amphibole formula (e.g., amphiboles cannot have more than eight tetrahedral Si^{4+} atoms per formula unit). Nonetheless, we used a Gaussian deviate function to vary each mole fraction independently about the measured value with the known or estimated standard deviation. These trial mole fraction vectors are mapped to trial $\vec{R}$ vectors, which are renormalized to sum to unity. The order parameters S_{Fe}, S_{Mn}, and S_{Ca} are adjusted to remain within legal bounds, and S_{Mg} is calculated implicitly. If the resulting composition is illegal, it is scaled back towards the nominal value by reducing all the added errors by an equal fraction until a valid composition is found. Likewise, the volumes in the $\vec{B}$ vector are also varied using a Gaussian deviate function about the measured value with standard deviation either the stated measurement error or 1 Å^3, whichever is greater. We continued generating trial $\mathbb{A}$ matrices and $\vec{B}$ vectors in this manner until we had 1,000 acceptable trials.

3.4 Results

3.4.1 Linear Model

We first obtained the set of cell volumes for each of the 13 compositional end members of the model (R's) and an S_{Fe} term that yield a best fit of the overall dataset to the linear model, where the end-member volumes are simply averaged in proportion to the R_i, plus a correction for Fe ordering (Table 3.3). The reduced χ^2 value of the linear model is 8.44, which indicates a rather poor fit. Results from the Monte Carlo assessment of the linear model indicate that the estimated uncertainties on composition, ordering, and volume data cause the greatest uncertainty in b_1, the coefficient of ordering term for S_{Fe}, with a 1σ error of 41.2% (Table 3.4). By comparison, the coefficients associated with the R terms are better defined, with 1σ errors ranging from 0.03% (for R_5) to 1.11% (for R_4; recall that large values of R_4, i.e., Mn-rich compositions, are absent from the calibration set).

Table 3.3. Linear and Second-Order Model Parameters.

Parameter	Linear Model	Second-Order Model
a_1	908.35	907.51
a_2	883.55	881.57
a_3	919.22	921.90
a_4	934.77	936.01
a_5	901.33	900.32
a_6	915.05	915.55
a_7	880.67	888.24
a_8	910.10	907.38
a_9	921.81	922.65
a_{10}	866.54	863.75
a_{11}	892.89	897.54
a_{12}	907.07	902.06
a_{13}	900.54	900.21
b_1	-3.07	-4.36
$a_{3,11}$		-43.33
$a_{7,10}$		-15.26
$c_{10,3}$		33.33
$a_{7,9}$		-20.04
$a_{1,7}$		-10.81
$a_{2,13}$		18.61
$a_{6,12}$		14.39
$a_{5,12}$		13.26
$a_{6,9}$		-13.88
$a_{7,13}$		-7.57
$a_{1,6}$		-5.13
$a_{7,11}$		-7.97
$c_{9,3}$		-72.42
$a_{2,3}$		0.35
$a_{1,9}$		-0.70
$a_{1,10}$		2.59
$a_{5,13}$		-0.10
$a_{10,13}$		4.08

3.4.2 Nonlinearity

Nonlinear parameters included in the second-order model were chosen by three approaches. We first conducted an exercise that involved sequentially adding whichever second-order parameter yielded the greatest decrease in the reduced χ^2 value. To avoid overfitting, we continued this process only until we had added two parameters that depend on S_{Ca}, because we expect non-linear interactions between the abundance of Ca in the model and the ordering state of that Ca between A and B sites.

Table 3.4. Results from the Monte Carlo Scheme (n=1,000) applied to the linear model.

Parameter	Monte Carlo Average	1σ	Minimum	Maximum	Linear Model
a_1	908.88	0.37	907.56	910.26	908.35
a_2	886.60	3.25	877.96	897.28	883.55
a_3	919.41	1.08	916.28	924.14	919.22
a_4	911.48	10.12	880.03	938.93	934.77
a_5	901.41	0.35	900.35	902.56	901.33
a_6	914.25	1.00	911.05	916.79	915.05
a_7	880.90	0.62	879.18	883.72	880.67
a_8	908.99	1.73	903.89	914.27	910.10
a_9	922.30	0.93	919.56	925.71	921.81
a_{10}	866.80	0.63	864.64	869.05	866.54
a_{11}	893.08	1.37	889.22	897.55	892.89
a_{12}	907.14	1.51	901.94	911.60	907.07
a_{13}	901.38	0.50	899.81	903.09	900.54
b_1	-5.99	2.47	-14.61	0.48	-3.07

This approach motivated the addition of thirteen second-order parameters (Table 3.5): $a_{3,11}$, $a_{7,10}$, $c_{10,3}$, $a_{7,9}$, $a_{1,7}$, $a_{2,13}$, $a_{6,12}$, $a_{5,12}$, $a_{6,9}$, $a_{7,13}$, $a_{1,6}$, $a_{7,11}$, and $c_{9,3}$ (recall that $a_{i,j}$ is the coefficient that expresses dependence on R_iR_j, whereas $c_{i,j}$ is the coefficient that expresses dependence on R_iS_j). At this stage we did not find justification for terms depending on S_{Mg}, which is nearly dependent on S_{Fe} due to the shortage of Mn-rich amphiboles in the data set. The incorporation of more Mn-rich amphiboles may change this decision in the future, as independent effects of Mg and Fe ordering might emerge.

Next, we looked at each binary join by isolating the data where the absolute values of all but two of the R values are ≤ 0.05. Only a few of these binaries are populated by enough data points to judge between linearity and non-linearity; most of the amphiboles in the data set are not close to any binary join. We plotted the residuals from the linear model and found evidence in this exercise for residual non-linearity along the R_2-R_3 and the R_1-R_9 joins (Figure 3.3). Hence $a_{2,3}$ and $a_{1,9}$ were provisionally added to the second-order model.

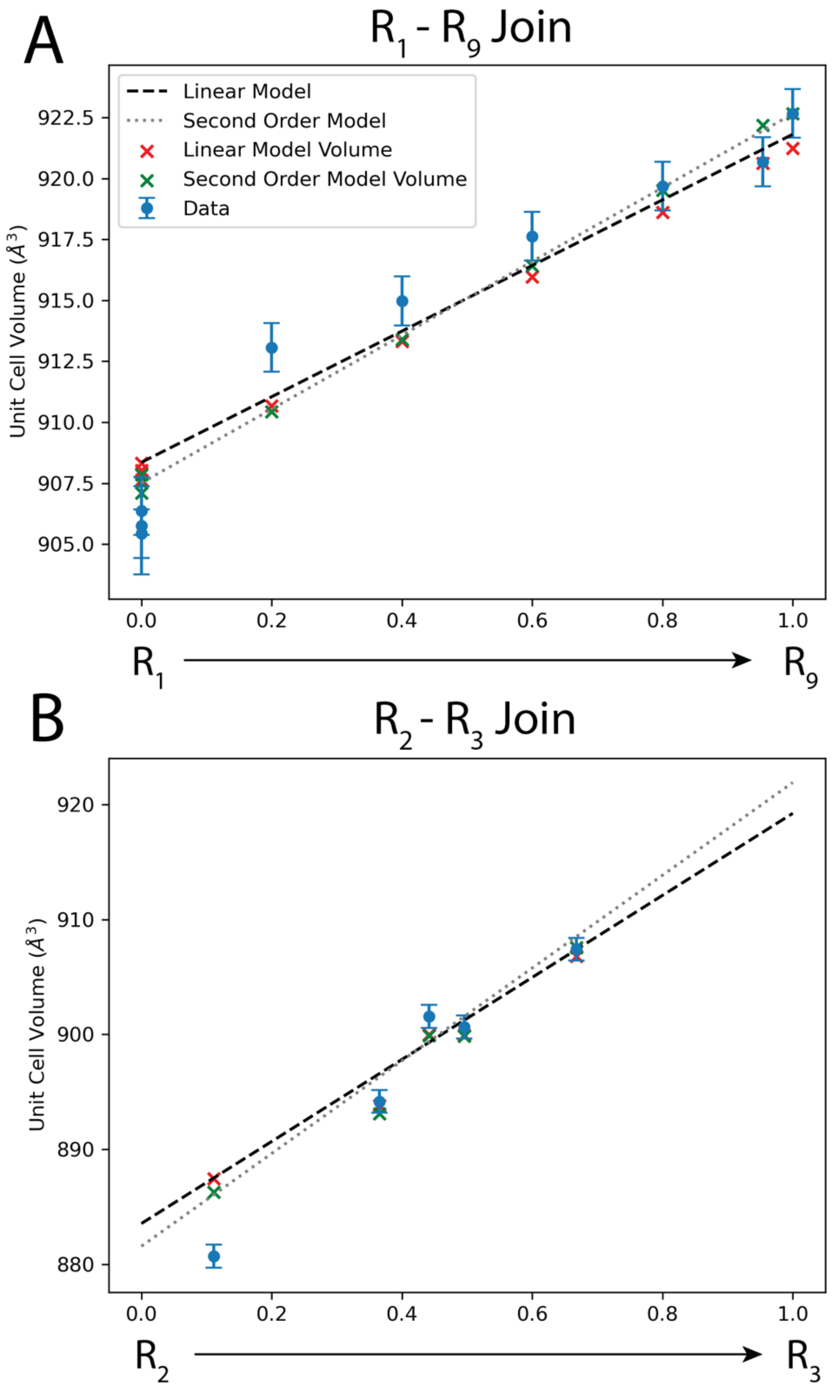

Figure 3.3. Measured data, linear model, linear modeled volumes, second-order model, and second-order modeled volumes for binary joins between R_1 and R_9 (A) and R_2 and R_3 (B). Order parameters are set to zero for the model lines but considered for the modeled data. Uncertainties on the 1 Å^3 or the measured uncertainty on each data point, whichever is larger.

Finally, second-order parameters were added based on visualization of volume residuals of the linear model along pseudo-joins in R_i vs. R_j cross plots (Figure 3.4). We define a pseudo-join as the line between (R_i, R_j) = (1,0) and (0,1) on each of these cross plots. Data that plot on or close to a pseudo-join in these cross plots may not in fact be near the corresponding binary join (since large positive and negative values of different R values are permissible so long as all R_i sum to one, and the limit on $|R_i|$ is not applied here). Nonetheless, if the residuals of points near the middle of the pseudo-join line in R_i vs. R_j space exhibit more negative or positive values than those near the ends of the pseudo-join, we infer that the addition of an $a_{i,j}$ parameter could remediate this non-linearity. Examining all the binary pseudo-join plots, we identified three additional second-order parameters to be provisionally included in the model: $a_{1,10}$, $a_{5,13}$, and $a_{10,13}$ (Figure 3.4).

Collectively, inclusion of these 18 second-order parameters lower the reduced χ^2 value of the model to 5.53. However, the error is dominated by a few outliers. The five highest χ^2 values among the data sum to 560 (contributing ~1 to the reduced χ^2). The results from the Monte Carlo Scheme reveal that the linear parameters remain well-determined in the expanded second-order fit, but the second-order parameter values are not especially robust; several of them range positive to negative at the 1σ level (Table 3.6). This indicates that, despite the improvement in model fit that comes from adding second-order parameters, the data set apparently remains too sparse to rigorously constrain most of these parameters.

Table 3.5. Results from sequentially adding 13 second-order parameters to the model in the order of parameters that achieved the greatest decrease in reduced χ^2.

	Reduced χ^2
Linear Model	8.44
$a_{3,11}$	7.99
$a_{7,10}$	7.62
$c_{10,3}$	7.17
$a_{7,9}$	6.85
$a_{1,7}$	6.64
$a_{2,13}$	6.49
$a_{6,12}$	6.32
$a_{5,12}$	6.12
$a_{6,9}$	5.96
$a_{7,13}$	5.79
$a_{1,6}$	5.67
$a_{7,11}$	5.61
$c_{9,3}$	5.54

3.5 Discussion

3.5.1 Evaluating the Linear Model

The reduced χ^2 value of the linear model is 8.44, which is much greater than one, indicating that the average data point is misfit by a few times its estimated uncertainty. Although χ^2 is an incomplete description of the error of the model, since it neglects composition and ordering errors in the data, the primary result of the linear fitting exercise is motivation to proceed to a second-order model in hopes of capturing non-linear behavior in the data (e.g., Figs. 3.3 and 3.4). On the other hand, the Monte Carlo scheme applied to the linear model does provide confidence that the fitted end-member volumes are stable and well-constrained by the data, with the partial exception of permanganogrünerite (a_4). This could be driven by the low Mn contents of amphiboles in this dataset. The average of the coefficients

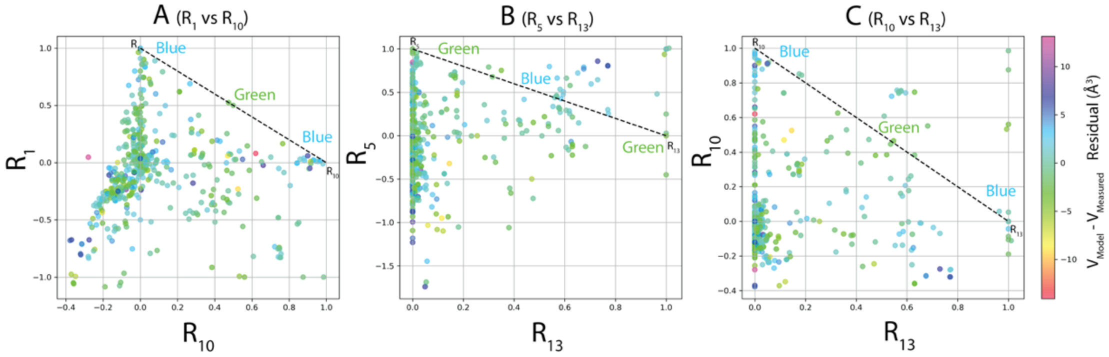

Figure 3.4. *R* parameter cross-plots color-coded by volume residuals from the linear model in Å^3. Black dashed lines represent pseudo-joins between R end members. The three cross-plots shown reveal evidence of non-linearity along the pseudo-join and motivated inclusion of corresponding second-order parameters. Green (positive volume residuals) and Blue (negative volume residuals) labels along the pseudo-joins assist with highlighting second-order behavior of the residuals.

determined by the Monte Carlo assessment are all within 2σ or better of the nominal fit to the linear model, except for a_4 (Tables 3.3 and 3.4), which may result from underrepresentation of R_4 in the data (Figure 3.1).

Table 3.6. Results from the Monte Carlo Scheme (n=1,000) applied to the second-order model.

Parameter	Monte Carlo Average	1σ	Minimum	Maximum	2^{nd}-Order Model
a_1	906.79	0.76	904.33	908.94	907.51
a_2	885.93	3.42	876.20	899.82	881.57
a_3	921.99	0.91	919.34	925.15	921.90
a_4	915.54	9.79	882.57	939.83	936.01
a_5	901.09	0.43	899.85	902.79	900.32
a_6	914.78	0.83	911.47	917.38	915.55
a_7	887.93	1.35	884.43	892.29	888.24
a_8	904.71	1.72	898.71	910.21	907.38
a_9	921.33	0.97	917.70	924.27	922.65
a_{10}	864.83	0.66	862.55	867.11	863.75
a_{11}	896.70	1.42	892.29	900.69	897.54
a_{12}	903.72	2.10	897.20	913.22	902.06
a_{13}	901.97	1.30	898.15	906.48	900.21
b_1	-4.34	2.55	-14.39	2.76	-4.36
$a_{3,11}$	-35.55	7.17	-60.80	-9.36	-43.33
$a_{7,10}$	-12.83	2.03	-19.02	-6.61	-15.26
$c_{10,3}$	48.85	17.61	-3.38	118.70	33.33
$a_{7,9}$	-19.59	5.12	-34.91	-0.53	-20.04
$a_{1,7}$	-12.12	4.03	-33.34	-1.80	-10.81
$a_{2,13}$	13.79	5.82	-3.33	32.73	18.61
$a_{6,12}$	12.39	2.44	4.68	20.42	14.39
$a_{5,12}$	11.98	2.66	4.46	21.43	13.26
$a_{6,9}$	-6.78	4.02	-18.26	4.95	-13.88
$a_{7,13}$	-6.29	4.34	-23.72	5.40	-7.57
$a_{1,6}$	1.66	3.05	-8.12	12.45	-5.13
$a_{7,11}$	-2.40	4.86	-16.27	13.39	-7.97
$c_{9,3}$	21.33	18.48	-68.58	70.68	-72.42
$a_{2,3}$	-12.36	6.06	-29.91	9.23	0.35
$a_{1,9}$	2.13	3.30	-9.20	15.71	-0.70
$a_{1,10}$	5.79	5.17	-12.54	22.75	2.59
$a_{5,13}$	-2.79	2.18	-9.97	3.56	-0.10
$a_{10,13}$	13.36	6.50	-3.60	31.37	4.08

The ordering term in the linear model, a coefficient expressing dependence on S_{Fe}, ranges from negative to nearly zero in the Monte Carlo trials (Table 3.4). However, the values of S_{Fe} and other ordering parameters in the Monte Carlo trial set are not directly generated using estimated or known uncertainty; they are dependent on the generated trial compositions and may not capture the uncertainty in ordering in the real data. Also, most amphiboles in the data predominantly host Ca or Na on the B sites, indicating that that the effect of ordering of Fe^{2+} onto the B site in grunerite-rich compositions is not well represented in the data set. Specifically, in the current data S_{Fe} is mostly negative (that is, Fe^{2+} is mostly on the C sites), yet in cummingtonite-grünerite series amphiboles Fe^{2+} does exhibit a strong preference for the B site relative to Mg (Hirschmann et al., 1994).

3.5.2 Improving the Second-Order Model

The reduced χ^2 value of the second-order model is 5.53, which is still high. Improvement of the reduced χ^2 to ~1 may be achieved by selectively filtering outliers from the data. Removal of the five most outlying points decreases the reduced χ^2 value to 4.7, without refitting. Removal of the 10% of the data points contributing the most to the reduced χ^2 in the fit to all 532 data points brings the reduced χ^2 value of the model to 2.8 ($n = 479$), again without refitting. We have additional reasons to suspect that the outliers present in the data reflect bad data rather than true complexity in the volume of the monoclinic amphiboles. One approach to identifying such bad data is to calculate Euclidean distances between $(\vec{R}, \vec{S})$ coordinates and plot this against difference in measured volume. We presume that the true volume function is a smooth surface, and hence when there are nearby points in $(\vec{R}, \vec{S})$ space with wildly different volumes, one (or both) are suspect. Moreover, for those refinements that are documented in the published literature (many are only available in internal documents at IGG Pavia), detailed evaluation of the refinements and the method of computing composition and ordering in the original reports may facilitate the removal of low-quality data.

The results from the Monte Carlo scheme reveal that second-order parameters are poorly constrained in the current fit. Despite this, some coeffects for the Monte Carlo scheme consistently show negative ($a_{3,11}$, $a_{7,10}$, $a_{7,9}$, $a_{1,7}$) or positive ($a_{6,12}$, $a_{5,12}$) second-order behavior in all 1,000 trials (Table 3.6). While many others exhibit either negative ($c_{10,3}$, $a_{2,13}$, $a_{2,3}$, $a_{5,13}$) or positive ($a_{6,9}$, $a_{7,13}$, $a_{1,10}$, $a_{10,13}$) second-order behavior within 1σ uncertainty, the calibrated $a_{2,3}$ coefficient of the second-order model is slightly positive in contrast to its tendency to be negative at 1σ in the Monte Carlo Scheme. Similarly, $a_{1,9}$ has a tendency toward positive values in the Monte Carlo calibrations, while the $a_{1,9}$ of the model is slightly negative. Note that a model with a positive $a_{1,9}$ coefficient would better satisfy misfits along the R_1-R_9 join (Figure 3.3A). The second-order behavior (positive or negative) of the $a_{1,6}$ and $a_{7,11}$ coeffects are not well constrained by the Monte Carlo scheme at 1σ. Curiously, the $c_{9,3}$ coefficients generated by the Monte Carlo scheme were all greater than that of the second-order model. This could be attributed to the influences of non-zero S_{Ca} values generated from the Monte Carlo scheme. Introduction of excessive Mg, Mn, Ca, or Fe^{2+} on the B sites can force all Na to the A site followed by any excess Ca. This process elevates S_{Ca}, which is otherwise mostly zero (Figure 3.1), introducing a S_{Ca} influence to the calibration of $c_{i,3}$ in the Monte Carlo scheme that was not present during calibration of the second-order model. Adjustments of S_{Ca} from zero to non-zero values associated with the Monte Carlo scheme could shift the $c_{9,3}$ coefficients away from the calibrated model while maintaining consistency with estimated compositional uncertainties. In contrast, the $c_{10,3}$ coefficient (other second-order parameter involving S_{Ca}) of the model is within the bounds of the coefficients produced by the Monte Carlo scheme.

A sign of a more stable, reliable, and error-free database would be well-constrained values of the second-order parameters in an updated fit. Also, although we added five additional second-order parameters to the model based on examination of binary joins and pseudo-joins, the influence of these additional parameters on reduced χ^2 was negligible (5.54 to 5.53), and the improvement in fitting to the selected binaries is not very apparent. In fact, some data points on the selected binaries are better fit by the linear model (Figure 3.3). This likely reflects the influence of data with large values of the *R* parameters defining the binaries and pseudo-joins that nevertheless do not lie directly on the joins or pseudo-joins. Moreover, none of the five second-order terms added on the basis of examination of binary joins and pseudo-joins are resolved from zero in the Monte Carlo simulation. We will drop these terms from the working model.

3.5.3 Compressibility and Thermal Expansion

Parameterization for thermal expansion and compressibility of monoclinic amphiboles will be necessary to model the thermodynamics of this mineral group at magmatic conditions (high pressure and temperature). While thermal expansion has been experimentally constrained on a subset of well-characterized amphiboles (e.g., Tribaudino *et al.*, 2008, 2022), at this time there is not enough data to constrain the thermal expansion of most of the end-members in our model, or the influence of elevated temperature on ordering (and vice versa). As adequate high temperature diffraction data becomes available, it may be possible to calibrate a thermal expansion model. Yet thermal expansion coefficients can vary by as much as ~50% among the amphiboles (Tribaudino *et al.*, 2022), suggesting considerable risk in filling in missing components by extrapolation.

Modeling the compressibility of monoclinic amphiboles as a function of composition will be necessary as well, as compressibility does vary significantly among amphibole compositions (e.g., Comodi *et al.*, 1991, 2010). When high-pressure diffraction data are not available, volume for amphiboles calculated at high pressure via density functional theory simulations may be the best route to calibrating such a model. Offsets in the simulations can be partially corrected using existing high-pressure diffraction data, and then the corrected simulations may be judiciously used to fill out the full composition-compressibility relationship.

3.6 Conclusion

We develop a framework for a volume model of monoclinic amphiboles that is compatible with the form in which mineral solid-solution models are incorporated in the MELTS algorithm. Preliminary linear and second-order models are produced and assessed using x-ray diffraction refinement data for amphiboles with well determined compositions. We find that additional filtering of the data may be needed to better calibrate the model by identifying and removing outliers. Furthermore, we address gaps in the available data which are detrimental to the calibration, such as the low number of Mn-rich amphiboles and the dearth of data at elevated temperature and pressure. The final volume model based on this framework will be part of a monoclinic amphibole solution model to be incorporated into the MELTS software, where the stabilizing influence of minor components is expected to yield petrologically useful predictions of amphibole crystallization in hydrous magmatic systems.

Chapter Three References

Aarons, S. M., Johnson, A. C., & Rader, S. T. (2021). Forming Earth's Continental Crust: A Nontraditional Stable Isotope Perspective. *Elements*, *17*(6), 413–418. https://doi.org/10.2138/gselements.17.6.413

Antao, S. M., Hassan, I., Wang, J., Lee, P. L., & Toby, B. H. (2008). STATE-OF-THE-ART HIGH-RESOLUTION POWDER X-RAY DIFFRACTION (HRPXRD) ILLUSTRATED WITH RIETVELD STRUCTURE REFINEMENT OF QUARTZ, SODALITE, TREMOLITE, AND MEIONITE. *The Canadian Mineralogist*, *46*(6), 1501–1509. https://doi.org/10.3749/canmin.46.5.1501

Asimow, P. D., Dixon, J. E., & Langmuir, C. H. (2004). A hydrous melting and fractionation model for mid-ocean ridge basalts: Application to the Mid-Atlantic Ridge near the Azores: HYDROUS MELTING AND FRACTIONATION. *Geochemistry, Geophysics, Geosystems*, *5*(1), n/a-n/a. https://doi.org/10.1029/2003GC000568

Bardelli, L., Suzaño, N., Arnosio, M., Báez, W., Becchio, R., Viramonte, J., & Lucci, F. (2023). Comparing the biotite and amphibole single-mineral thermobarometric models: A case study from the Cordillera de San Buenaventura volcanic rocks, Puna plateau of Central Andes (Argentina). *Journal of South American Earth Sciences*, *127*, 104406. https://doi.org/10.1016/j.jsames.2023.104406

Collins, W. J., Murphy, J. B., Johnson, T. E., & Huang, H.-Q. (2020). Critical role of water in the formation of continental crust. *Nature Geoscience*, *13*(5), 331–338. https://doi.org/10.1038/s41561-020-0573-6

Comodi, P., Ballaran, T. B., Zanazzi, P. F., Capalbo, C., Zanetti, A., & Nazzareni, S. (2010). The effect of oxo-component on the high-pressure behavior of amphiboles. *American Mineralogist*, *95*(7), 1042–1051. https://doi.org/10.2138/am.2010.3429

Comodi, P., Mellini, M., Ungaretti, L., & Zanazzi, P. F. (1991). Compressibility and high pressure structure refinement of tremolite, pargasite and glaucophane. *European Journal of Mineralogy*, *3*(3), 485–499.

Downs, R. T. and Hall-Wallace, M. (2003). The American Mineralogist crystal structure database. *American Mineralogist*, *88*(1), 247–250.

Ernst, W. G. (1968). Crystal Chemistry of the Amphiboles. In W. G. Ernst, *Amphiboles* (pp. 4–18). Springer Berlin Heidelberg. https://doi.org/10.1007/978-3-642-46138-5_2

Evans, B. W., & Yang, H. (1998). Fe-Mg order-disorder in tremolite-actinolite-ferro-actinolite at ambient and high temperature. *American Mineralogist*, *83*(5–6), 458–475. https://doi.org/10.2138/am-1998-5-606

Ghiorso, M., Evans, B., Hirschmann, M., & Yang, H. (1995). Thermodynamics of the amphiboles: Fe-Mg cummingtonite solid solutions. *American Mineralogist*, *80*(1), 502–519.

Ghiorso, M. S., Hirschmann, M. M., Reiners, P. W., & Kress, V. C. (2002). The pMELTS: A revision of MELTS for improved calculation of phase relations and major element partitioning related to partial melting of the mantle to 3 GPa: pMELTS, A REVISION OF MELTS. *Geochemistry, Geophysics, Geosystems*, *3*(5), 1–35. https://doi.org/10.1029/2001GC000217

Ghiorso, M. S., & Sack, R. O. (1995). Chemical mass transfer in magmatic processes IV. A revised and internally consistent thermodynamic model for the interpolation and extrapolation of liquid-solid equilibria in magmatic systems at elevated temperatures and pressures. *Contributions to Mineralogy and Petrology*, *119*(2–3), 197–212. https://doi.org/10.1007/BF00307281

Gualda, G. A. R., Ghiorso, M. S., Lemons, R. V., & Carley, T. L. (2012). Rhyolite-MELTS: A Modified Calibration of MELTS Optimized for Silica-rich, Fluid-bearing Magmatic Systems. *Journal of Petrology*, *53*(5), 875–890. https://doi.org/10.1093/petrology/egr080

Hawthorne, F. C., Day, M. C., Fayek, M., Linthout, K., Lustenhouwer, Wim. J., & Oberti, R. (2022). Ferro-papikeite, ideally NaFe22+(Fe32+Al2)(Si5Al3)O22(OH)2, a new orthorhombic amphibole from Nordmark (Western Bergslagen), Sweden: Description and crystal structure. *American Mineralogist*, *107*(2), 306–312. https://doi.org/10.2138/am-2021-7877

Hawthorne, F. C., Oberti, R., Harlow, G. E., Maresch, W. V., Martin, R. F., Schumacher, J. C., & Welch, M. D. (2012). Nomenclature of the amphibole supergroup. *American Mineralogist*, *97*(11–12), 2031–2048. https://doi.org/10.2138/am.2012.4276

Hirschmann, M., Evans, B. W., & Yang, H. (1994). Composition and temperature dependence of Fe-Mg ordering in cummingtonite-grunerite as determined by X-ray diffraction. *American Mineralogist*, *79*(9–10), 862–877.

Holtstam, D., Cámara, F., Karlsson, A., Skogby, H., & Zack, T. (2022). Ferri-taramite, a new member of the amphibole supergroup, from the Jakobsberg Mn–Fe deposit, Värmland, Sweden. *European Journal of Mineralogy*, *34*(5), 451–462. https://doi.org/10.5194/ejm-34-451-2022

Mutch, E. J. F., Blundy, J. D., Tattitch, B. C., Cooper, F. J., & Brooker, R. A. (2016). An experimental study of amphibole stability in low-pressure granitic magmas and a revised Al-in-hornblende geobarometer. *Contributions to Mineralogy and Petrology*, *171*(10), 85. https://doi.org/10.1007/s00410-016-1298-9

Oberti, R., and Boiocchi, M., (2023). (Personal communication).

Oberti, R., Ungaretti, L., Cannillo, E., & Hawthorne, F. C. (1992). The behaviour of Ti in amphiboles; I, Four- and six-coordinate Ti in richterite. *European Journal of Mineralogy*, *4*(3), 425–439.

Putirka, K. (2016). Amphibole thermometers and barometers for igneous systems and some implications for eruption mechanisms of felsic magmas at arc volcanoes. *American Mineralogist*, *101*(4), 841–858. https://doi.org/10.2138/am-2016-5506

Reece, J. J., Redfern, S. A. T., Welch, M. D., Henderson, C. M. B., & McCammon, C. A. (2002). Temperature-dependent Fe 2+ -Mn 2+ order-disorder behaviour in amphiboles. *Physics and Chemistry of Minerals*, *29*(8), 562–570. https://doi.org/10.1007/s00269-002-0267-1

Swindle, C. R. (2023). *Framework for a Volume Model for Monoclinic Amphibole (Code and Data)*. https://doi.org/10.5281/ZENODO.8329902

Tribaudino, M., Bruno, M., Iezzi, G., Della Ventura, G., & Margiolaki, I. (2008). The thermal behavior of richterite. *American Mineralogist*, *93*(10), 1659–1665. https://doi.org/10.2138/am.2008.2895

Tribaudino, M., Hovis, G. L., Almer, C., & Leaman, A. (2022). Thermal expansion of minerals in the amphibole supergroup. *American Mineralogist*, *107*(7), 1302–1312. https://doi.org/10.2138/am-2022-7988

Wieser, P. E., Kent, A. J. R., Till, C. B., Donovan, J., Neave, D. A., Blatter, D. L., & Krawczynski, M. J. (2023). Barometers Behaving Badly I: Assessing the Influence of Analytical and Experimental Uncertainty on Clinopyroxene Thermobarometry Calculations at Crustal Conditions. *Journal of Petrology*, *64*(2), egac126. https://doi.org/10.1093/petrology/egac126

Yong, T., Dera, P., and Zhang, D. (2019). Single-crystal X-ray diffraction of grunerite up to 25.6 GPa: A new high-pressure clinoamphibole polymorph. *Physics and Chemistry of Minerals*, *46*(3), 215–227. https://doi.org/10.1007/s00269-018-0999-1